THÈSE de DOCTORAT DE L'UNIVERSITÉ PARIS VI

Spécialité :
CONSTITUANTS ÉLEMENTAIRES–SYSTÈMES COMPLEXES

présentée par
Carlos Muñoz Camacho

pour obtenir le grade de DOCTEUR de l'UNIVERSITÉ PARIS VI

Diffusion Compton profondément virtuelle dans le Hall A au Jefferson Laboratory

Soutenue le 14 décembre 2005 devant le jury composé de :

Lawrence	CARDMAN	Examinateur
Christian	CAVATA	Rapporteur
Jacques	CHAUVEAU	Président de jury
Nicole	d'HOSE	Directrice de thèse
Xiangdong	JI	Rapporteur
Jacques	MARTINO	Examinateur
Franck	SABATIÉ	Examinateur

Acknowledgments

I carried out my thesis in the *Service de Physique Nucléaire* (SPhN) at CEA-Saclay and I thank Nicolas Alamanos for making this work possible. I would also like to express my gratitude to my thesis director, Nicole d'Hose. Her careful reading of this thesis and her good suggestions and sound advice improved the quality of this document.

During the last three years I was part of the CLAS group. I am especially grateful to Michel Garçon, who provided me with an excellent atmosphere to pursue my research.

My endless and biggest gratitude goes to my thesis advisor, Franck Sabatié, to whom I will always remain indebted. He has followed this work closely from the very first day. His enthusiasm, his deep understanding of physics and his numerous ideas have inspired most of this work. I appreciated his strong support and sincere trust over the last few years. Without his optimism, encouragement and guidance, none of this work would have been possible.

If I have seen further, it is by standing on the shoulders of a giant. I was lucky to work next to Pierre Bertin. His profound insight, his vast knowledge of physics and his contagious passion have made every single day of my thesis an exciting and tantalizing new experience.

I worked at Jefferson Lab for a large part of my time. I would like to thank Kees de Jager for his warm welcome in the Hall A Collaboration.

Further gratitude go to the DVCS collaboration. A special thank to my PhD colleagues Alexandre Camsonne and Malek Mazouz, with whom I had great pleasure working. I am also grateful to all other members, and especially Charles Hyde-Wright, Eric Voutier, Bernard Michel and Catherine Ferdi. The DVCS experiment could not have possible without the help of the Hall A Collaboration at Jefferson Lab. I acknowledge particularly the support received from Robert Feuerbach and Bob Michaels.

Thanks also to all the members of the SPhN. I wish to thank Pierre Guichon for answering my questions, the careful reading of my theory chapter and the help with the interpretation of the results. Particular thanks also to David Lhuillier for his assistance with radiative corrections. Thanks to Etienne Burtin for useful discussion and advice.

Michel Guidal helped me in the very last moments of this work. I appreciated his readiness to answer all my questions.

Special thanks also go to all the other members and former members of the CLAS group at Saclay: Jacques Ball, Diane Doré, Ludyvine Morand, Steven Morrow, François-Xavier Girod and Rita de Masi.

I extend my sincere gratitude to Xiangdong Ji and Christian Cavata for the care-

ful reading of the manuscript and for their suggestions and comments. Also, I thank Larry Cardman, Jacques Chauveau and Jacques Martino for accepting being part of the examination committee and the interest they have shown in my work.

Finally, I thank my family and friends, who help me during all these years to make this work possible.

Contents

Introduction

Ordinary matter consists of protons, neutrons and electrons. Electrons are elementary particles, and their interactions are successfully described by Quantum Electrodynamics (QED). Protons and neutrons are the building blocks of nuclei, and are generally called nucleons. They are known to be formed of elementary particles: quarks and gluons. The interactions between quarks and gluons are described by Quantum Chromodynamics.

Quantum Chromodynamics presents unique characteristics. At very short distances ($<$0.2 fm), it is *asymptotically free*. The interactions between quarks and gluons, represented by the effective coupling constant α_s, become very small. A perturbative treatment, like in QED, allows one to make accurate calculations. However, at large distances, of the order of the nucleon size, the forces become extremely large. Quarks and gluons have never been seen free, but only confined at the interior of hadrons. Quantitatively understanding quark and gluon confinement in Quantum Chromodynamics is one of the outstanding problems and compelling questions in physics today.

In order to understand how QCD works, and especially how the transition from short distances to long distances is made, one needs to turn to experiments. By experimentally studying the structure of the nucleon, we can shed some light into how hadrons are formed from their underlying degrees of freedom: quarks and gluons.

The electromagnetic probe, well described by QED, provides an excellent experimental tool to study hadrons. In the past, it has been used to measure nucleon form factors by elastic scattering and parton distributions through deep inelastic scattering. Recently, new theoretical tools have been developed. They generalize parton distributions and contain form factors, but provide a wealth of new information about quarks and gluons within the nucleon. These new distributions are called Generalized Parton Distributions (GPDs). By experimentally measuring these new quantities one can gain a deeper insight into the nucleon structure.

The easiest process which allows access to GPDs is called Virtual Compton Scattering (VCS), and consists of the production of a real photon off the nucleon, when scattered by a virtual photon. Schematically,

$$\gamma^* \; p \; \rightarrow \gamma \; p \, .$$

This reaction in a certain kinematic regime (where it is called Deep VCS, or DVCS) can provide interesting information about GPDs.

DVCS is a very challenging process to measure experimentally. Firstly, its cross section is very small (of the order of nb). Secondly, identifying this specific channel and separating

it from background requires good experimental resolution. However, as soon as DVCS was pointed out by theorists as a clean way to measure GPDs, several experimental collaborations worldwide provided evidence of this process in their data sample. The statistics of these results were very limited because no experiment had been planned to measure this particular channel before. Nonetheless, these results proved the experimental feasibility of this kind of experiments in the currently available accelerator facilities. At the same time, new experiments were planned. With dedicated experimental setups, much more statistics and better identification of the DVCS channel can be achieved.

The first dedicated DVCS experiment ran in the Hall A of Jefferson Lab in 2004, and is the subject of this thesis. The planning, preparation and the data taking and analysis is the work of a large collaboration. This text describes in detail my contribution to this experiment. Important work necessary to the understanding of the discussion, will only be briefly described and reference to detailed explanations will be provided.

The DVCS experiment in Hall A presented several technical challenges. The small DVCS cross sections are compensated by the very high intensity of the Jefferson Lab accelerator. Two new detectors were constructed specifically for this experiment: an electromagnetic calorimeter and a plastic scintillator array. Due to the experimental constraints, these detectors are located at very small angle and very close to the target. An important electromagnetic and hadronic background reduces the resolution of detectors. Specific electronics and data acquisition system were built for this experiment also, in order to improve detector resolutions.

I joined the DVCS collaboration in 2002 and participated to the preparation of the experimental setup, including the construction and tests of the electromagnetic calorimeter and the plastic scintillator detector. The data was taken during the Fall 2004. An analysis of these data and some preliminary results are presented in this document.

The text is organized as follows:

- Chapter 1 very briefly reviews the theoretical and experimental context of the study of nucleon structure. It is not exhaustive, and the reader is usually referred to more detailed articles or to one of the excellent reviews on the subject. Some analytical expressions from [1], used on the data analysis, are included at the end of this chapter for later reference.

- Chapter 2 describes the experimental setup. The standard setup of Hall A at Jefferson Lab will be briefly reviewed and special attention will be payed to the new DVCS setup, the electromagnetic calorimeter and proton scintillator array, as well as the dedicated DVCS electronics.

- Chapter 3 describes the tools used in the data analysis. In particular, it describes in thorough detail the ARS waveform analysis algorithm, a key ingredient in the experiment raw data analysis.

- Chapter 4 describes the calibration of each of the detectors. It also includes all the tests performed before the production data taking, in order to characterize the new detectors.

- Chapter 5 describes the Monte Carlo simulation used for the acceptance calculation. Details on the event generator written are given. The way real radiative corrections are implemented in the simulation is detailed.
- Chapter 6 describes the analysis of the data, the identification of the DVCS channel and the preliminary results obtained. Attention is payed to the experimental uncertainties. A brief discussion of the results follows.

Chapter 1

Deeply Virtual Compton Scattering

The dynamics of quarks and gluons, the elementary particles that form hadrons, are described by quantum chromodynamics (QCD). However, the knowledge of this theory is not sufficient at this moment to derive quantitative observables starting from its first principles. The mechanism that forms hadrons from the underlying quark and gluonic degrees of freedom is not completely understood. One needs to turn to experiments in order to better understand how QCD works.

There are two complementary approaches when studying the structure of hadronic matter [2]. One can access the spatial distribution of charge in a system by elastic scattering of electrons. The form factors measured in this kind of experiments depend on the momentum transfer to the system and their Fourier transform gives us information about the spatial distribution of the internal constituents. A completely different approach is Deep Inelastic Scattering (DIS), where the momentum distribution of the constituents can be measured.

These two approaches are complementary, but have similar limitations. The form factors do not contain any information about the dynamics of the hadron, such as the momentum of the constituents, while the measurements of DIS do not provide any information about their spatial distribution . From the correlations between the spatial and momentum distributions one can gain a deeper insight into the internal structure of the system.

Let me review briefly these experimental techniques as far as the study of the nucleon structure is concerned. Later, a new and more general approach will be presented, which provides novel fundamental pieces of information about the formation of hadrons from the internal degrees of freedom of QCD.

1.1 Elastic scattering: form factors

In order to determine the charge distribution of a system, one can measure the angular distribution of the scattered electrons and compare it to the known cross section for

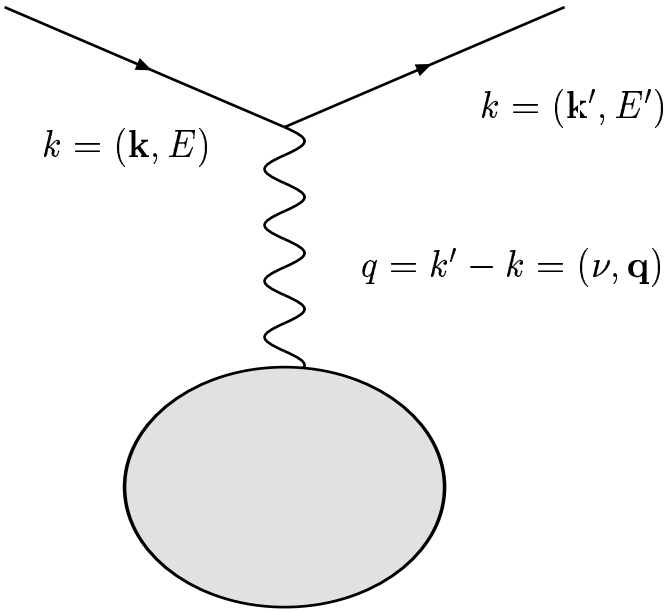

Figure 1.1: Probing internal structure through electron scattering.

scattering electrons from a point charge:

$$\frac{d\sigma}{d\Omega} = \left(\frac{d\sigma}{d\Omega}\right)_{\text{point}} |F(q)|^2, \tag{1.1}$$

where q is the momentum transfer between the incident electron and the target (cf. Fig. 1.1). We can deduce the structure of the target from the form factor $F(q)$ [3]. For unpolarized electrons on a static, spinless target with a charge distribution $\rho(\mathbf{x})$, normalized so that

$$\int \rho(\mathbf{x}) d^3x = 1\,, \tag{1.2}$$

the form factor is found to be the Fourier transform of the charge distribution:

$$F(\mathbf{q}) = \int \rho(\mathbf{x}) e^{i\mathbf{q}\cdot\mathbf{x}} d^3x\,. \tag{1.3}$$

The spectacular measurements of the proton form factors by R. Hofstadter via electron scattering [4] opened a new era in the understanding of hadron structure. In the case of a nucleon, the cross section for elastic electron-proton scattering has been calculated by M. N. Rosenbluth (1950) to leading order in $\alpha \simeq 1/137$ as a function of the scattering angle θ:

$$\frac{d\sigma}{d\Omega}(E) = \sigma_M(E)\left(\frac{E'}{E}\right)\left(\frac{G_{Ep}^2(q^2) + \tau G_{Mp}^2(q^2)}{1+\tau} + 2\tau G_{Mp}^2(q^2)\tan^2\frac{\theta}{2}\right), \tag{1.4}$$

where E and E' are the initial and final electron energies respectively,

$$\sigma_M = \frac{4\alpha^2 E'^2}{q^4} \cos^2 \frac{\theta}{2} \tag{1.5}$$

is the Mott cross section for elastic scattering from a point-like proton, and

$$\tau = \frac{-q^2}{4M^2} \,. \tag{1.6}$$

In the non-relativistic limit the squares of the electric and magnetic form factors $G_{Ep}(q^2)$ and $G_{Mp}(q^2)$ are the Fourier transforms of the spatial distributions of charge and magnetic moment, respectively.

1.2 Inelastic scattering: parton distributions

In inelastic scattering, energy is imparted to the hadronic system. The invariant or missing mass W is the mass of the final hadronic state. It is given by

$$W^2 = (2M\nu + M^2 - Q^2) \,, \tag{1.7}$$

where $\nu = E - E'$. When only the scattered electron is observed (inclusive measurement), the composition of the hadronic state is unknown except for its invariant mass W. On the assumption of one photon exchange, the inclusive differential cross section for electron scattering from the nucleon target is related to two structure functions, W_1 and W_2 according to

$$\frac{d^2\sigma}{d\Omega dE'}(E, E', \theta) = \sigma_M \left(W_2(\nu, q^2) + 2W_1(\nu, q^2) \tan^2 \frac{\theta}{2} \right) . \tag{1.8}$$

This expression is the analog of the Rosenbluth cross section (1.4).

In the limit of $Q^2 = -q^2$ and ν approaching infinity, with a ratio $\omega = 2M\nu/Q^2$ held fixed, the two quantities νW_2 and W_1 become functions of ω only. That is,

$$2MW_1(\nu, q^2) = F_1(\omega) \,, \tag{1.9}$$

$$\nu W_2(\nu, q^2) = F_2(\omega) \,. \tag{1.10}$$

It is this property that is referred to as *scaling* in the variable ω in the *Bjorken limit.*

The experimental observation of scaling of the structure functions was the first evidence of point-like, charged structures within the nucleon. R. P. Feynman first introduced the parton model as an explanation of Deep Inelastic Scattering (DIS) data. In his initial formulation (1969), now called parton theory, he assumed that the proton was composed of point-like partons, from which the electrons scattered incoherently. In an infinite momentum frame of reference, in which the relativistic time dilation slowed down the motion of the constituents, the partons are assumed not to interact with one another while the

virtual photon is exchanged (*impulse approximation*). In this theory, electrons scatter from constituents that are "free", and therefore the scattering reflects the properties and motions of the constituents. This assumption of near-vanishing of the parton-parton interaction during lepton scattering, in the Bjorken limit, was later shown to be a consequence of QCD known as *asymptotic freedom*.

1.2.1 Optical theorem: forward Compton amplitude

Right before the incoming lepton hits the target, it fluctuates into a lepton and a virtual photon, $e(k) \to e(k')\gamma^*(q)$; the latter interacts with the target $|p\rangle$ fragmenting into a number of hadrons in the final state $|n\rangle$ with the total momentum $P_n = \sum_k p_k$. In the single-photon exchange approximation, the amplitude of this process is described by the current-to-current coupling [5],

$$\mathcal{A}_n = L_\mu(k,k')\langle n|j^\mu(0)|p\rangle\,, \tag{1.11}$$

of the hadronic transition amplitude $\langle n|j^\mu|p\rangle$ via the local quark electromagnetic current

$$j^\mu(x) = \sum_q e_q \bar\psi_q(x)\gamma^\mu\psi_q(x)\,, \tag{1.12}$$

and the leptonic current

$$L^\mu(k,k') = \frac{i}{q^2}\bar u(k')\gamma^\mu u(k)\,. \tag{1.13}$$

The measurement is inclusive with respect to the final states and only the scattered lepton is detected. Neglecting the phase-space factor, the cross section reads:

$$\sigma_{\rm DIS} = \frac{\alpha}{4\pi}\sum_n |\mathcal{A}_n|^2(2\pi)^4\delta(p+q-P_n) = \frac{\alpha^2}{q^4}L^\dagger_\mu L_\nu W^{\mu\nu}\,, \tag{1.14}$$

where, using the completeness condition $\sum_n |n\rangle\langle n| = 1$ in summation over the final states, we introduce

$$W^{\mu\nu} = \frac{1}{4\pi}\int d^4z\, e^{iq\cdot z}\langle p|j^\mu(z)j^\nu(0)|p\rangle\,. \tag{1.15}$$

The hadronic tensor $W^{\mu\nu}$ is related via the optical theorem to the imaginary part of the *forward Compton scattering* amplitude:

$$W^{\mu\nu} = \frac{1}{2\pi}\Im{\rm m}T^{\mu\nu}\,, \tag{1.16}$$

where

$$T^{\mu\nu} = i\int d^4z\, e^{iq\cdot z}\langle p|T\{j^\mu(z)j^\nu(0)\}|p\rangle\,, \tag{1.17}$$

is determined by the chronological product of quark electromagnetic currents (1.12).

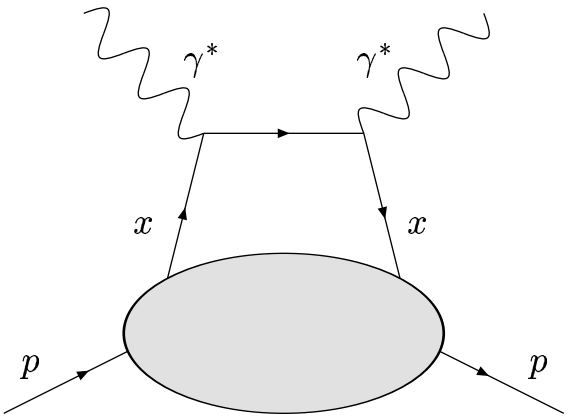

Figure 1.2: Handbag diagram for forward Compton scattering. The imaginary part of its amplitude is related to the DIS amplitude through the optical theorem (1.16).

1.2.2 The Bjorken limit: handbag and light-cone dominance

As mentioned before, the Bjorken limit is defined by large virtualities $Q^2 \to \infty$ and energies $\nu \to \infty$, at fixed Bjorken variable $x_B = Q^2/(2p \cdot q)$.

If the virtuality of the photon is sufficiently high, it will usually "see" only one parton per collision. The transverse distance probed by the virtual photon in the hadron is of order $\delta z_\perp \sim 1/Q$. The probability for coherent scattering on a $n-$parton configuration is suppressed by n-th power of the photon virtuality [5]:

$$\mathcal{P}_n \sim \left(\frac{|\delta \mathbf{z}_\perp|^2}{\pi R_N^2}\right)^n \sim \frac{1}{(Q^2 \pi R_N^2)^n}\,, \tag{1.18}$$

where πR_N^2 is the transverse area of the nucleon. The power-suppressed corrections go under the name of higher twists. Thus, in *leading twist* approximation at high Q^2 one can restrict all considerations to the photon scattering on a single parton. This is known as the *handbag approximation*. In the forward Compton scattering, a quark taken from the hadron absorbs the virtual photon and, as a result, accelerates. Then it re-emits a photon and falls in the *same momentum state*. After the energy is freed into the final state the parton merges back into the parent hadron (cf. Fig. 1.2).

The points of absorption and emission are separated by a light-like distance. To derive the relevant distances in DIS, let us switch to a reference frame where the target proton is at rest and the virtual photon's three-momentum points in the direction opposite to the $z-$axis. Then the virtual photon 4-vector reads:

$$q^\mu = \left(\frac{Q^2}{2Mx_B}, 0, 0, -\frac{Q^2}{2Mx_B}\sqrt{1 + 4M^2x_B^2/Q^2}\right). \tag{1.19}$$

We can express q in light-cone coordinates as:

$$q^\mu = q^+ \tilde{p}^\mu + q^- n^\mu + \vec{q}_\perp^{\,\mu}\,, \tag{1.20}$$

where $q^+ = q^0 + q^3$, $q^- = q^0 - q^3$ and $\tilde{p}$ and n are the Sudakov vectors defined by

$$\tilde{p} = \frac{1}{\sqrt{2}} \begin{pmatrix} 1 \\ 0 \\ 0 \\ 1 \end{pmatrix} , \qquad n = \frac{1}{\sqrt{2}} \begin{pmatrix} 1 \\ 0 \\ 0 \\ -1 \end{pmatrix} . \tag{1.21}$$

When Q^2 is large, the light-cone components of the momentum transfer can be approximated by

$$q^- \sim Q^2/(Mx_B) , \qquad q^+ \sim Mx_B . \tag{1.22}$$

The integrand in equation (1.17) is an oscillatory function and thus gives vanishing result unless the distances involved are

$$z^- \sim 1/(Mx_B) , \qquad z^+ \sim Mx_B/Q^2 . \tag{1.23}$$

Causality ensures $z^2 > 0$ [6], and so $z_\perp < 2z^+z^- \sim 1/Q^2$. Therefore, the only region which contributes to the integral is close to the light-cone $z^2 \approx 0$.

1.2.3 Factorization

The parton model is a beautiful example of an important aspect of the QCD treatment of hard scattering processes. In the parton model, we imagine hadrons as extended objects, made up of constituents held together by their mutual interactions. We assume that the hadrons can be described in terms of virtual partonic states, but that we are not able to calculate the structure of these states. On the other hand, we suppose that we do know how to compute the scattering of a free parton by, say, an electron. This dichotomy of ignorance and knowledge corresponds to our inability to compute perturbatively at long distances in QCD, while having asymptotic freedom at short distances [7]. In the center-of-mass frame, the hadron is Lorentz contracted in the direction of the collision and its internal interactions are time dilated. Since partons do not interact during the collision, they can be thought as carrying a definite fraction x of the hadron's momentum in the center-of-mass frame. We can define a function $q_i(x)$ that expresses the probability that the proton contains a parton of type i and momentum fraction x. The scattering process is essentially incoherent and the cross section may thus be computed by combining probabilities, rather than amplitudes:

$$\sigma_{\rm DIS}(x, Q^2) = \sum_i q_i(x) \sigma_{eq \to eq}(x, Q^2) . \tag{1.24}$$

This important result, which can formally be proven in QCD in the Bjorken limit, is known as *factorization* (for a review of factorization of hard processes in QCD, see [7]). Since the hard quark-photon subprocess implies small distances (large Q^2) and small times (large energies ν), but the scales involved in the formation of the nucleon are much larger, they are uncorrelated and will not interfere.

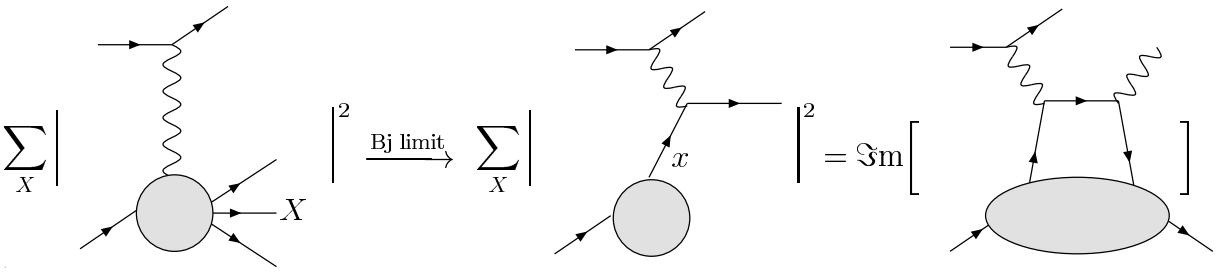

Figure 1.3: Deep inelastic scattering is at *leading twist* dominated by the scattering on a single quark, and so its amplitude is related through the optical theorem to the handbag diagram of the forward Compton scattering.

The non-perturbative phenomena is entirely contained in the functions $q_i(x)$. They describe the internal structure of the hadron and are universal. The same parton distribution of DIS appear in Drell-Yan processes ($A + B \to \mu^+ + \mu^- + X$). The remaining function has two important properties. Firstly, it depends only on the parton type, and not directly on the choice of a hadron. Secondly, it can be computed as a power series in the strong coupling constant $\alpha_s(Q)$, with finite coefficients.

Explicitly writing the value of $\sigma_{eq\to eq}$ in equation (1.24), the DIS cross section reads:

$$\frac{d^2\sigma}{dxdQ^2} = \sum_i e_i^2 q_i(x) \frac{2\pi\alpha^2}{Q^4}\left[1 + \left(1 - \frac{Q^2}{xs}\right)^2\right], \tag{1.25}$$

where $s = (P + k)^2$. Remarkably, the fraction x only depends on the scattered electron momentum. Since the scattered parton has a small mass compared to s and Q^2,

$$0 \simeq (p + q)^2 = 2p \cdot q + q^2 = 2xP \cdot q - Q^2 \,. \tag{1.26}$$

Thus, the momentum fraction x is simply the kinematical variable x_B previously defined:

$$x = \frac{Q^2}{2P \cdot q} = x_B \,, \tag{1.27}$$

which is the inverse of the variable ω appearing in (1.10). Therefore, by measuring the structure functions $F_1(\omega)$ and $F_2(\omega)$ in DIS, one can have access to the *parton distributions* $q_i(x)$, the momentum distributions of quarks within the nucleon.

1.3 Off-forward Compton scattering

Deeply inelastic scattering experiments and other inclusive reactions have been used for over the last three decades as one of the major sources of information on the complicated long distance dynamics of hadrons constituents. However, information obtained in this way is insufficient to constrain the detailed picture of the hadron wave function. There is a large class of hadronic reactions where one gets a more direct access to the wave

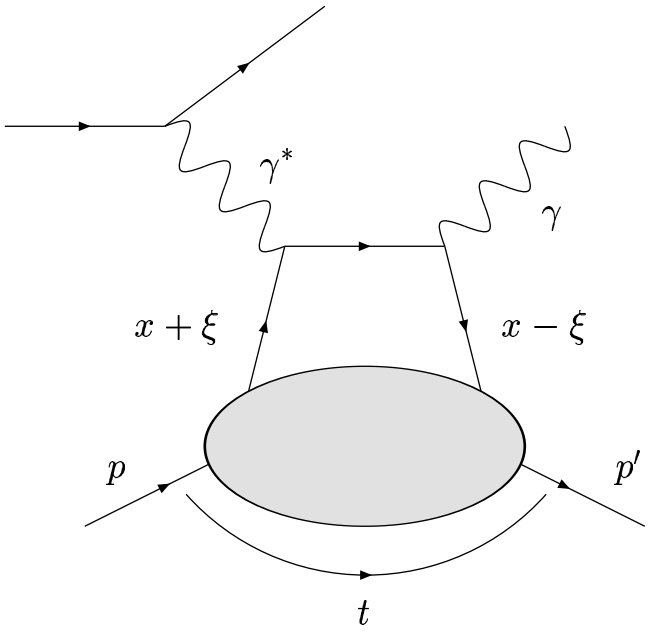

Figure 1.4: Handbag diagram for Deeply Virtual Compton Scattering (DVCS).

functions. Exclusive processes are defined as scattering reactions where the kinematical parameters of all initial and final state particle are specified. From the experimental point of view, this implies a clean identification of the final state of the reaction.

A generalization of the handbag diagram for DIS is shown in Fig. 1.4. Here the virtual photon interacts with a quark of momentum fraction $x+\xi$, but the quark comes back to the nucleon with a *different* momentum fraction, $x-\xi$. This is possible thanks to an overall momentum transfer to the nucleon $\Delta = (p'-p)$, and the emission of a real photon.

The amplitude represented by the diagram of Fig. 1.4 is also a generalization of equation (1.17) for the forward Compton scattering. Now the final proton is in a different state $|p'\rangle$:

$$T^{\mu\nu} = i \int d^4z \, e^{iq\cdot z} \langle p'|T\{j^\mu(z) j^\nu(0)\}|p\rangle \,, \tag{1.28}$$

Lepto-production of real photons off the nucleon,

$$e\ p \to e'\ p'\ \gamma \,, \tag{1.29}$$

or rather, the underlying process of Virtual Compton Scattering (VCS),

$$\gamma^*\ p \to p'\ \gamma \,, \tag{1.30}$$

is dominated, in the Bjorken limit, by the leading twist handbag diagram of Fig. 1.4. A factorization theorem has been proven for VCS in the Bjorken limit or Deeply Virtual

Compton Scattering (DVCS) [8, 9], which allows one to calculate the DVCS amplitude as the product of some *Generalized Parton Distributions* and a handbag coefficient function that is calculable perturbatively.

Following the discussion in [10], we can write the Compton amplitude corresponding to the handbag diagram as

$$T^{\mu\nu} = i \int \frac{d^4k}{(2\pi)^4} \mathrm{Tr}\left\{ \left[\gamma^\nu \frac{i}{\not K - \not\Delta/2 + \not q + i\epsilon} \gamma^\mu + \gamma^\mu \frac{i}{\not K + \not\Delta/2 - \not q + i\epsilon} \gamma^\nu \right]_{\alpha\beta} M_{\alpha\beta}(k) \right\}, \tag{1.31}$$

where μ and ν are the polarization indices of the virtual and real photon and $M_{\alpha\beta}(k)$ is a quark density matrix,

$$M_{\alpha\beta}(k) = \int e^{ikz} d^4z \, \langle p'|\bar\psi_\alpha(-z/2)\psi_\beta(z/2)|p\rangle \, . \tag{1.32}$$

In the Bjorken limit, we can neglect components of four vectors other than the one parallel to n. Introducing the factor $\int dx \frac{d\lambda}{2\pi} e^{i\lambda(x-k\cdot n)} = 1$ and integrating over k and z, the Compton amplitude takes the form [10]:

$$\begin{aligned} T^{\mu\nu}(p,q,\Delta) \;=\; & \frac{1}{2}(g^{\mu\nu} - p^\mu n^\nu - p^\nu n^\mu) \int_{-1}^{1} dx \left(\frac{1}{x - \xi/2 + i\epsilon} + \frac{1}{x + \xi/2 - i\epsilon} \right) \\ & \left[H(x,\xi,\Delta^2) \bar u(p') \not n u(p) + E(x,\xi,\Delta^2) \bar u(p') \frac{i\sigma^{\alpha\beta} n_\alpha \Delta_\beta}{2M} u(p) \right] \\ & + \frac{i}{2} \epsilon^{\mu\nu\alpha\beta} p_\alpha n_\beta \int_{-1}^{1} dx \left(\frac{1}{x - \xi/2 + i\epsilon} - \frac{1}{x + \xi/2 - i\epsilon} \right) \\ & \left[\tilde H(x,\xi,\Delta^2) \bar u(p') \not n \gamma_5 u(p) + \tilde E(x,\xi,\Delta^2) \frac{\Delta\cdot n}{2M} \bar u(p') \gamma_5 u(p) \right], \end{aligned} \tag{1.33}$$

where

$$\xi = \frac{-p\cdot q + \sqrt{(p\cdot q)^2 + Q^2(M^2 - t/4)}}{M^2 - t/4} \xrightarrow{\text{Bjorken limit}} \frac{x_B}{2 - x_B} \tag{1.34}$$

and $t = \Delta^2$. H, $\tilde H$, E and $\tilde E$ are off-forward parton distributions defined through the following light-cone correlation functions,

$$\begin{aligned} \int \frac{d\lambda}{2\pi} e^{i\lambda x} \langle p'|\bar\psi(-\lambda n/2)\gamma^\mu \psi(\lambda n/2)|p\rangle \;&=\; H(x,\xi,t)\bar u(p')\gamma^\mu u(p) \\ &+\; E(x,\xi,t)\bar u(p')\frac{i\sigma^{\mu\nu}\Delta_\nu}{2M} u(p) + \dots \, , \\ \int \frac{d\lambda}{2\pi} e^{i\lambda x} \langle p'|\bar\psi(-\lambda n/2)\gamma^\mu \gamma_5 \psi(\lambda n/2)|p\rangle \;&=\; \tilde H(x,\xi,t)\bar u(p')\gamma^\mu\gamma_5 u(p) \\ &+\; \tilde E(x,\xi,t)\bar u(p')\frac{\gamma_5 \Delta^\mu}{2M} u(p) + \dots \, , \end{aligned} \tag{1.35}$$

where the ellipses denote higher-twist distributions.

1.4 Generalized Parton Distributions

The off-forward parton distributions H, $\tilde{H}$, E and $\tilde{E}$ defined in the preceding section are defined for each flavor of quark i. They are usually called Generalized Parton Distributions (GPDs). Indeed, in the limit of $t \to 0$, we have

$$H^i(x,0,0) = q_i(x)\,, \tag{1.36}$$
$$\tilde{H}^i(x,0,0) = \Delta q_i(x)\,, \tag{1.37}$$

where $q_i(x)$ and $\Delta q_i(x)$ are quark and quark helicity distributions. On the other hand, forming the first moment of these distributions, one gets the following sum rules,

$$\int_{-1}^{1} dx\, H^i(x,\xi,t) = F_1^i(t) \qquad \forall\xi\,, \tag{1.38}$$
$$\int_{-1}^{1} dx\, E^i(x,\xi,t) = F_2^i(t) \qquad \forall\xi\,, \tag{1.39}$$
$$\int_{-1}^{1} dx\, \tilde{H}^i(x,\xi,t) = G_A^i(t) \qquad \forall\xi\,, \tag{1.40}$$
$$\int_{-1}^{1} dx\, \tilde{E}^i(x,\xi,t) = G_p^i(t) \qquad \forall\xi\,, \tag{1.41}$$

where $F_1(t)$ and $F_2(t)$ are the Dirac and Pauli form factors (linear combinations of Rosenbluth form factors G_{Ep} and G_{Mp}) and $G_A(t)$ and $G_P(t)$ are the axial-vector and pseudoscalar form factors, all of them defined for each flavor of quark i. Finally, the second moment of the GPDs is related to the total angular momentum of the quarks J^i in the nucleon, through the so-called Ji sum rule [10, 11]:

$$\int_{-1}^{1} dx\, x[H^i(x,\xi,0) + E^i(x,\xi,0)] = J^i \qquad \forall\xi\,. \tag{1.42}$$

Note that unlike equations (1.36) and (1.37), the $x-$dependence of E and $\tilde{E}$ is unconstrained. For $\xi = 0$, since $H(x,0,0)$ is already measured, Ji's sum rule directly relates the total angular distributions of quarks to the integral of GPD E over x.

1.4.1 Gluon GPDs

Up to this point, only the handbag diagram where the virtual photon interacts with a quark of the nucleon has been considered. At leading twist, there is also the possibility of scattering on a gluon, as in the diagram of Fig. 1.5. This diagram gives rise to gluon GPDs, different from the ones appearing in the diagram of Fig. 1.4. Scattering on a gluon is suppressed with respect to the quark diagram by an order of α_s. However, in the kinematic regime where x_B is small, it can have a significant contribution. In the Bjorken limit, according to Eq. (1.34),

$$\xi \simeq \frac{x_B}{2 - x_B}\,. \tag{1.43}$$

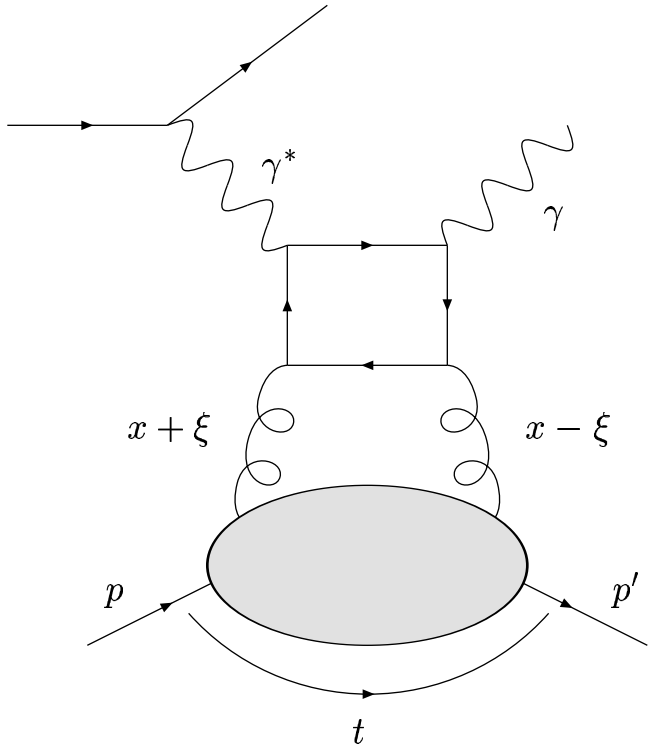

Figure 1.5: Gluon handbag diagram for Deeply Virtual Compton Scattering (DVCS).

When x_B is very small, the momentum fractions $x-\xi$ and $x+\xi$ are very small in some part of the integration region over x, and the contribution can be large enough to compensate the α_s suppression. The DVCS experiment described in this thesis, where $x_B \sim 0.36$, is not sensible to gluon GPDs and they will not be further described. More details can be found in the review papers [5, 12].

1.4.2 Physics in the transverse plane

While GPDs relate to already known quantities as form factors and parton distributions, they contain a wealth of new information. The new feature of GPDs is given by their t–dependence, which introduces a new momentum scale. The target is resolved by the virtual photon on a spatial scale small compared to the target size: a photon of high virtuality Q^2 selects a short-distance region of the target $\Delta b_\perp \sim \hbar/Q$. Meanwhile the net momentum transfer t is independent, and Fourier-conjugate to the spatial location where the virtual photon scattering event occurs. This interpretation of the variable t, pioneered by Burkardt [13, 14] and generalized by Diehl [15], is illustrated in Fig. 1.6.

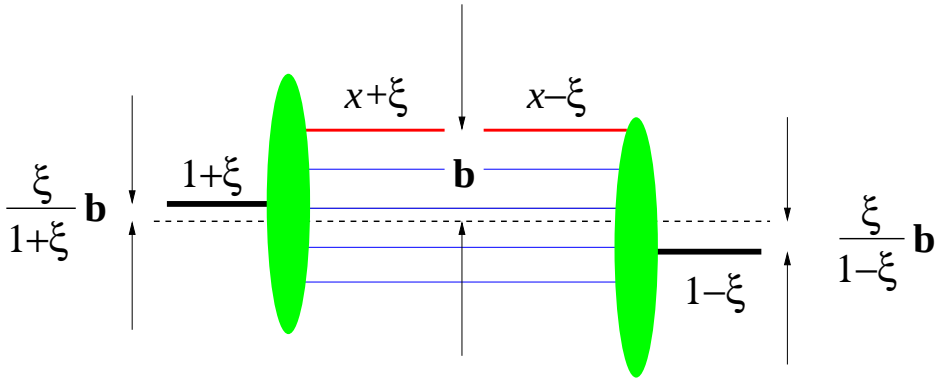

Figure 1.6: DVCS in the transverse plane can be viewed as the emission and reabsorption of a quark at transverse position **b**. The transverse location of the initial and final state proton are shifted relative to each other by an amount of the order of $\xi\mathbf{b}$. Figure taken from [15].

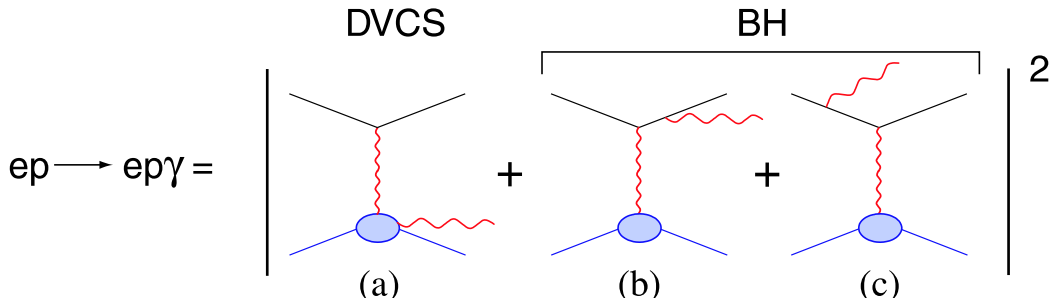

Figure 1.7: Two contributions to the $ep \to ep\gamma$ reaction: the Bethe-Heitler (BH), where the photon of the final state is radiated by the initial or the final electron, and DVCS, where the photon is emitted by the nucleon.

1.4.3 DVCS and BH: nucleon holography

DVCS interferes with the Bethe-Heitler (BH) process, where the real photon of the final state is not emitted by the nucleon but radiated by the electron (Fig. 1.7). This interference allows the simultaneous determination of the real and imaginary parts of the DVCS amplitude (rather than simply the squared amplitude). This technique, an analog to holography, allows a three-dimensional experimental exploration of the nucleon degrees of freedom [16, 17].

If the handbag mechanism dominates, we can access GPDs from DVCS measurements. GPDs are convoluted with x in the DVCS amplitude through the quark propagators $1/(x - \xi + i\epsilon)$:

$$\mathcal{T}^{DVCS} \propto \int_{-1}^{1} dx \frac{H(x,\xi,t)}{x - \xi + i\epsilon} \dots , \tag{1.44}$$

where the ellipses denote similar terms for E, $\tilde{H}$ and $\tilde{E}$. In addition to $|\mathcal{T}^{DVCS}|^2$ which

can be accessed in the DVCS cross section measurement, the interference of DVCS with the BH process adds a new experimental dimension. Indeed, one is able to measure the real part, the integral principal value

$$\Re\mathrm{e}\mathcal{T}^{DVCS} \propto P\int_{-1}^{1} dx \frac{H(x,\xi,t)}{x-\xi}\,, \tag{1.45}$$

and the imaginary part

$$\Im\mathrm{m}\mathcal{T}^{DVCS} \propto -i\pi H(\xi,\xi,t)\,, \tag{1.46}$$

independently. Whereas GPDs appear convoluted in $|\mathcal{T}^{DVCS}|^2$ and $\Re\mathrm{e}\mathcal{T}^{DVCS}$, we can access it directly through $\Im\mathrm{m}\mathcal{T}^{DVCS}$, but only along a precise line of its parameter space ($x=\xi$).

- In the region where the DVCS cross section is much larger than the BH one, we can measure directly σ^{DVCS}:

$$\sigma^{DVCS} \propto \left| \int_{-1}^{1} dx \frac{H(x,\xi,t)}{x-\xi+i\epsilon} \ldots \right|^2 . \tag{1.47}$$

  A deconvolution is needed to access GPDs directly. How to tackle this deconvolution problem remains an outstanding task for theory [18].

- In the region where the BH dominates the cross section, one can use the interference term to gain access to the real and imaginary parts of the DVCS amplitude:

  – The most straight-forward extraction of the interference term, which measures the relative phase between DVCS and BH amplitudes, is achieved by making use of the opposite lepton charge conjugation properties of DVCS and BH amplitudes. The former is odd while the latter is even under change of the lepton charge. The unpolarized beam charge asymmetry gives

$$\sigma^{+} - \sigma^{-} \propto \Re\mathrm{e}\mathcal{T}^{DVCS} = P\int_{-1}^{1} dx \frac{H(x,\xi,t)}{x-\xi} \ldots . \tag{1.48}$$

    and measures the real part of the DVCS amplitude, where a deconvolution is also needed to access GPDs.

  – By either beam or target polarization differences, one can cleanly extract the imaginary part of the DVCS amplitude, where GPDs enter in diverse combinations. Luckily, since the ratio of BH to DVCS amplitude scales like

$$\frac{\mathcal{A}_{DVCS}}{\mathcal{A}_{BH}} \sim \frac{1}{y}\sqrt{\frac{t}{Q^2(y-1)}}\,, \tag{1.49}$$

    with $y = p\cdot q_1/p\cdot k$, for large y or small $-t$, it is safe to neglect $|\mathcal{A}_{DVCS}|^2$ as compared to other terms. Thus, in such kinematical settings one has access to the interference in cross section differences with opposite beam helicities:

$$\sigma^{\rightarrow} - \sigma^{\leftarrow} \propto \Im\mathrm{m}\mathcal{T}^{DVCS} = -i\pi H(\xi,\xi,t)\ldots\,, \tag{1.50}$$

which provides a measurement of the imaginary part of the GPDs directly, but only along the line $x = \xi$.

Note that the cross section difference can be directly related to GPDs, but its experimental measurement is more complicated than trying to access the traditional relative asymmetry or single spin asymmetry (SSA) simply defined as:

$$SSA = \frac{\sigma^{\rightarrow} - \sigma^{\leftarrow}}{\sigma^{\rightarrow} + \sigma^{\leftarrow}}. \tag{1.51}$$

Indeed, the normalization, the efficiency and the acceptance factors cancel out in the ratio. It is clearly the simplest observable one can extract from the data, but the $\varphi-$dependence of the denominator does not allow the simple decomposition in φ harmonics, which relates to GPDs.

1.5 DVCS beyond leading twist

As argued before, the scattering of a virtual photon on a single parton is the leading contribution to DVCS at high Q^2. The simultaneous scattering on two partons is suppressed by a power of the hard scale. Since experimentally accessed processes are probed at finite values of the momentum transfer (sometimes only of the order of a few GeV^2), one has to know the magnitude of power-suppressed contributions, which also go under the name of power corrections or higher twist effects, as they may affect the understanding of lowest order results.

A systematic approach to power corrections in Compton scattering is the operator product expansion (OPE) of the product of two electromagnetic currents. Here information about hadron structure is encoded in matrix elements of higher-twist operators.

DVCS cross section has been computed completely in the twist-three approximation by Belitsky, Müller and Kirchner [1]. The 5-fold differential cross section has the form:

$$\frac{d^5\sigma}{dQ^2 dx_B d\varphi_e dt d\varphi} = \frac{\alpha^3 x_B y}{16\pi^2 Q^2 \sqrt{1+4x_B^2 M^2/Q^2}} \left|\frac{\mathcal{T}}{e^3}\right|^2 . \tag{1.52}$$

In Eq. (1.52) we have integrated over φ_p, the azimuthal angle between the outgoing photon-proton scattering plane and the target polarization direction, and we have introduced the differential with respect to the azimuthal angle φ_e of the electron scattering plane.

The scattering amplitude $\mathcal{T}$ is a superposition of the BH and DVCS amplitudes:

$$|\mathcal{T}|^2 = |\mathcal{T}_{\rm BH}|^2 + |\mathcal{T}_{\rm DVCS}|^2 + \mathcal{I} \tag{1.53}$$

$$\mathcal{I} = \mathcal{T}^*_{\rm DVCS}\mathcal{T}_{\rm BH} + \mathcal{T}_{\rm DVCS}\mathcal{T}^*_{\rm BH} \tag{1.54}$$

1.5.1 Azimuthal harmonic structure of the cross section

We can exploit the structure of the cross section as a function of the angle φ, between the leptonic and hadronic plane, in order to extract a set of independent observables.

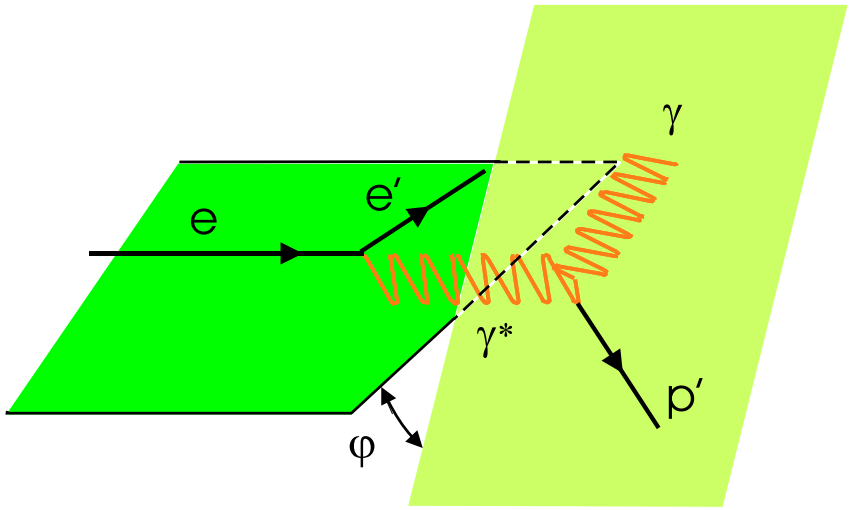

Figure 1.8: Kinematics of the DVCS reaction showing the angle φ between the leptonic and hadronic planes.

Fig. 1.8 illustrates the angle φ between the leptonic and hadronic planes. The individual contributions to the cross section have the form [1]:

$$|\mathcal{T}_{\rm BH}|^2 = \frac{e^6}{x_B^2 y^2 [1+4x_B^2 M^2/Q^2]^2 t \mathcal{P}_1(\varphi)\mathcal{P}_2(\varphi)} \left\{ c_0^{\rm BH} + \sum_{n=1}^{2} c_n^{\rm BH} \cos(n\varphi) + s_1^{\rm BH} \sin\varphi \right\}, \tag{1.55}$$

$$|\mathcal{T}_{\rm DVCS}|^2 = \frac{e^6}{y^2 Q^2} \left\{ c_0^{\rm DVCS} + \sum_{n=1}^{2} \left[c_n^{\rm DVCS} \cos(n\varphi) + s_n^{\rm DVCS} \sin(n\varphi) \right] \right\}, \tag{1.56}$$

$$\mathcal{I} = \frac{\pm e^6}{x_B y^3 t \mathcal{P}_1(\varphi)\mathcal{P}_2(\varphi)} \left\{ c_0^{\mathcal{I}} + \sum_{n=1}^{3} \left[c_n^{\mathcal{I}} \cos(n\varphi) + s_n^{\mathcal{I}} \sin(n\varphi) \right] \right\}, \tag{1.57}$$

where the $+(-)$ in the interference stands for negatively (positively) charged lepton beam. In these formulae, all $\sin(n\varphi)$ terms depend on the electron helicity λ, and for an unpolarized target $s_3^{\mathcal{I}} = 0$ and $s_2^{\rm DVCS} = 0$. The φ dependence of the cross section arises from both the virtual photon polarization (giving rise to the Fourier structure of Eq. (1.55)$-$(1.57)), and from the BH propagators:

$$\begin{aligned} Q^2\mathcal{P}_1 &= (k-q_2)^2 = Q^2 + 2k\cdot\Delta > 0, \\ Q^2\mathcal{P}_2 &= (k-\Delta)^2 = -2k\cdot\Delta + t < 0. \end{aligned} \tag{1.58}$$

The Fourier coefficients of Eq. (1.55)$-$(1.57) are described in detail in [1]. For an unpolarized target, they are the 11 linear combinations of GPDs summarized in Tab. 1.1,

	Unknown	Type	φ dependence
BH^2		Elastic Form Factors^2	$\mathcal{P}_1^{-1}\mathcal{P}_2^{-1}(c_o$ $+c_1\cdot\cos(\varphi)$ $+c_2\cdot\cos 2\varphi)$
$DVCS^2$	$C_{unp}^{DVCS}(\mathcal{F},\mathcal{F}^*)$	twist-2	constant
	$\Re\mathrm{e}[C_{unp}^{DVCS}(\mathcal{F}^{eff},\mathcal{F}^*)]$	twist-3	$\cos\varphi$
	$\Im\mathrm{m}[C_{unp}^{DVCS}(\mathcal{F}^{eff},\mathcal{F}^*)]$	twist-3	$\sin\varphi$
	$\Re\mathrm{e}[C_{unp}^{DVCS}(\mathcal{F}_T,\mathcal{F}^*)]$	twist-3	$\cos 2\varphi$
$BH\cdot$ $DVCS$	$\Re\mathrm{e}[C_{unp}^{I}(\mathcal{F})]$	twist-2	$\mathcal{P}_1^{-1}\mathcal{P}_2^{-1}$ $\mathcal{P}_1^{-1}\mathcal{P}_2^{-1}\cos\varphi$
	$\Re\mathrm{e}[\Delta C_{unp}^{I}(\mathcal{F})]$	twist-2++	$\frac{1}{\mathcal{P}_1\mathcal{P}_2}$
	$\Im\mathrm{m}[C_{unp}^{I}(\mathcal{F})]$	twist-2	$\frac{\lambda}{\mathcal{P}_1\mathcal{P}_2}\sin\varphi$
	$\Re\mathrm{e}[C_{unp}^{I}(\mathcal{F}^{eff})]$	twist-3	$\frac{1}{\mathcal{P}_1\mathcal{P}_2}cos2\varphi$
	$\Im\mathrm{m}[C_{unp}^{I}(\mathcal{F}^{eff})]$	twist-3	$\frac{\lambda}{\mathcal{P}_1\mathcal{P}_2}\sin 2\varphi$
	$\Re\mathrm{e}[C_{T,unp}^{I}(\mathcal{F}_T)]$	twist-2 gluon	$\frac{1}{\mathcal{P}_1\mathcal{P}_2}\cos 3\varphi$

Table 1.1: The 11 independent quantities that can be extracted from the data (see [1] for more details). The indice *unp* refers to an unpolarized target, the only case considered in this text. The forth column gives the formal φ dependence of each term. Each of the unknowns can be binned in $\xi\simeq x_B/(2-x_B)$, t, and Q^2.

preceded of some kinematical factors. We will write here the ones we will use for the data analysis of the experiment, all the others can be found in [1].

1.5.2 Single spin cross section difference

In the kinematic region of the experiment described in this thesis, the BH dominates the cross section. We can access the imaginary part of the DVCS amplitude by a single spin cross section difference. In this case, only the helicity dependent terms remain:

$$d^5\sigma^{\rightarrow}-d^5\sigma^{\leftarrow}=2\cdot\frac{\alpha^3 x_B y}{16\pi^2Q^2e^6\sqrt{1+4x_B^2M^2/Q^2}}\times \left[\frac{e^6}{y^2Q^2}s_1^{\mathrm{DVCS}}\sin\varphi-\frac{e^6}{x_By^3t\mathcal{P}_1(\varphi)\mathcal{P}_2(\varphi)}\left\{s_1^{\mathcal{I}}\sin\varphi+s_2^{\mathcal{I}}\sin 2\varphi\right\}\right], \quad (1.59)$$

where in this equation s_1^{DVCS}, $s_1^{\mathcal{I}}$ and $s_2^{\mathcal{I}}$ no longer contain the helicity dependency, which gives rise to the first factor 2 when writing $d^5\sigma^{\rightarrow}-d^5\sigma^{\leftarrow}$. For small values of $-t$, we can neglect the term s_1^{DVCS} coming from $|\mathcal{T}_{\mathrm{DVCS}}|^2$, following the argumentation of Eq. (1.49). Only the two following harmonics remain:

$$\begin{aligned} s_1^{\mathcal{I}} &= 8Ky(2-y)\Im\mathrm{m}\,\mathcal{C}^{\mathcal{I}}(\mathcal{F}),\\ s_2^{\mathcal{I}} &= \frac{16K^2}{2-x_B}y\Im\mathrm{m}\,\mathcal{C}^{\mathcal{I}}(\mathcal{F}^{\mathrm{eff}}). \end{aligned} \quad (1.60)$$

where K is a $1/Q-$suppressed kinematical factor

$$K^2 = -\frac{t}{Q^2}(1-x_B)\left(1-y-\frac{y^2\epsilon^2}{4}\right)\left(1-\frac{t_{\rm min}}{t}\right)\left\{\sqrt{1+\epsilon^2}+\frac{4x_B(1-x_B)+\epsilon^2}{4(1-x_B)}\frac{t-t_{\rm min}}{Q^2}\right\}, \tag{1.61}$$

which vanishes at the kinematical boundary $t = t_{\rm min}$, determined by the minimal value

$$t_{\rm min} = -Q^2\frac{2(1-x_B)(1-\sqrt{1+\epsilon^2})+\epsilon^2}{4x_B(1-x_B)+\epsilon^2} \qquad \text{with} \qquad \epsilon = 2x_B\frac{M}{Q}. \tag{1.62}$$

There are two *unknowns* in the coefficients of Eq. (1.60):

- The first one, which has a $\sin\varphi$ dependence, is a twist-2 term and is the following linear combination of GPDs:

$$C^{\mathcal{I}}(\mathcal{F}) = F_1\mathcal{H}+\frac{x_B}{2-x_B}(F_1+F_2)\tilde{\mathcal{H}}-\frac{t}{4M^2}F_2\mathcal{E}, \tag{1.63}$$

  where

$$\Im{\rm m}\,\mathcal{H} = \pi\sum_q e_q^2\{H^q(\xi,\xi,t)-H^q(-\xi,\xi,t)\}+\mathcal{O}(\alpha_s), \tag{1.64}$$

$$\Im{\rm m}\,\tilde{\mathcal{H}} = \pi\sum_q e_q^2\{\tilde{H}^q(\xi,\xi,t)+\tilde{H}^q(-\xi,\xi,t)\}+\mathcal{O}(\alpha_s), \tag{1.65}$$

$$\Im{\rm m}\,\mathcal{E} = \pi\sum_q e_q^2\{E^q(\xi,\xi,t)-E^q(-\xi,\xi,t)\}+\mathcal{O}(\alpha_s). \tag{1.66}$$

- The second coefficient, which has a $\sin 2\varphi$ dependence is a twist-3 term, and is the same linear combination, but now of effective twist-3 GPDs:

$$C^{\mathcal{I}}(\mathcal{F}^{\rm eff}) = F_1\mathcal{H}^{\rm eff}+\frac{x_B}{2-x_B}(F_1+F_2)\tilde{\mathcal{H}}^{\rm eff}-\frac{t}{4M^2}F_2\mathcal{E}^{\rm eff}, \tag{1.67}$$

  where $\mathcal{H}^{\rm eff}$, $\tilde{\mathcal{H}}^{\rm eff}$ and $\mathcal{E}^{\rm eff}$ relate to twist-3 GPDs. In the Wandzura-Wilczek (WW) approximation [19], which consists on neglecting the antiquark-gluon-quark correlations, all the twist-3 GPDs can be entirely determined by twist-2 ones.

1.6 GPDs parametrizations

A parametrization of GPDs has been proposed by M. Vanderhaegen, P.A.M. Guichon and M. Guidal (VGG) [20, 21, 22]. Experimental results will be compared with this GPD parametrization in chapter 6. I describe here its main features.

1.6.1 Factorized $t-$dependence

GPDs are parametrized as the product a Double Distribution (DD) [23], which contains the x and ξ dependence, and the Dirac form factor, which parametrizes the $t-$dependence:

$$H^q_{DD}(x,\xi,t) = H^q_{DD}(x,\xi)F^q_1(t)\,, \tag{1.68}$$

where

$$H^q_{DD}(x,\xi) = \int_{-1}^{1} d\beta \int_{-1+|\beta|}^{1-|\beta|} d\alpha \delta(x-\beta-\alpha\xi)F^q(\beta,\alpha)\,. \tag{1.69}$$

The double distribution $F^q(\beta,\alpha)$ can be interpreted as the probability amplitude to find a quark carrying a momentum fraction β of the average nucleon momentum between the initial and final state, and a fraction $(1+\alpha)/2$ of the momentum transfer Δ to the nucleon. The shape of this double distribution is constrained in two ways. First, at $\Delta = 0$ (i.e. $\xi = 0$) the $\beta-$dependence must contain the ordinary parton distributions $q(\beta)$ because H^q must satisfy Eq. (1.36). On the other hand, in the limit of vanishing final nucleon momentum, the double distribution must show a distribution amplitude of mesons of the form $[(1-\beta)-\alpha][(1-\beta)+\alpha]$. The parametrization of the double distribution may be written as

$$F^q(\beta,\alpha) = h(\beta,\alpha)q(\beta)\,, \tag{1.70}$$

where $h(\beta,\alpha)$ is a profile function constrained by Eq. (1.69) when $\Delta \to 0$:

$$q(x) = \int_{-1+|\beta|}^{1-|\beta|} d\alpha h(\beta,\alpha)q(x)\,, \tag{1.71}$$

so that

$$\int_{-1+|\beta|}^{1-|\beta|} d\alpha h(\beta,\alpha) = 1\,. \tag{1.72}$$

Thus, $h(\beta,\alpha)$ can be written as

$$h(\beta,\alpha) = C\frac{[(1-|\beta|)^2-\alpha^2]^b}{(1-|\beta|)^{2b+1}}\,, \tag{1.73}$$

where C is a normalization constant that depends on b. The profile function depends only on one free parameter: b. Larger values of b imply softer $\xi-$dependence of H^q. At the limit $t \to \infty$, $h(\beta,\alpha) = 1$ and H^q becomes $\xi-$independent. Two parameters b are necessary, one for valence quarks (b_{val}) and one for sea quarks (b_{sea}). More details can be found in [24].

1.6.2 Non-factorized $t-$dependence

A more sophisticated $t-$dependence, inspired on the quark-soliton model [21], is given by:

$$H^q(x,\xi=0,t) = \frac{1}{x^{\alpha' t}}q(x)\,, \tag{1.74}$$

where α' is a free parameter that can be interpreted as a Regge trajectory.

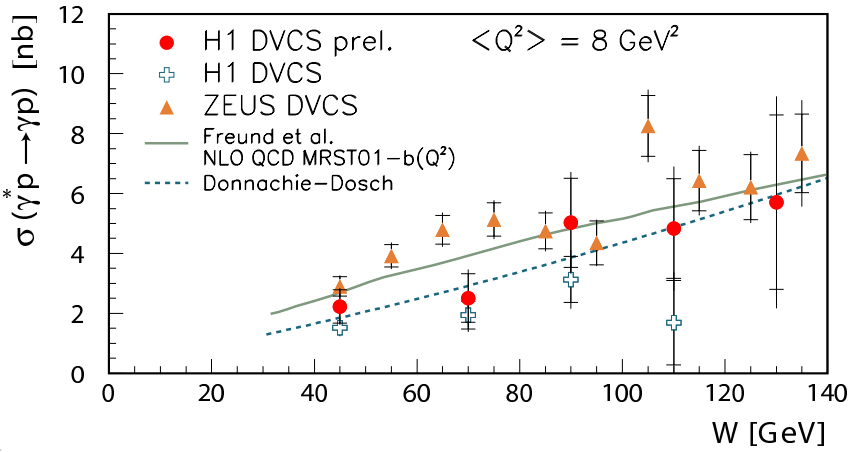

Figure 1.9: Reduced DVCS cross section as a function of W for $\langle Q^2 \rangle = 8\,\mathrm{GeV}^2$. Published H1 [31], preliminary H1 and published ZEUS [32] data are represented. The measurement is in fair agreement with next to leading order QCD predictions using GPD parametrizations [33].

1.6.3 D-term

The $n^{th}-$moment of $H^q_{DD}(x,\xi)$ does not satisfy the polynomiality condition [25] when n is odd. In order to satisfy this condition one needs to add a so-called D-term $D(x,\xi)$. Physically, the D-term represents the exchange of a quantum number 0^+ between the photon and the nucleon. It can thus be interpreted as the exchange of two pions.

The D-term is defined in the interval $(-\xi,\xi)$ and is an odd function of x/ξ.

1.7 Experimental context

GPDs have been the subject of intense theoretical development since the mid-90s [10, 11, 26, 27, 28, 29]. DVCS generated a huge interest, as the simplest process giving access to GPDs. Excellent reviews can be found in references [5, 12, 30, 24].

1.7.1 Published results in DVCS

Attracted by the theoretical interest in DVCS, experimental groups from HERA and Jefferson Lab re-analyzed available data to look for lepto-production events. They all succeeded in extracting a signal from data.

In the high energy domain, where DVCS dominates over BH, H1 [31] and ZEUS [32] at HERA were able to determine the reduced cross section from data (Fig. 1.9). In this energy regime gluons are dominant, and these experiments are sensitive to the gluon GPDs described in section 1.4.1. At lower energy, in the regime where the BH dominates, the HERMES [34] and CLAS [35] collaborations have both determined the single beam spin asymmetry (SSA), shown in Fig. 1.10.

Technically, even if these experiments show evidence of DVCS events in their data sample, no interpretation in terms of GPDs is legitimate at this point. The handbag dominance mechanism needs to be proven. Several tests have been proposed in the literature [38]. They basically consist of testing the Q^2-dependence of different observables. However, the low statistics of the non-dedicated experiments described above do not allow a test of this assumption. From an experimental point of view, the identification of the DVCS channel was never ideal, as these experiments were not planned to study this specific reaction.

However, these early non-dedicated experiments proved the feasibility of DVCS measurements using available facilities, and paved the way to improved experimental setups.

1.7.2 Dedicated DVCS experimental program

The first dedicated experiment (E00-110) aimed at measuring DVCS ran in Hall A at Jefferson Lab in 2004 [39], and is the subject of this thesis. Its first goal is to test the handbag dominance in the regime $Q^2 \sim 1.5 - 2.5\,\mathrm{GeV}^2$ and $x_B \sim 0.36$. If this is the case, a linear combination of GPDs will be extracted from its high statistics data. At the beam energy of Jefferson Lab (5.75 GeV), the BH dominates the cross section. It is through a cross section difference with polarized electrons of opposite helicities that we will be able to access the imaginary part of the DVCS amplitude, and potentially interpret the result in terms of a linear combination of GPDs. Fig. 1.11 shows a simple layout of the detector configuration for the E00-110 DVCS experiment. The 5.75 GeV polarized electron beam of CEBAF scatters on a 15 cm-long LH_2 target. The scattered electron is detected in the Hall A High Resolution Spectrometer (HRS), the real photon in an electromagnetic calorimeter and the recoil proton in a plastic scintillator array. The experimental setup will be described in more detail in chapter 2.

Another experiment ran in Hall A immediately after E00-110, using a slightly different setup on a deuterium target in order to measure DVCS on the neutron [40]. In 2005 a third dedicated DVCS experiment was performed using the large acceptance spectrometer CLAS in the Hall B of Jefferson Lab [41], which covered a larger kinematical domain but with lower resolution and luminosity. Additional dedicated DVCS experimental programs will start soon at HERMES [42] and H1 [43], with improved experimental setups. The COMPASS collaboration at CERN has also expressed an interest in running a DVCS program [44].

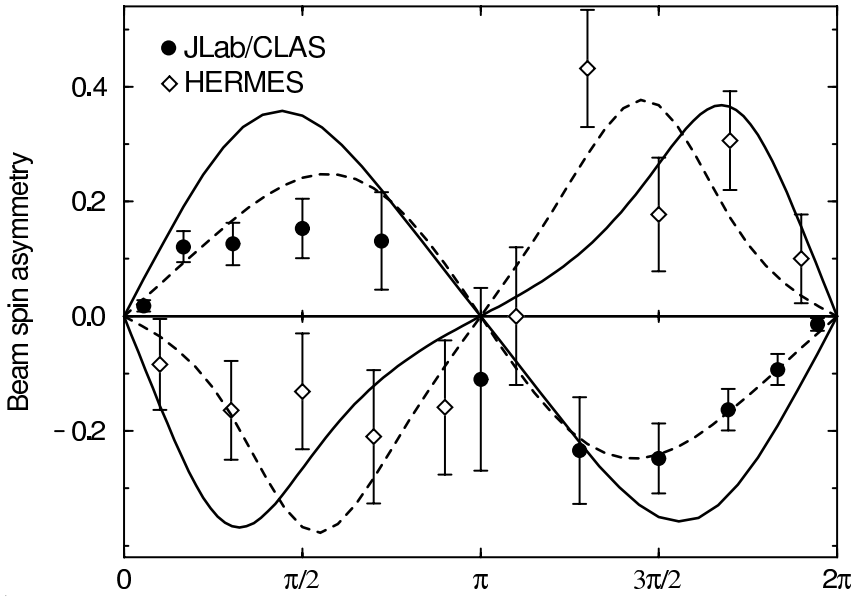

Figure 1.10: Dependence of the beam spin asymmetry as a function of the azimuthal angle between the leptonic and hadronic planes from both the HERMES [34] and CLAS [35] experiments. The opposite sign is explained by the opposite charge of the lepton beam used at the two facilities. GPD models [36, 37] have been overlayed (solid lines) and show that theory and data are in fairly good agreement. Dashed lines show a phenomenological fit to the data.

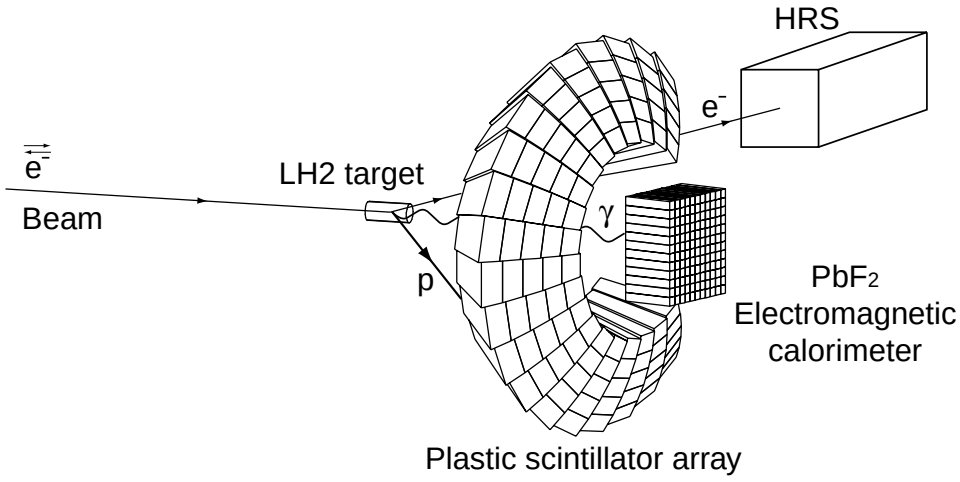

Figure 1.11: E00-110 schematic setup showing the three different detectors used to measured each of the particles in the final state.

Chapter 2

Experimental setup

The DVCS experiments took place in Hall A at Jefferson Lab from September 21st to December 9th 2004, including both DVCS on the proton (E00-110) and DVCS on the neutron (E03-106). I describe in this chapter the experimental setup used in E00-110, beginning with a short description of the Continuous Electron Beam Accelerator Facility (CEBAF) [45] at Jefferson Lab and the instrumentation of Hall A [46].

2.1 Jefferson Lab

CEBAF (figure 2.1) was originally designed to accelerate electrons up to 4 GeV by recirculating the beam up to five times through two superconducting linacs, each producing an energy gain up to 400 MeV per pass. Electrons are injected into the accelerator from a photocathode gun capable of providing highly-polarized electrons. The polarized gun consists of a strained GaAs cathode, which was illuminated during the DVCS experiment by a 499 MHz Ti-Sapphire laser, operated at 850 nm. The polarization is measured at the injector with a 5 MeV Mott polarimeter and the polarization vector can be oriented with a Wien filter. The current to the three experimental Halls A, B and C can be controlled independently. Each linac contains 20 cryomodules with a design accelerating gradient of 5 MeV/m. Ongoing in situ processing has already resulted in an average gradient in excess of 7 MeV/m, which has made it possible to accelerate electrons up to 6 GeV. The design maximum current is 200 μA CW (Continuous Wave), which can be split arbitrarily between three interleaved 499 MHz bunch trains. One bunch can be peeled off after each linac pass to any of the Halls using RF separators and septa. All Halls can simultaneously receive the maximum energy beam.

2.2 Hall A

The DVCS experiment took place in the Hall A of Jefferson Lab, which is dedicated to high luminosity and precision measurements. The core of the Hall A equipment is a pair of identical 4 GeV/c High Resolution Spectrometers (HRS). Both devices provide a momen-

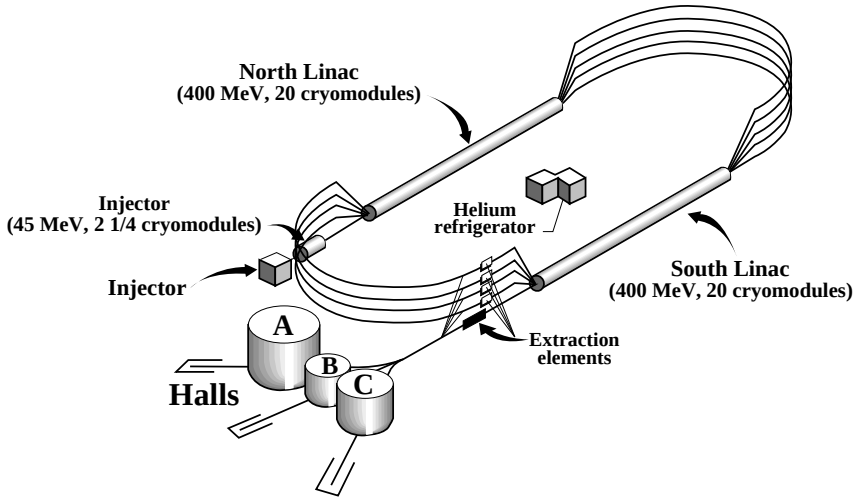

Figure 2.1: Layout of the CEBAF facility. The electron beam is produced at the injector by illuminating a photocathode and then accelerated to 45 MeV. The beam is then further accelerated in each of the two superconducting linacs, through which it can be recirculated up to five times. The beam can be extracted simultaneously to each of the three experimental halls.

tum resolution of better than $2 \cdot 10^{-4}$ and a horizontal angular resolution of better than 2 mrad at a design maximum central momentum of 4 GeV/c. The magnet configuration is of a QQDQ type with a vertical bend: a pair of superconducting quadrupoles followed by a 6.6 m long dipole and a third superconducting quadrupole.

2.2.1 The detector package

The detector packages of the two spectrometers are designed to perform various functions in the characterization of charged particles passing through. They are located in the shield huts at the top of the HRS (see figure 2.2). Their configuration can change from one experiment to another. I describe here the configuration used during the DVCS experiment.

The left HRS was equipped with two planes of scintillators, S1 and S2, separated by a distance of about 2 m. Each plane is composed of six and sixteen overlapping paddles respectively, made of thin plastic scintillator to minimize hadron absorption. Each scintillator paddle is viewed by two photomultipliers (PMTs). A gas Čerenkov detector filled with CO_2 at atmospheric pressure [47] and two layers of shower detectors allow the identification of negative pions and electrons. Tracking information is provided by a pair of Vertical Drift Chambers (VDCs), described in detail in reference [48].

The trajectory of particles is defined at the focal plane by four variables, two positions and two angles, reconstructed from the drift chambers:

- x_{fp} and y_{fp}, positions of the particle in the dispersive and transverse directions respectively,

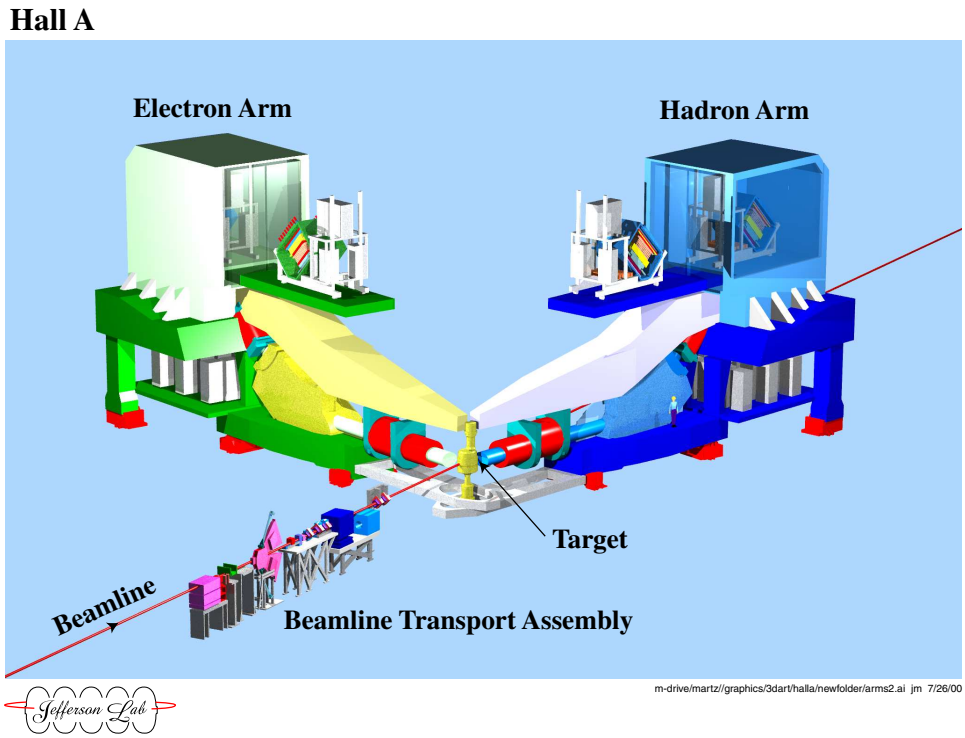

Figure 2.2: Schematic layout of Hall A showing both HRS and their detector packages, as well as the beamline.

- ϕ_{fp} and θ_{fp}, the horizontal and vertical angles of the particle.

The track variables of the reconstructed particle in the HRS reference frame are:

- dp, momentum of the particle relative to the HRS nominal momentum P_0,
- y_{tg}, coordinate along the horizontal axis perpendicular to the spectrometer,
- ϕ_{tg}, horizontal Cartesian angle of the particle with the HRS axis,
- θ_{tg}, vertical Cartesian angle of the particle with the HRS axis.

These reconstructed variables are obtained from the measured angular and spatial coordinates at the focal plane using an optics matrix, which can be determined experimentally during special calibration runs.

The right HRS was only used as a luminosity monitor during the experiment, with a very basic detector package: a pair of scintillator planes and VDCs.

2.2.2 Beamline

The instrumentation along the beamline consists of various elements necessary to measure the relevant properties of the beam. Special attention is paid to the control and determination of the beam energy, current and polarization, and also to the position, direction,

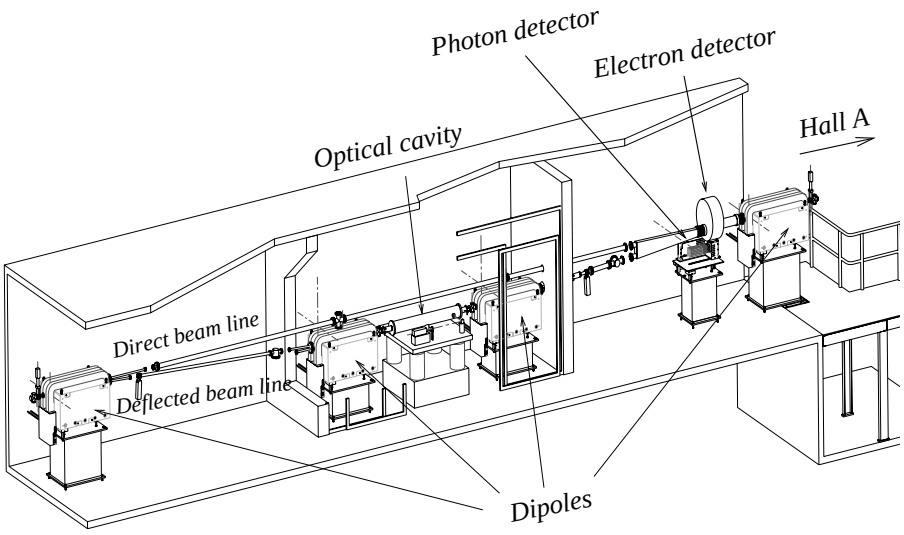

Figure 2.3: Schematic layout of the Compton polarimeter, showing the four dipoles of the chicane, the optical cavity and the photon and electron detector.

size and stability of the beam at the target location. I will briefly detail here the elements that were useful to the DVCS experiment.

2.2.2.1 Polarimeters

Compton polarimeter The Compton polarimeter [49], utilizing the process of Compton scattering, can measure the beam polarization concurrently with experiments. The polarization is extracted from the measurement of the counting rate asymmetry for opposite beam helicities in the scattering of a circularly polarized photon beam by the electron beam.

Installed at the entrance of the Hall, the Compton polarimeter consists of a magnetic chicane, a photon source, a photon calorimeter, and an electron detector as shown in figure 2.3. The electron beam is deflected vertically by the four dipoles of the chicane and crosses the photon beam at the Compton interaction point. The interaction takes place at the center of a resonant Fabry-Pérot cavity, where a primary 230 mW CW Nd:YaG laser beam ($\lambda = 1064\,\mathrm{nm}$) is amplified to 1200 W. After interaction, the backscattered photons are detected in the calorimeter and the electrons in the silicon strip electron detector located a few mm above the primary beam in the front of the fourth dipole. Electrons that did not interact exit the polarimeter and reach the target.

The statistical error of a Compton measurement is inversely proportional to the square root of the number of events and to the analyzing power of the polarimeter, which is basically proportional to the electron beam energy. For our beam energy and current,

a 1% statistical error could be achieved in 2.5 h of data taking. However, this is far from being the limiting factor. Since the Compton data was taken during normal DVCS running, we can average over long periods of time in order to make the statistical error negligible.

Møller polarimeter A Møller polarimeter exploits the process of Møller scattering of polarized electrons off polarized atomic electrons in a magnetized foil. The reaction cross section depends on the beam and target polarizations. The Møller polarimeter uses a ferromagnetic foil, magnetized in a magnetic field of about 24 mT along its plane, as a target of polarized electrons. The target foil can be tilted at various angles to the beam in the horizontal plane, providing a target polarization that has both longitudinal and transverse components, to permit determination of a transverse component of the beam polarization. The spin of the incoming electron beam may have a transverse component due to precession in the accelerator and in the extraction arc.

The Møller scattering events are detected with the help of a magnetic spectrometer consisting of a sequence of three quadrupole magnets and a dipole magnet. The detector consists of lead-glass calorimeter modules, split into two arms in order to detect two scattered electrons in coincidence. The helicity-driven asymmetry of the coincidence counting rate is used to derive the beam polarization.

The polarization measurements with the Møller polarimeter are invasive, and one measurement typically takes an hour, providing a statistical accuracy of about 0.2%.

Systematic uncertainties of the polarimeters The most important systematic uncertainties of the two polarimeters are different. The dominant uncertainty of the Møller polarimeter comes from the uncertainty in the target polarization while that of the Compton polarimeter comes from its analyzing power. Another uncertainty comes from the fact that the Møller polarimeter has to use a low beam current (0.5 μA, typically). The current is reduced at the injector, either by attenuating the laser light or with a slit at the chopper. Each of these techniques might change the beam polarization. In contrast, the Compton polarimeter is used at the same current as the experiments. At energies of a few GeV the main systematics uncertainties of the Compton polarimeter come from the knowledge of the detectors' calibration and resolution in the determination of the mean analyzing power. In the measurement of the Compton asymmetry, special care must be taken to minimize the sensitivity to helicity-correlated beam parameters, like the beam position. The background depends critically on the beam tune. The Møller polarimeter is insensitive to this class of uncertainties. At the energy of our experiment, the total systematic error of the Compton measurement was 2%, while it was 3% for the Møller polarimeter.

2.2.2.2 Beam position monitors

In order to determine the position and direction of the beam at the target location, two Beam Position Monitors (BPMs) are used, one located 7.524 m and the second 1.286 m

upstream of the target. Each transverse coordinate of the beam centroid is calculated from the ratio of the difference to the sum voltages on a pair of diametrically opposed antennas. The relative position of the center of the beam centroid can be determined to within 100 μm for currents above 1 μA. The absolute position of the beam can be determined from the BPMs by calibrating them against wire scanners which are located adjacent to each of the BPMs. The wire scanners are surveyed with respect to the Hall A coordinates at regular intervals.

2.2.2.3 Beam current monitor

The Beam Current Monitor (BCM) of Hall A is designed to provide a stable, low-noise, non-interfering beam current measurement. Two RF cavities and an Unser monitor are enclosed in a temperature-stabilized box to improve magnetic shielding. The Unser monitor is a Parametric Current Transformer, which provides an absolute reference. This monitor is calibrated by passing a known current through a wire inside the beam pipe. As the Unser monitor's output signal drifts significantly on a time scale of several minutes, it cannot be used to monitor the beam current continuously.

The two resonant RF cavity monitors on either side of the Unser Monitor are stainless steel cylindrical waveguides tuned to the frequency of the beam (1.497 GHz) resulting in voltage levels at their outputs that are proportional to the beam current.

2.2.2.4 Absolute energy measurements

The beam energy can be measured by two independent methods [50]: the Arc and eP methods. The Arc method determines the energy by measuring the deflection of the beam in the arc section of the beamline. The measurement is made when the beam is tuned in dispersive mode in the arc section. The momentum of the beam is then related simply to the field integral of the eight dipoles and the net bend angle of the beam through the arc section.

The method consists of two simultaneous measurements, one for the magnetic field integral of the bending elements (eight dipoles in the arc), based on a reference magnet (9th dipole) measurement, and the actual bend angle of the arc, based on a set of wire scanners. A measurement of the beam energy made during the experiment using the Arc method resulted in the value $E_b = 5757.2 \pm 0.1 \pm 0.1$ MeV.

The eP method utilizes a stand-alone device along the beamline located 17 m upstream of the target. In this method, the beam energy is determined by measuring the scattered electron angle and the recoil proton angle in the ^{1}H(e,e'p) elastic reaction.

The eP system consists of two identical arms, each of which contains an electron and a corresponding proton detector system, made up of a set of 2×8 silicon micro-strip detectors in the reaction plane. Both arms are placed symmetrically with respect to the beam along the vertical plane. Simultaneous measurements of the beam energy with both arms result in the cancellation, to first order, of uncertainties in the knowledge of the position and direction of the beam.

The eP measurement could not be used during the DVCS experiment as the instrumentation was not fully operational at that moment.

2.2.3 The target system

2.2.3.1 The scattering chamber

A custom-made scattering chamber was built for the DVCS experiment. It was thinner than the usual scattering chamber in Hall A. Also, a larger exit beam pipe was constructed. The scattering chamber is made of a 1 cm spherical shell of aluminum, permitting low energy protons to penetrate it (minimum momentum of 305 MeV, corresponding to a cut on the kinematic variable t of -0.091 GeV^2). Moreover, the new scattering chamber accommodates the spherical symmetry of the reaction and makes energy losses independent of the scattering angle. The larger exit beam pipe reduces the background.

2.2.3.2 Cryogenic target

The cryogenic target system is mounted inside the scattering chamber along with the sub-systems for cooling, gas handling, temperature and pressure monitoring, target control and motion, and an attached calibration and solid target ladder. The basic cryogenic target has three independent target loops, two of which were used for the DVCS experiment: a liquid hydrogen (LH_2) loop and a liquid deuterium (LD_2) loop[1]. Each of the two liquid loops had a cylindrical aluminum target cell, 15 cm long, mounted on the target ladder. The sidewalls of the cells were about 178 μm thick, while the entrance and exit windows were approximately 102 and 127 μm thick, respectively. The operating temperature and pressure of the LH_2 target is 19 K and 0.17 MPa, resulting in a density of about 0.0723 g/cm^3. The targets are arranged in a vertical stack, which can be moved from one position to another by remote control. The solid target ladder contained the following targets:

- **Optics:** Seven 1 mm thick carbon foils used mainly for optics calibration of the HRS.
- **Two dummy targets:** $\pm$2 cm and $\pm$7.5 cm Al foils to study target walls effects.
- **Cross hair:** Aluminum foil with a milled cross, used to measure beam position with respect to the target.
- **BeO:** It allows to see the beam spot at the target through a camera installed in the scattering chamber.
- **C:** 1 mm thick carbon.

[1]The deuterium loop was only used during experiment E03-106, running just after the experiment described herein.

- **Empty:** Position used to reduce radiation on detectors while beam was used for other purposes (Moller and eP runs, beam size measurements using wire scanners and other beam tunings).

The cryogenic target can take up to 130 μA of beam current. In this configuration, the beam heating alone deposits 700 W in the target . The maximum luminosity achieved is over $5{\cdot}10^{38}\,\mathrm{cm}^{-2}/\mathrm{s}$. This is far more than necessary for the DVCS experiment, which was designed to run at $10^{37}\,\mathrm{cm}^{-2}\,\mathrm{s}^{-1}$, i.e. 2.25 μA.

2.3 Electromagnetic calorimeter

The left HRS was used to measure the scattered electron in the DVCS experiment. The emitted photon and the recoil proton of the DVCS reaction were detected in two dedicated detectors built for the experiment. This section describes the electromagnetic calorimeter.

2.3.1 General characteristics

The electromagnetic calorimeter consists of an array of 11×12 PbF_2 blocks, each measuring $3 \times 3 \times 18.6\,\mathrm{cm}^3$. PbF_2 is a very dense material ($7.77\,\mathrm{g/cm}^3$), which allow a very compact detector. The radiation length of PbF_2 is 0.95 cm and its Molière radius is 2.2 cm. Thus, more than 99.9% of the photon energy is absorbed in the crystals (19.6 radiation lengths) and a typical electromagnetic shower is contained in 9 adjacent blocks.

Each block is wrapped in Tyvek© (internal wrapping) and Tedlar© (external wrapping). The Čerenkov photons emitted in each block by the charged particles of the electromagnetic shower are collected by Hamamatsu R7700 PMTs. Around 1000 Čerenkov photons are emitted per GeV (Monte Carlo simulation estimate).

2.3.2 Gain monitoring system

In order to monitor gain variations of individual channels, a system based on Light Emitting Diodes (LEDs) was designed. A remotely controlled carriage holding the whole system can be moved in front of each of the blocks. In order for this carriage to move in front of the crystals, the calorimeter needs to be retracted by 45 cm centimeters. This motion is also remotely controlled.

Three pulsed and one continuous LEDs are integrated in the board. The pulsed LEDs can be simultaneously and individually turned on or off, thus allowing the testing of the linearity of each channel (see results in section 4.2.2). The continuous LED was used to simulate the low energy background noise in the PMTs and check their gain variation as a function of their anode current. In addition to the LED system, a UV lamp was incorporated into the carriage. Turning it on for a few hours cures crystals from radiation damage.

This system also provides a relative calibration of each channel. Since the light emitted by the LED is constant, the high voltage (HV) of each PMT can be adjusted to get the

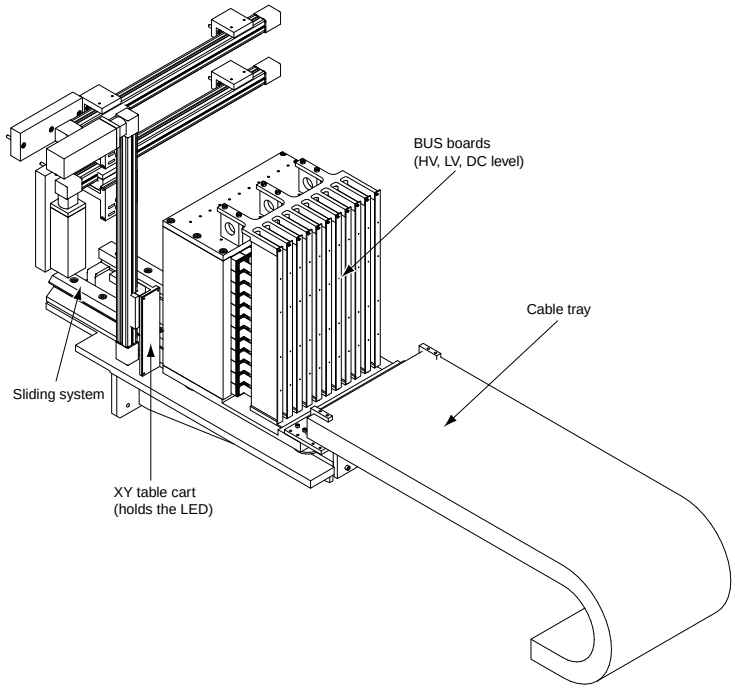

Figure 2.4: Calorimeter layout (backside view). The LED carriage of the monitoring system, as well as the system to control its motion, are schematically shown.

same output signal in each block, matching overall gains. Figure 2.4 shows a schematic layout of the calorimeter, together with the LED monitoring system.

I contributed to the installation and tests of this system and some results and discussion will be presented later in section 4.2.2.

2.4 Proton detector

The hadronic part of the DVCS reaction has an azimuthal symmetry around the virtual photon (which has an almost fixed direction, as explained in section 2.3.1). The proton detector takes advantage of this symmetry, and consists of a set of 100 EJ200 plastic scintillator blocks, arranged in 20 towers of 5 blocks each. Its azimuthal coverage is 270° around the average virtual photon direction and its polar coverage is 20°, from 18° to 38° with respect to the average virtual photon. There is a 90° azimuthal cut-out in this detector on the beam side (see figure 2.5) in order to accommodate the exit beam pipe in the setting where the detector is located closest to the beamline. The minimum polar angle of 18° is necessary in order not to interfere with the calorimeter and the choice of the maximum polar angle of 38° was determined by the very small cross section value for large values of $-t$.

Both the calorimeter and proton detector were equipped with a DC current monitoring system. The low energy background can be very damaging to the detectors. It mainly

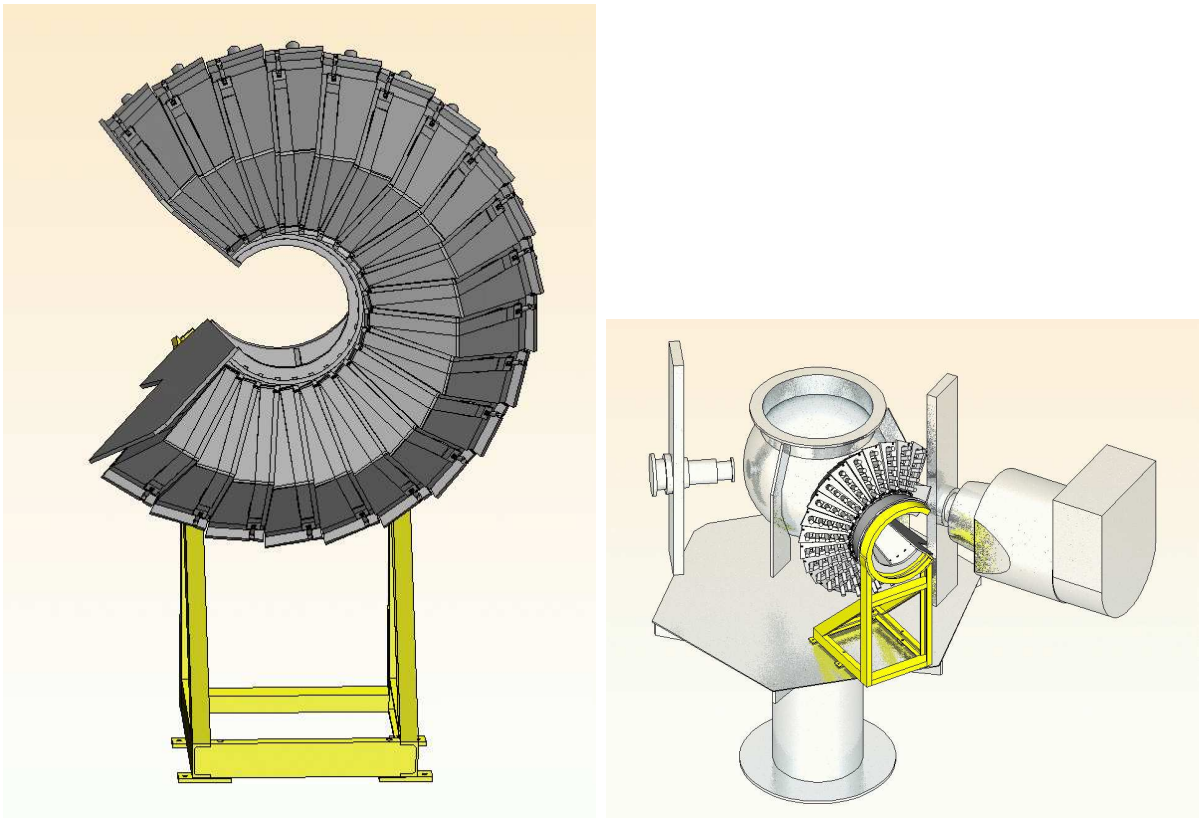

Figure 2.5: Proton array layout (left), where the polar segmentation is not visible. The right figure shows its relative position to the scattering chamber and the left HRS. The exit beam pipe (not shown) goes in between these two detectors.

comes from Møller electrons and low energy photons. The light they produce is seen as a continuous component by PMTs, similar to a light leak. This affects both the gain of the PMTs and their lifetime. The continuous LED system in the calorimeter was designed to measure the effect of a light leak on the PMT gains, and results that will be presented later will show that the gain variation remained below 1% for the anode currents measured during the experiment. DC current was monitored constantly during the experiment to ensure PMT gain stability and the lifetime of PMTs during the whole experiment.

2.5 Control systems

A distributed system based on the application framework of the Experimental Physics and Industrial Control System (EPICS) is used to monitor and control various elements of the Hall A instrumentation. EPICS is also used at JLab to monitor and control the accelerator. For the DVCS experiment, the motion of the calorimeter and the LED gain monitoring system was controlled by EPICS, as was the HV and DC current monitors for each detector channel.

The value of any EPICS variable, such as the HV of PMTs or the position of the LED carriage in front of the calorimeter, can easily be added to the data stream at regular intervals.

2.6 Data acquisition

In addition to two dedicated detectors, a new data acquisition system was designed and built in order to fulfill the very special requirements of the DVCS experiment in terms of background noise and counting rates. I will very briefly describe the standard data acquisition system in Jefferson Lab and the Hall A, and then in some more detail the one used for the DVCS experiment.

2.6.1 Data acquisition in Jefferson Lab and the Hall A

The data-acquisition (DAQ) system in Hall A uses CODA (CEBAF On-line Data Acquisition System), developed by the JLab data-acquisition group. Supported hardware elements are mainly commercially available electronics, including front-end Fastbus and VME digitization devices, single-board VME computers, 100BaseT Ethernet networks, Unix or Linux workstations, and a mass storage tape silo (MSS). The commercial software elements are the VxWorks operation system which runs on the VME computers, and either SunOS or Linux on the workstations. Custom hardware elements made at JLab include the trigger supervisor that synchronizes the read-out of the front-end crates and handles the dead-time logic of the system. The most important custom software components of CODA are the read-out controller (ROC), which runs on the front-end crates, the event builder (EB) and event recorder (ER), which run on a Unix or Linux workstation, the event transfer (ET) system, which allows distributed access to the data on-line or insertion of data from user processes, and finally the RunControl process, which allows users to select different experimental configurations and to control the experiment data taking.

For each event, which corresponds to a trigger accepted by the trigger supervisor, data are gathered from the front-end boards by the ROC component, which buffers the data in memory and sends these buffers via the network to the EB running on a workstation. The EB builds events from fragments sent by the various ROCs and passes them to the ER, which writes data to a local disk. The data are subsequently written to tapes in the MSS. Using the ET system, various additional pieces of data are inserted into the data stream every few seconds from the control system, scalers, or text files of information.

2.6.2 DVCS DAQ

Two new crates running two ROCs were used to read-out the calorimeter and proton detector data. The front-end electronics used to record the data from these detectors were specifically designed for this application.

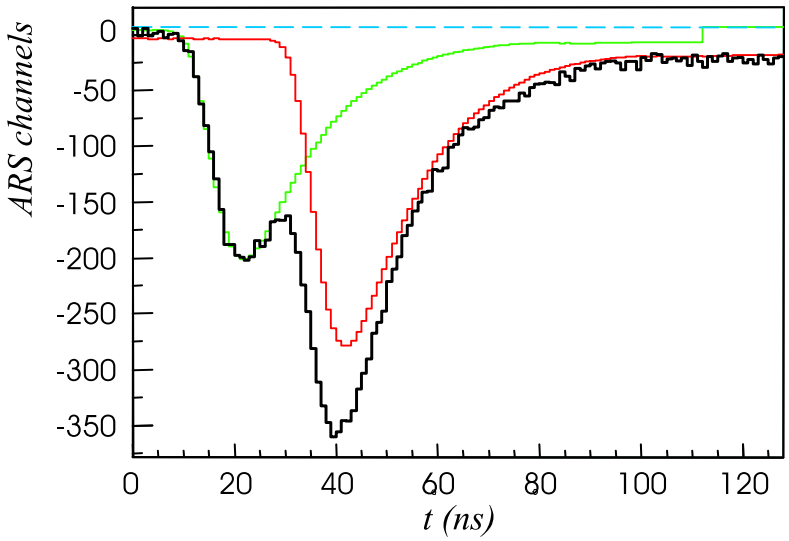

Figure 2.6: PMTs signals are recorded in a 128 ns window at a sampling rate of 1 GHz. The offline treatment of this data allows to resolve pile-up events, as the one shown in this figure.

Due to the high luminosity of the experiment ($10^{37}\,s^{-1}cm^{-2}$) and the location of the detectors at small angles from the beamline and close to the target (some blocks of the calorimeter are at 6° and 1.1 m from the target in one of the kinematic settings), high single rates, up to 10 MHz, were expected. With pile-up events (like the one shown in figure 2.6), conventional ADCs would give very inaccurate results. In order to cope with pile-up and attain sufficient energy and position resolutions, a system based on the Analog Ring Sampler (ARS) [51] chip was designed.

2.6.2.1 The Analog Ring Sampler

The Analog Ring Sampler consists of an array of 128 capacitor cells, which continuously sample the signal. Some of the cells are in the track state (connected to the signal), and some are in the hold state (isolated). Cells are cleared when they are switched to the track state. At any time, the last tens of nanoseconds of the input signal are recorded in the cells in hold state. The number of hold cells is a constant number determined by a 7-bit input bus of the circuit.

Memory cell switches are controlled by command signals coming from an internal loop delay line. The sampling frequency is defined by the elementary delay between two consecutive command signals, and was 1 GHz in our experiment.

When a signal STOP is received, the ARS stops overwriting. Until the memory is full, the last cells in track state continue to switch to the hold state while none of the cells already in hold state are cleared. Sampling is completely stopped when all the cells are in hold state. The signal is then stored in the array of capacitors, with the charge of each

capacitor proportional to the value of the input signal. If a new signal VALID is received, the charge on each of the capacitors is digitized using flash-ADCs and the information transfered to the data stream.

This digitalization allows the recording of the signal of each channel for every event over 128 ns as in a digital oscilloscope. Figure 2.6 shows a typical example. This data can then be treated offline to resolve pile-up events (see section 3.2).

The ARS system generates a large amount of data. Each sample is digitized by an 11-bit ADC. If all channels are read for every event, it implies for a typical coincidence rate of 50 Hz, a data rate of 2 Mbytes/s. The transfer of this large amount of data at every trigger has an impact on the acquisition system deadtime. As it was mentioned in section 2.3.1, a typical electromagnetic shower is contained in only 9 calorimeter blocks. In order to reduce the amount of data by recording and reading only the interesting electronic channels of the calorimeter, a dedicated trigger module was designed for the experiment. Its main characteristics are described in the following section.

2.6.2.2 Calorimeter trigger module

DVCS detectors are located in a high background environment as they are unshielded and in direct view of the target at a small angle to the beamline and a small distance from the target. DVCS photons, however, are very energetic (over 1.5 GeV). A high threshold can be set in the calorimeter as a whole. On the other hand, an electromagnetic shower develops exponentially in the detector, which means that even though 9 blocks are typically hit, more than 90% of the energy is deposited in the central block, and only very little energy is deposited in the surrounding blocks. An individual block threshold is not well suited.

In order to account for the topology of the electromagnetic shower, the calorimeter trigger module works in the following way. When an external signal is received (typically a good electron candidate has been detected in the HRS), it integrates the signal of each calorimeter PMT in a time window (chosen to be about 60 ns during the experiment), using 7-bit flash-ADCs. It then computes the sum of these ADC values for every set of 2×2 neighboring blocks (see figure 2.7 left). Note that these sets overlap. The sum of the 4 neighboring blocks is coded in 8 bits. Only the ARS corresponding to 2×2 sets above a threshold will be recorded.

The right plot in figure 2.7 shows a typical example. The numbers shown in each calorimeter block correspond to the result of the fast integration of each channel signal. Most blocks are at their pedestal values (around 8 or 9 ADC channels). Some low energy noise is present all over the calorimeter, but only 4 overlapping sets of 2×2 blocks are above threshold (set to 57 ADC channels during most of the experiment, corresponding to around 1 GeV of energy). The 9 corresponding ARS will be recorded. Note that blocks with low signals will generally not be read. However, they will be recorded if they are next to a high energy block, as low energy blocks are important to the energy and position resolution of the main cluster.

The time the calorimeter trigger module takes to make a decision on whether any

11	23	35	47	59	71	83	95	107	119	131
10	22	34	46	58	70	82	94	106	118	130
9	21	33	45	57	69	81	93	105	117	129
8	20	32	44	56	68	80	92	104	116	128
7	19	31	43	55	67	79	91	103	115	127
6	18	30	42	54	66	78	90	102	114	126
5	17	29	41	53	65	77	89	101	113	125
4	16	28	40	52	64	76	88	100	112	124
3	15	27	39	51	63	75	87	99	111	123
2	14	26	38	50	62	74	86	98	110	122
1	13	25	37	49	61	73	85	97	109	121
0	12	24	36	48	60	72	84	96	108	120

9	9	8	10	9	10	8	9	8	8	10
11	10	11	11	9	12	11	9	9	8	9
9	8	9	9	9	8	8	8	9	6	9
9	9	10	9	8	9	7	8	9	10	9
9	8	8	10	9	10	8	8	7	17	8
9	8	8	9	9	9	8	9	5	4	12
9	8	8	9	9	10	11	8	8	7	10
9	10	9	15	9	9	12	9	41	15	5
9	9	9	9	10	9	9	7	14	12	10
9	9	8	8	9	10	8	10	10	8	12
9	10	10	9	9	9	9	8	7	9	9
9	8	9	9	9	9	10	7	8	8	8

Figure 2.7: Calorimeter showing block numbers and two examples of overlapping sets of 2×2 neighboring blocks (left). The sum of ADC values in each set are computed and compared to a threshold. ARS belonging to sets above threshold will be recorded. A typical event is shown in the right, where each block is labeled with the result of the fast ADC integration. Four overlapping sets are above threshold in this example and the 9 corresponding blocks (highlighted in yellow) will be read.

ARS needs to be recorded or not is 340 ns (17 counts of a 50 MHz clock). This module is based on 4 FPGAs (Field Programmable Gate Array), very flexible user-programmable logic-array chips.

2.6.2.3 DVCS trigger and readout

The experiment trigger works in two steps. The first step is defined by the HRS, whose trigger is set on an S1–S2 coincidence. In order to reduce the number of HRS triggers due to negative pions, the Čerenkov detector in the HRS was also in the trigger during most of the experiment.

When the HRS fires (indicating a good electron candidate), all ARS are *stopped* (but not yet read) and the calorimeter trigger module is started. It integrates all calorimeter PMT signals following the procedure described in section 2.6.2.2. After 340 ns a decision whether to read the calorimeter ARS or not is available. The two possible outcomes are illustrated in figure 2.8. If none of the blocks need to be read (most of the time), a fast clear of all ARS is made, with a total dead time of around 500 ns. If at least one set of 2×2 blocks is above threshold (indicating a good photon candidate), then the readout of the corresponding ARS is started. The digitalization and transfer of the data imply a dead time of about 128 μs in this case.

Due to the small acceptance of the HRS and the kinematics of the DVCS reaction,

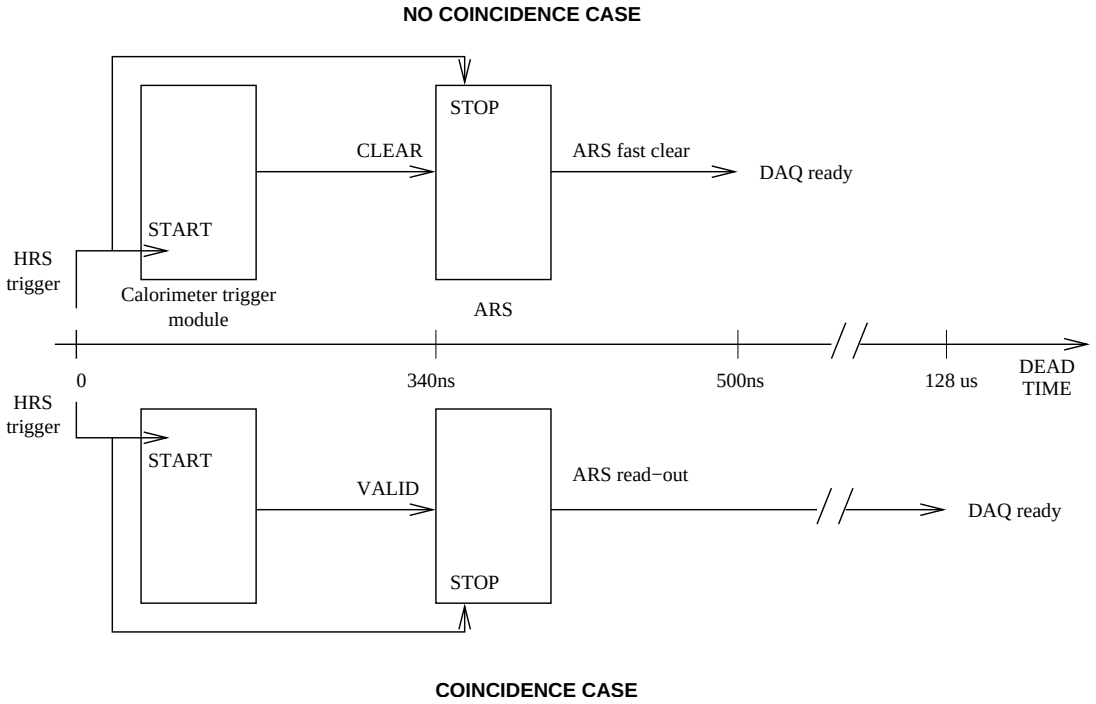

Figure 2.8: Schema of the DVCS trigger. HRS trigger stops all ARS and starts the calorimeter trigger module, which takes a decision whether to read ARS or not in 340 ns. If no ARS needs to be read, a fast clear is made with a total dead time of 500 ns. When ARS are read out, DAQ is busy during 128 μs.

the *virtual* photon is always emitted in a very small angular region, around which the calorimeter is centered. The fictitious impact point of the virtual photon in the calorimeter is constrained to its four central blocks. The proton detector is not in the trigger and is read at every HRS–calorimeter coincidence. As the virtual photon has an almost fixed direction, the approximate region of the proton detector that a DVCS proton would hit can be inferred knowing only which calorimeter region was hit by the photon. The choice of which proton detector region (which blocks) should be read can then be made on the fly out of the information provided by the calorimeter trigger module. The accuracy of this prediction is dominated by a convolution of the HRS acceptance and the calorimeter energy resolution. Processes like multiple scattering in the target and the scattering chamber can also affect the accuracy of the prediction. The look-up table of proton detector blocks to read as a function of calorimeter ones was computed using a Monte Carlo simulation based on GEANT 3.21 (see chapter 5 for more details), which included a realistic description of all the elements of the experimental setup. Figure 2.9 shows the proton detector map determined and used in the experiment. The detector inefficiency for DVCS protons due to this map is smaller than 0.1%. Depending on the kinematic setting, between 15% and 30% of the proton detector blocks needed to be read on average. This reduces the amount of data recorded and therefore the acquisition dead time. Note that no threshold was set in any of the proton detector channels, so that even very low energy

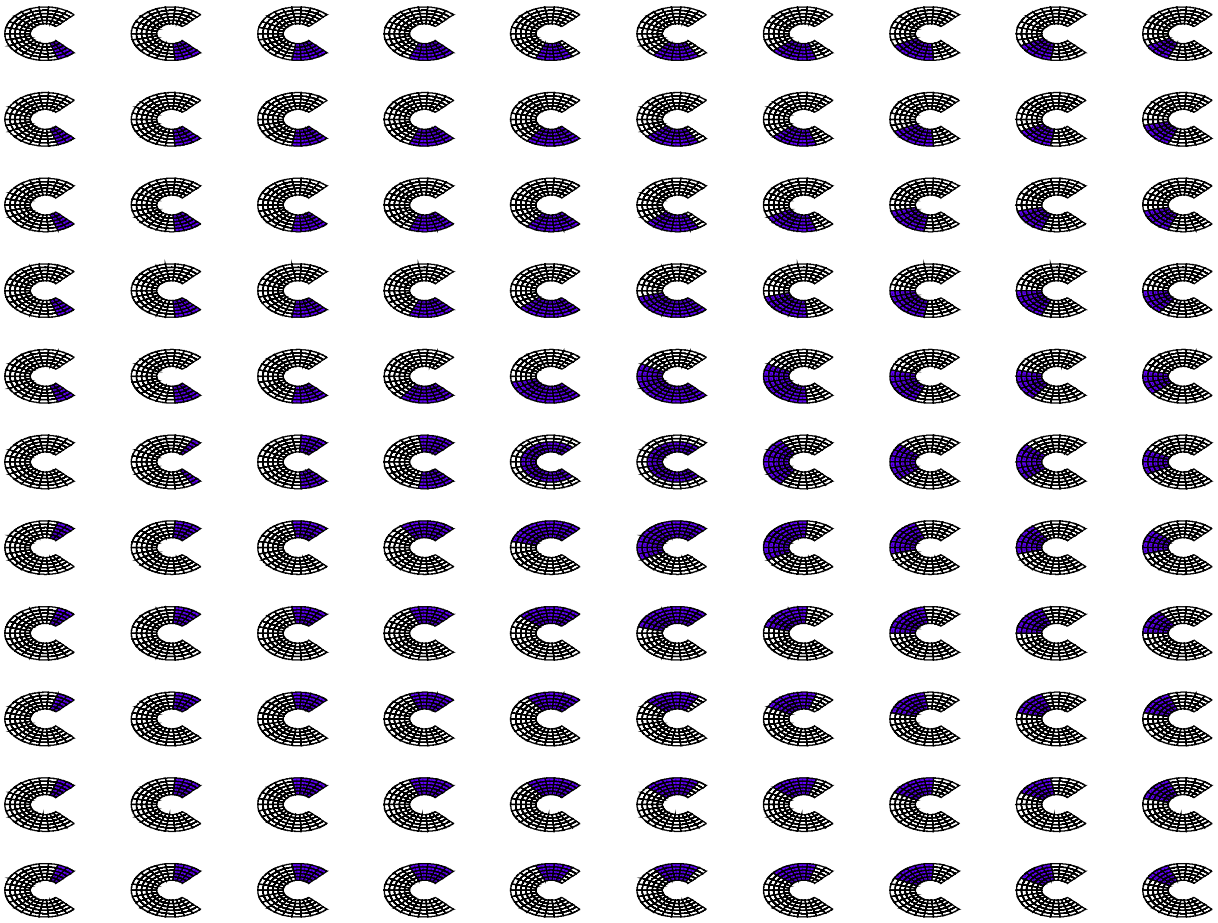

Figure 2.9: Proton detector blocks to be read as a function of the 2×2 calorimeter set which fired. Note that the number of 2×2 sets in each direction is one less than the number of calorimeter blocks (cf. Fig. 2.7).

protons could be detected. The communication between the calorimeter and proton array crates necessary for this block selection in the proton detector was made possible by a multiplexer module (MUX) that allowed the calorimeter trigger module to send its data to the proton array crate.

2.7 E00-110 kinematic settings

In order to test the dominance of the handbag mechanism, necessary to make the theoretical connection between DVCS and GPDs, three kinematical settings at 3 different values of Q^2 and fixed x_B were made in the E00-110 experiment.

With an electron beam energy of 5.75 GeV and the several constraints of the experimental apparatus, we develop here the 3 optimal kinematical settings for this experiment.

We consider the kinematics of the leptonic reaction

$$e^-(k) \to e^-(k')\,\gamma^*(q)\,. \tag{2.1}$$

In the laboratory frame the four-momenta of the particles are

$$k = (E_b, 0, 0, E_b)\,, \tag{2.2}$$
$$k' = (|\vec{P}_e|, |\vec{P}_e|\sin\theta_e, 0, |\vec{P}_e|\cos\theta_e)\,, \tag{2.3}$$
$$q = (\nu, |\vec{q}|\sin\theta_{\gamma^*}, 0, |\vec{q}|\cos\theta_{\gamma^*})\,, \tag{2.4}$$

where E_b is the electron beam energy, $\vec{P}_e$ is the scattered electron momentum, $\vec{q}$ is the virtual photon momentum, θ_e is the angle between the scattered electron and the beam direction, and θ_{γ^*} is the angle between the virtual photon and the electron beam. We have neglected the electron mass.

Using energy and momentum conservation in reaction (2.1), we can write $\cos\theta_{\gamma^*}$ as a function of two pairs of variables: (s,x_B) and (Q^2,x_B), which allow the identification of the experimental constraints:

$$\cos\theta_{\gamma^*} = \frac{1 + Mx_B/E_b}{\sqrt{1 + 4M^2x_B^2/Q^2}}\,, \qquad \cos\theta_{\gamma^*} = \frac{1 + Mx_B/E_b}{\sqrt{1 + \dfrac{4M^2x_B^2(1-x_B)}{(s-M^2)x_B}}}\,. \tag{2.5}$$

Fig. 2.10 (top) shows θ_{γ^*} as a function of x_B for $E_b = 5.75$ GeV.

Similarly, we obtain the expression for $|\vec{P}_e|$ as a function of θ_e and the relevant invariants of the reaction: Q^2, $s = (q+p)^2$, and the Bjorken variable x_B (p is the four-momentum of the target proton, which in the laboratory frame is $p = (M, 0, 0, 0)$):

$$|\vec{P}_e| = \frac{Q^2}{2E_b(1-\cos\theta_e)}\,,$$
$$|\vec{P}_e| = \frac{E_bMx_B}{E_b(1-\cos\theta_e) + x_BM}\,,$$
$$|\vec{P}_e| = \frac{M^2 - s + 2ME_b}{2[M + E_b(1-\cos\theta_e)]}\,. \tag{2.6}$$

Figure 2.10 (bottom) shows $|\vec{P}_e|$ as a function of θ_e and Q^2, s and x_B.

The electromagnetic calorimeter is centered along the direction of the virtual photon γ^*. Several kinds of constraints exist. Geometrical constraints for the positions of detectors in the Hall imply:

$$\theta_e \geqslant 14^\circ \tag{2.7}$$
$$\theta_{\gamma^* e} \geqslant 26.5^\circ \tag{2.8}$$
$$\theta_{\gamma^*} \geqslant 14^\circ \tag{2.9}$$

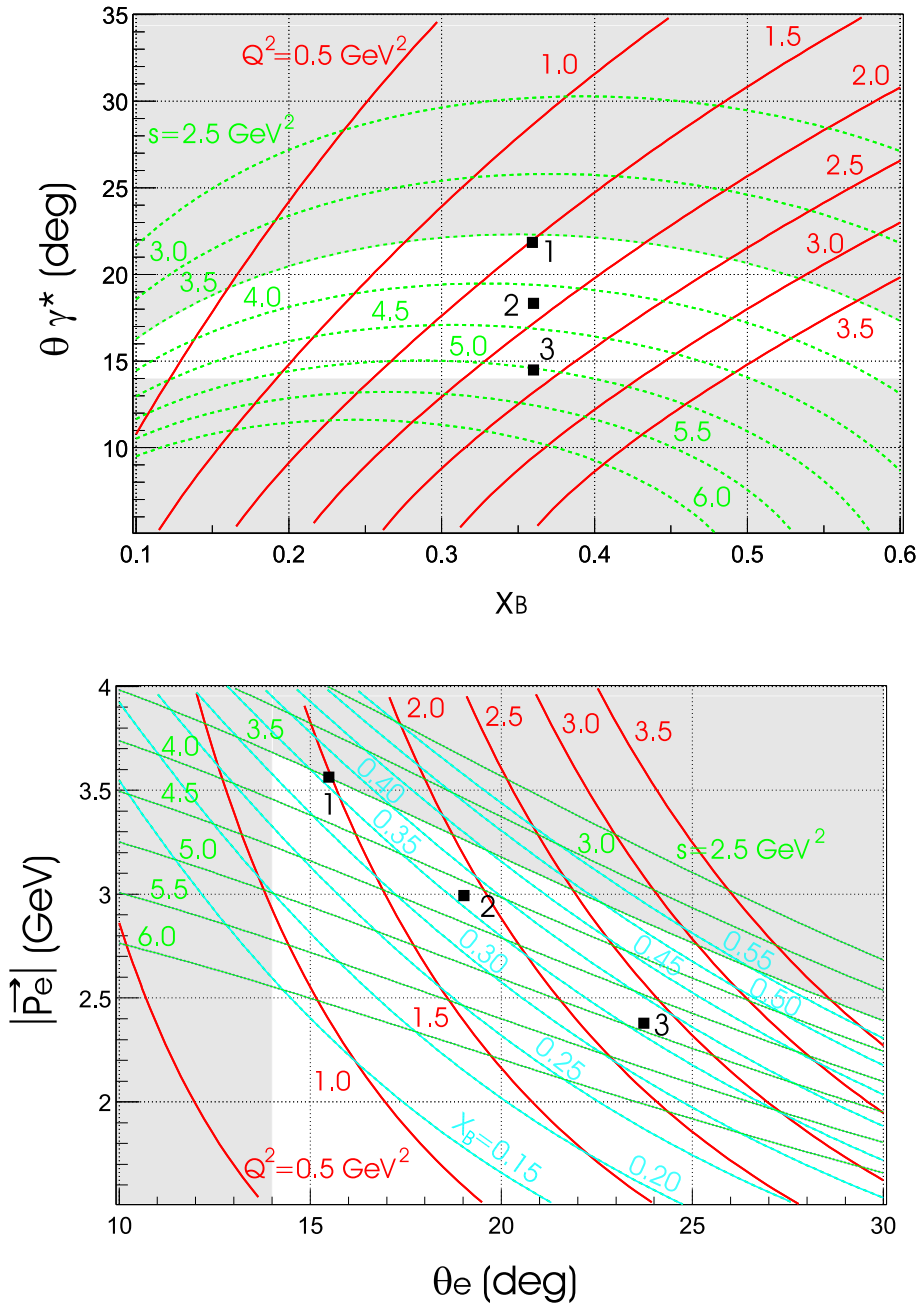

Figure 2.10: Top: angle between the virtual photon and the electron beam as a function of x_B; curves for constant Q^2 and constant s are also plotted. Bottom: scattered electron momentum magnitude as a function of the scattering angle; curves for constant Q^2, constant s and constant x_B are also plotted. Shadowed zones in both figures correspond to regions not accessible due to experimental constraints.

s (GeV^2)	Q^2 (GeV^2)	x_B	θ_e (deg.)	θ_{γ^*} (deg.)	P_e (GeV)
3.5	1.5	0.36	15.6	22.3	3.6
4.2	1.9	0.36	19.3	18.3	2.9
4.9	2.3	0.36	23.9	14.8	2.3

Table 2.1: Three kinematical settings of the E00-110 experiment. With the aim of testing the handbag dominance, 3 different Q^2 setting were chosen to maximize the highest Q^2 value and Q^2 range studied, while remaining above the main nucleon resonances.

where $\theta_{\gamma^* e}$ is the angle between the scattered electron and the virtual photon.

To ensure that the data are from the deep inelastic scattering regime (with the nuclear excitation well above) we require

$$s \geqslant 3.5 \text{ GeV}^2 . \tag{2.10}$$

Finally, the maximum momentum measurable by the spectrometer implies:

$$|\vec{P}_e| \leqslant 4 \text{ GeV} . \tag{2.11}$$

All these constraints have been represented as shadowed zones in Fig. 2.10. In the allowed areas we have searched for three kinematical points at different Q^2 and constant x_B. The 3 squared points in the figure represent the 3 kinematics chosen. With the aim of testing the handbag dominance, 3 different Q^2 setting were chosen trying to maximize the highest Q^2 value and Q^2 range, remaining above the main resonances. In Tab. 2.1 we summarize these kinematics.

Chapter 3

Analysis methods

This chapter describes the different methods used to analyze data from each of the detectors. The dedicated detectors required the development of specific tools, such us the waveform analysis algorithm to treat ARS data. The calorimeter and proton array analysis tools will be the main focus of this chapter. For completeness, some details on the HRS analysis will be presented first.

3.1 High Resolution Spectrometer

We can divide the HRS analysis into two main parts described in the following sections: the tracking, done by the Vertical Drift Chambers (VDCs), and the optics transformation of the track from the detector package back to the interaction point.

As mentioned in section 2.2.1, two detectors were installed in the HRS during the experiment for particle identification: a gas Čerenkov and a two-layer shower counter. Particle identification, which is a key issue in inclusive experiments, is not as relevant for an exclusive experiment as ours. Indeed, the detection of a recoil proton verifying the kinematics of a DVCS event, greatly reduces the possibility of mistaking the electron for some other particle.

3.1.1 VDC analysis

The HRS detector package was described in section 2.2.1. When a charged particle passes through a VDC plane, it ionizes the gas in the chamber. Ions and electrons generated in this process drift and generate an avalanche close to the wires, inducing an electrical signal that is preamplified and sent to discriminators and then TDCs. VDC clusters consist of hits with consecutive wire numbers. To allow for inefficiencies, clusters are allowed to have gaps of one wire without a TDC hit. There are typically four to six wires hit in a cluster.

In principle, tracks can be reconstructed using only the cluster center coordinates, but better resolution can be obtained by analyzing the TDC information. The TDCs directly measure the time between the ionization and the arrival of the signal at the wire (the "drift

time"). The extraction of precise drift distances from the measured drift times requires the knowledge of the non-linear relationship between them, which is parametrized by a fourth-order polynomial with fitted coefficients based on calculations or empirically based on data. Once the drift distances to each wire are known, the cross-over point of the track in the wire plane can be determined very accurately by a linear fit.

If multiple clusters are found in a wire plane, an algorithm to reconstruct each of the tracks is used [46]. Multiple-track events are less than 10% of the triggers, and their analysis is very complex. However, the ratio of multi-track events to single-track events is well defined, and so the inefficiency due to omitting multi-track events can be readily calculated (see chapter 6). We will discard multi-track events altogether in the present analysis.

Once the track through the VDC has been determined in terms of wire plane coordinates, it is advantageous to convert the track coordinates to detector coordinates: x_{det} and y_{det}, and their corresponding angular coordinates, θ_{det} and ϕ_{det}.

3.1.2 Momentum and vertex reconstruction

For each event, two angular coordinates (θ_{det} and ϕ_{det}) and two spatial coordinates (x_{det} and y_{det}) are measured by the focal plane detectors. The position of the particle and the tangent of the angle made by its trajectory along the dispersive direction are given by x_{det} and θ_{det}, while y_{det} and ϕ_{det} give the position and tangent of the angle perpendicular to the dispersive direction. These focal plane variables are corrected for any detector offsets from the ideal central ray of the spectrometer to obtain the focal plane coordinates x_{fp}, θ_{fp}, y_{fp}, and ϕ_{fp}. Theses observables are used to calculate x_{tg}, θ_{tg}, y_{tg}, ϕ_{tg} and δ_{tg} for the particle at the target by inverting the transport matrix that describes the optics of the spectrometer (δ_{tg} is the fractional deviation of the momentum of the trajectory from the HRS central trajectory). To first order, the transport matrix has the following design values (in meters, dimensionless, and fractional δ's) at the focus:

$$\begin{pmatrix} x_{fp} \\ \theta_{fp} \\ y_{fp} \\ \phi_{fp} \\ \delta_{fp} \end{pmatrix} = \begin{pmatrix} -2.48 & 0.0 & 0.0 & 0.0 & 12.4 \\ -0.15 & -0.40 & 0.0 & 0.0 & 2.04 \\ 0.0 & 0.0 & -0.40 & -1.30 & 0.0 \\ 0.0 & 0.0 & 0.54 & -0.78 & 0.0 \\ 0.0 & 0.0 & 0.0 & 0.0 & 1.0 \end{pmatrix} \cdot \begin{pmatrix} x_{tg} \\ \theta_{tg} \\ y_{tg} \\ \phi_{tg} \\ \delta_{tg} \end{pmatrix}. \tag{3.1}$$

Notice that the transverse matrix is neither point to point (rays that come from the same interaction point are focused to a single point at the detector: $\langle y|\phi_{tg}\rangle = 0$), nor parallel to point (rays that are parallel to each other at the interaction point are focused to the same point at the detector: $\langle y|y_{tg}\rangle = 0$). This compromise was driven by the need for a simultaneous good resolution in the transverse position, y_{tg}, and angle, ϕ_{tg}. In practice, the expansion of the focal plane coordinates is performed up to fifth order. A set of tensors Y_{jkl}, T_{jkl}, P_{jkl} and D_{jkl} link the focal-plane coordinates to target coordinates. For

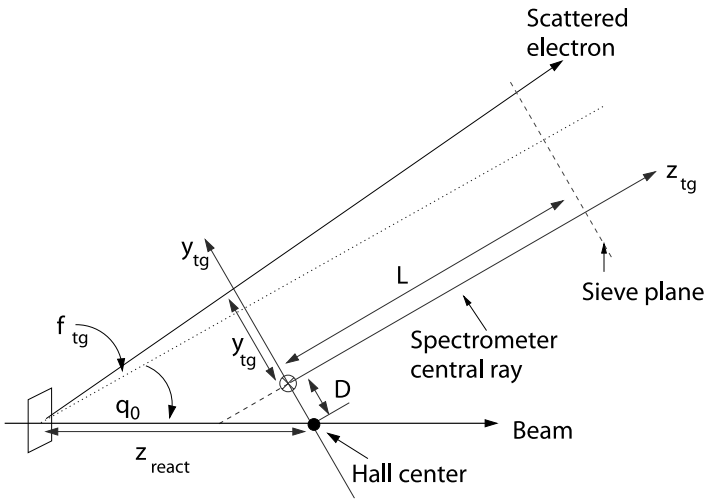

Figure 3.1: Target coordinate as seen from above. L is the distance from the Hall center to the HRS sieve plane, while D is the horizontal displacement of the spectrometer axis from its ideal position. Spectrometer central angle is denoted by Θ_0. Note that x_{tg} is vertically down (into the page).

instance:

$$y_{tg} = \sum_{j,k,l} Y_{jkl} \theta_{fp}^j y_{fp}^k \phi_{fp}^l, \qquad \text{where} \qquad Y_{jkl} = \sum_{i=0}^{m} C_i x_{fp}^i. \tag{3.2}$$

If the interaction point is not known, there are more unknowns (five) than observables (four). For a very thin target, by measuring the beam position and direction, the interaction point can be known. This is basically the way matrix elements are calculated during optics calibration runs. For extended targets, such as the ones used in the DVCS experiment, the HRS cannot simultaneously determine the particle momentum and the interaction point at the target. The approach used consists of assuming a small-acceptance, pointing-type spectrometer. It is assumed that the spectrometer only reconstructs the position at the target transverse to the bend plane (y_{tg}) with relatively high precision; x_{tg} is considered equal to zero. The vertex is then defined as the intersection point of the "track plane" and the beam ray. The "track plane" is the plane spanned by the reconstructed momentum vector and the transport x-axis (vertical) whose origin is the y_{tg} point (cf. Fig. 3.1). The beam ray is given by the measured beam positions and angles for the event. The spectrometer pointing offset is taken into account in this calculation.

Assuming $x_{tg} = 0$ and calculating the interaction point as mentioned before, we can now compute x_{tg}. This value of x_{tg} is then used to correct the momentum of the detected particle and θ_{tg} (extended target corrections). If we note with the superscript i the elements of the inverse of the first-order transport matrix, we can write

$$x_{tg} = \langle x|x\rangle^i x_{fp} + \langle x|\theta\rangle^i \theta_{fp} + \langle x|\delta\rangle^i \delta_{fp}\,, \tag{3.3}$$

and so

$$\delta_{fp} = \frac{-\langle x|x\rangle^i x_{fp} - \langle x|\theta\rangle^i \theta_{fp}}{\langle x|\delta\rangle^i} + \frac{x_{tg}}{\langle x|\delta\rangle^i}\,, \tag{3.4}$$

the second term of equation (3.4) being the correction. A similar calculation yields the correction of θ_{tg}:

$$\theta_{tg}^{corrected} = \theta_{tg} + x_{tg}\frac{\langle\theta|\delta\rangle^i}{\langle x|\delta\rangle^i}\,. \tag{3.5}$$

3.2 Waveform analysis

This section describes the algorithm we have developed to analyze ARS data (see [52] for more details). It is the key element of the raw data analysis, and will be described in detail. Its principle is common to both the calorimeter and the proton array.

3.2.1 Ideal case

The algorithm is based on the assumption that the signal *shape* is independent of its amplitude. For an ideal event without noise, there are only two free parameters, the amplitude of the pulse and the arrival time. If we know the arrival time $t = 0$, the amplitude a which best fits the signal $\{x_i\}$ is simply given by the one which minimizes

$$\chi^2 = \sum_{i=0}^{127}(x_i - ah_i)^2, \tag{3.6}$$

where $\{h_i\}$ is the reference shape. Reference shapes for each individual PMT are determined experimentally from data, using elastic calibration runs, where the probability of pile-up is very small. The reference shape is basically the average shape of a pulse for each PMT.

We can now write:

$$\frac{\partial\chi^2}{\partial a} = -2\sum_{i=0}^{127}(x_i - ah_i)h_i = 0, \tag{3.7}$$

and so

$$a = \frac{\sum_{i=0}^{127} x_i h_i}{\sum_{i=0}^{127} h_i^2}. \tag{3.8}$$

The algorithm to compute the best amplitude is fast, as the equation is linear and the result is analytic. Note, however, that there are no constraints on the value of a. The fit amplitude can lead to a negative energy pulse in some cases.

Generally, the arrival time of the pulse is not known. In order to find it, we perform the fit described above for all possible arrival times where we expect the pulse to be, by

steps of 1 ns, the sampling of ARS[1]. This is done by shifting the reference shape of a time t. At each step of time, the amplitude which best fits the signal is given by an expression equivalent to (3.8), but now the reference shape is shifted in time:

$$a(t) = \frac{\sum_{i=0}^{127} h_{i-t} x_i}{\sum_{i=0}^{127} h_{i-t}^2} \,. \tag{3.9}$$

For every amplitude found by equation (3.9) we can compute the χ^2 of the fit:

$$\chi^2(t) = \sum_{i=0}^{127} (x_i - a(t) h_{i-t})^2 \,, \tag{3.10}$$

and we will define the arrival time of the signal as the time t where we found the minimum $\chi^2(t)$, and so the best fit.

3.2.2 Multi-pulse fit

In a more realistic case, a signal from an accidental event may interfere with the signal we want to measure. In this case of pile-up, the ARS tool is particularly useful to resolve events and improve both the time and energy resolution.

The algorithm used in the ideal case of a single pulse fit can be generalized to fit two pulses of two different amplitudes at two different arrival times. Again, if the arrival times of the pulses were known, say t_1 and t_2, the amplitudes which best fit each pulse can be obtained by minimizing

$$\chi^2 = \sum_{i=0}^{127} (x_i - a_1 h_{i-t_1} - a_2 h_{i-t_2})^2, \tag{3.11}$$

which yields the linear system

$$\frac{\partial \chi^2}{\partial a_1} = -2 \textstyle\sum_{i=0}^{127} (x_i - a_1 h_{i-t_1} - a_2 h_{i-t_2}) h_{i-t_1} = 0 \tag{3.12}$$

$$\frac{\partial \chi^2}{\partial a_2} = -2 \textstyle\sum_{i=0}^{127} (x_i - a_1 h_{i-t_1} - a_2 h_{i-t_2}) h_{i-t_2} = 0 \,. \tag{3.13}$$

[1]Note that choosing steps equal to the sampling of ARS is not necessary and we could go beyond 1 ns and look for arrival times more precisely.

This, in turn, can be written as follows:

$$\begin{pmatrix} \sum_{i=0}^{127} h_{i-t_1} x_i \\ \sum_{i=0}^{127} h_{i-t_2} x_i \end{pmatrix} = \underbrace{\begin{pmatrix} \sum_{i=0}^{127} h_{i-t_1} h_{i-t_1} & \sum_{i=0}^{127} h_{i-t_1} h_{i-t_2} \\ \sum_{i=0}^{127} h_{i-t_1} h_{i-t_2} & \sum_{i=0}^{127} h_{i-t_2} h_{i-t_2} \end{pmatrix}}_{M^h_{t_1,t_2}} \begin{pmatrix} a_1(t_1,t_2) \\ a_2(t_1,t_2) \end{pmatrix}. \tag{3.14}$$

The amplitudes a_1 and a_2 can be obtained by inverting the matrix $M^h_{t_1,t_2}$. Note that this matrix only depends on the reference shape and not on the signal actually recorded in the event, so its computation and inversion can be carried out once and for all at the beginning of the analysis to improve the algorithm speed.

In order to find the arrival times t_1 and t_2, the same procedure described in section 3.2.1 is applied. Every combination of times t_1 and t_2 is considered and the one which minimizes

$$\chi^2(t_1,t_2) = \sum_{i=0}^{127} (x_i - a_1(t_1,t_2) h_{i-t_1} - a_2(t_1,t_2) h_{i-t_2})^2 \tag{3.15}$$

is chosen.

The amplitude fits for all combinations of times t_1 and t_2 is fast (it is a linear fit). On the other hand, the search of the arrival times is time-consuming (every combination of times must be tested). The search of 3 pulses would be too slow and as we shall see, the energy resolution obtained with the algorithm described here (fitting up to 2 pulses) is better than 5% for DVCS photons in the kinematic setting 3 (highest background rates). Nonetheless, another degree of freedom can be added to this algorithm to account for any fluctuations of the baseline due to background noise. It will be described in section 3.2.3.

An important choice on the algorithm implementation is the decision of whether a multi-pulse fit is necessary or a 1-pulse fit is sufficient. This decision balances the energy resolution against the need for increased computation time. This choice will be made on the value of the χ^2 of the 1-pulse fit for the best arrival time found. This is a parameter to study carefully and more details will be presented later in the chapter.

Several optimizations of the algorithm presented above can be considered in order to improve its performance. First of all, instead of using the whole ARS window of 128 samples for the analysis, a smaller window size can be better. Indeed, calorimeter pulses are 20-30 ns wide and proton detector pulses are about 50 ns wide. A window of 128 ns is probably too large and reducing it may increase the quality of the fit: typically, we do not want our fit to be disturbed by a pulse very far from the one we are interested in. Only pile-up cases need to be handled with a 2-pulse fit.

The choice of whether to fit 2 pulses or not is made on the value of the χ^2 of a 1-pulse fit. However, we can compute this χ^2 in a different (smaller) window than the one used to compute the amplitude. If the fit is good enough around the signal maximum, it may not be necessary to make a 2-pulse fit: a bad quality of the fit around the pulse tail would hardly affect the fit amplitude or time.

Finally, it must be noted that the 2-pulse fit is singular for $t_1 = t_2$; an infinite number of pairs a_1 and a_2 minimize the χ^2. In practice, it is very difficult to resolve 2 pulses arriving very close to each other from a single, larger pulse. The result of a 2-pulse fit with arrival times very close to each other is not reliable. An additional parameter of the algorithm is the resolution $\Delta\tau$ of a 2-pulse fit. If $|t_1 - t_2| < \Delta\tau$, we would reject the results of a 2-pulse fit, keeping the more reliable single-pulse amplitude and arrival time.

3.2.3 Algorithm full implementation

For completeness, I describe here the full algorithm with all its free parameters and details. The basics were presented in the previous section.

3.2.3.1 Baseline fit

We will first of all fit a constant to the signal. Some channels will be recorded, but no physical signal may be present. The value

$$b = \frac{1}{(i_{max} - i_{min})} \sum_{i=i_{min}}^{i_{max}} x_i \tag{3.16}$$

minimizes

$$\chi^2 = \sum_{i=i_{min}}^{i_{max}} (x_i - b)^2 \,, \tag{3.17}$$

where $[i_{min}, i_{max}]$ is the portion of the ARS window that we will consider in our analysis, which I shall call analysis window hereafter. As mentioned before, it maybe interesting to make this window smaller than the full 128 samples of the ARS. The analysis window absolute position will be different for each electronic channel as for cabling issues the signal arrives at slightly different times in each channel with respect to the common stop. Also, the analysis window width will be different for the calorimeter and for the proton detector.

If the χ^2_t defined as

$$\chi^2_t = \sum_{i=\chi^2_{min}}^{\chi^2_{max}} (x_i - b)^2 \tag{3.18}$$

is smaller than a χ^2_0 threshold to be determined, a baseline fit will be considered good enough and no pulse is present. Even though in the case of a baseline fit it is less important, please notice that the limits where this χ^2 is computed, $[\chi^2_{min}, \chi^2_{max}]$, are in principle different from the analysis window $[i_{min}, i_{max}]$, which may be larger.

3.2.3.2 One-pulse fit

If the χ^2 of equation (3.18) is greater than χ^2_0, at least one pulse must be fit. For every possible arrival time $t_1^{min} \leq t_1 \leq t_1^{max}$, the amplitude $a_1(t_1)$ and the baseline $b(t_1)$ verifying

$$\begin{pmatrix} \sum_{i=i_{min}}^{i_{max}} x_i h_{i-t_1} \\ \sum_{i=i_{min}}^{i_{max}} x_i \end{pmatrix} = \begin{pmatrix} \sum_{i=i_{min}}^{i_{max}} h^2_{i-t_1} & \sum_{i=i_{min}}^{i_{max}} h_{i-t_1} \\ \sum_{i=i_{min}}^{i_{max}} h_{i-t_1} & \sum_{i=i_{min}}^{i_{max}} 1 \end{pmatrix} \begin{pmatrix} a_1(t_1) \\ b(t_1) \end{pmatrix} \tag{3.19}$$

minimize

$$\chi^2(t_1) = \sum_{i=i_{min}}^{i_{max}} (x_i - a_1(t_1) h_{i-t_1} - b(t_1))^2 . \tag{3.20}$$

For every t_1 we compute

$$\chi^2_t(t_1) = \sum_{i=\chi^2_{min}}^{\chi^2_{max}} (x_i - a_1(t_1) h_{i-t_1} - b(t_1))^2 . \tag{3.21}$$

The minimum χ^2_t found in the time window $t_1^{min} \leq t_1 \leq t_1^{max}$ is compared to a χ^2_1 threshold to be defined. If it is smaller than χ^2_1, a one pulse fit will be considered good enough.

3.2.3.3 Two-pulse fit

If the minimum χ^2_{min} of equation (3.21) for all $t_1^{min} \leq t_1 \leq t_1^{max}$ is greater than χ^2_1, at least two pulses must be considered. For every possible pair of arrival times t_1 and t_2, the amplitudes $a_1(t_1, t_2)$, $a_2(t_1, t_2)$ and the baseline $b(t_1, t_2)$ verifying

$$\begin{pmatrix} \sum_{i=i_{min}}^{i_{max}} x_i h_{t_1+i} \\ \sum_{i=i_{min}}^{i_{max}} x_i h_{i-t_2} \\ \sum_{i=i_{min}}^{i_{max}} x_i \end{pmatrix} = \begin{pmatrix} \sum_{i=i_{min}}^{i_{max}} h_{i-t_1} h_{i-t_1} & \sum_{i=i_{min}}^{i_{max}} h_{i-t_1} h_{i-t_2} & \sum_{i=i_{min}}^{i_{max}} h_{i-t_1} \\ \sum_{i=i_{min}}^{i_{max}} h_{t_1+i} h_{i-t_2} & \sum_{i=i_{min}}^{i_{max}} h_{i-t_2} h_{i-t_2} & \sum_{i=i_{min}}^{i_{max}} h_{i-t_2} \\ \sum_{i=i_{min}}^{i_{max}} h_{t_1+i} & \sum_{i=i_{min}}^{i_{max}} h_{i-t_2} & \sum_{i=i_{min}}^{i_{max}} 1 \end{pmatrix} \begin{pmatrix} a_1(t_1, t_2) \\ a_2(t_1, t_2) \\ b(t_1, t_2) \end{pmatrix} \tag{3.22}$$

minimize

$$\chi^2(t_1, t_2) = \sum_{i=i_{min}}^{i_{max}} (x_i - a_1(t_1, t_2) h_{i-t_1} - a_2(t_1, t_2) h_{i-t_2} - b(t_1, t_2))^2 . \tag{3.23}$$

For every t_1 and t_2 we compute

$$\chi^2_t(t_1,t_2) = \sum_{i=\chi^2_{min}}^{\chi^2_{max}} (x_i - a_1(t_1,t_2)h_{i-t_1} - a_2(t_1,t_2)h_{i-t_2} - b(t_1,t_2))^2 \,. \tag{3.24}$$

The minimum value of χ^2_t found in the range $t_1^{min} \leq t_1 \leq t_1^{max}$ and $t_2^{min} \leq t_2 \leq t_2^{max}$ will represent the quality of the fit. If smaller than a χ^2_2 (to be defined), a 2-pulse fit will be considered good enough. If not, we need to decide what to do with these events.

If the result of a 2-pulse fit is such that $|t_1 - t_2| < \Delta\tau$, the result of a 1-pulse fit is kept as the good one. The value of $\Delta\tau$ represents the algorithm resolution, which is unable to distinguish two pulses arriving very close to each other.

3.2.4 Algorithm parameters

The algorithm parameters will depend on each individual ARS channel. There will be a major difference between the proton array and the calorimeter channels, but even within the same detector the parameters may change. Let us summarize here the free parameters of the waveform analysis algorithm:

Analysis window	$[i_{min},i_{max}]$	*Channel dependent*
χ^2-window	$[\chi^2_{min},\chi^2_{max}]$	*Event and channel dependent*
1st-window	$[t_1^{min},t_1^{max}]$	*Event and channel dependent*
2nd-window	$[t_2^{min},t_2^{max}]$	*Event and channel dependent*

These intervals vary channel by channel, as it was mentioned before. Due to the cabling of each channel, the signal is expected at a slightly different time in each detector block. In addition to this, the last 3 intervals will change event-by-event, to correct for the time jitter of the ARS stop signal. Indeed, ARS recording is stopped by the S2 scintillator paddles in the HRS. Time-walk corrections and time corrections as a function of the track position in the paddle have been found to be of the order of 2 ns, which is larger than our time resolution. Therefore, corrections have been implemented [53]. However, it is not reasonable to make these corrections to the analysis window, as it would imply the computation of all matrices only dependent on the reference shape $M^h_{t_1,t_2}$ on an event-by-event basis.

The other parameters of the algorithm are $\Delta\tau$, χ^2_0, χ^2_1 and χ^2_2. The χ^2 thresholds will be dependent on the calibration coefficient of each individual channel. The χ^2 being an absolute quantity, it is larger for bigger signals. In order to make the thresholds homogeneous throughout the detector, χ^2 thresholds will be inversely proportional to the calibration coefficient of each channel.

The χ^2 thresholds will be given in GeV later in the text. They correspond to the integral of a signal of that energy. By setting $\chi^2_0 = 20$ MeV for example, we allow a 20 MeV signal to be fitted by a baseline and so neglected. In this sense, GeV units are more meaningful that ARS channels. Instead of normalizing the χ^2_t of equations (3.18), (3.21) and (3.24), the thresholds were normalized to a common value of GeV, depending

on the calibration coefficient of each channel, which also changes with time, as a function of the run number.

3.3 Electromagnetic calorimeter

3.3.1 Single cluster algorithm

The accuracy in the determination of the reaction kinematics depends crucially on the photon energy and position resolutions. The algorithm used to compute the photon energy and impact point on the calorimeter is explained in the following, starting by considering the case of only one particle hitting the calorimeter (single cluster).

The photon total energy E is taken to be the sum over the energy loss E_i in each of the calorimeter blocks:

$$E = \sum_i E_i \qquad E_i = C_i A_i \,, \tag{3.25}$$

where A_i is the signal amplitude collected in block i and C_i the calibration coefficient of the block.

The impact position x is calculated as the sum of blocks positions x_i weighted logarithmically by the relative energy loss in each of them:

$$x = \frac{\sum_i w_i \, x_i}{\sum_i w_i} \quad w_i = \max\left\{0, \left[W_0 + \ln\left(\frac{E_i}{E}\right)\right]\right\}. \tag{3.26}$$

The parameter W_0 allows tuning of the relative weight between blocks: as $W_0 \to \infty$ the weighting becomes uniform regardless of the energy loss in each block, whereas small values of W_0 give a larger relative weight to blocks with big energy losses. The value of W_0 fixes the energy loss threshold for blocks to be taken into account in the position determination: blocks with a relative energy loss less than e^{-W_0} are neglected in the calculation.

The calorimeter is placed at 110 cm from the 15-cm-long target. Corrections due to the vertex position in the target need to be done. Furthermore, the electromagnetic shower does not begin at the surface of the calorimeter, but at a certain depth. This depth is, in first approximation, independent of the incident particle energy. Taking these two effects into account, the position x given by equation (3.26) is corrected by:

$$x_{corr} = x\left(1 - \frac{a}{\sqrt{L_{vc}^2 + x^2}}\right) \tag{3.27}$$

where L_{vc} is the distance from the vertex to the calorimeter and a is the distance of the electromagnetic shower centroid to the calorimeter front face, taken along the direction of its propagation (cf. Fig. 3.2). The algorithm depends on two parameters, W_0 and a, which have been optimized first with a Monte Carlo simulation, but later with real data coming from the elastic runs (see chapter 4). The performance of this algorithm was tested using the elastic run data. We achieved a 2 mm resolution (σ) at 1.1 m and 4.2 GeV,

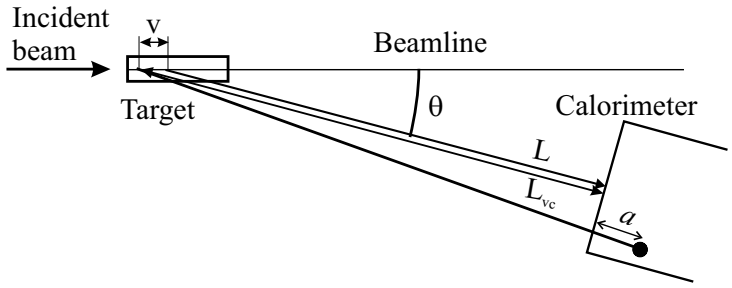

Figure 3.2: Vertex and shower depth corrections in calorimeter analysis. The distance L from the calorimeter to the center of the target is corrected by the vertex position v and is noted L_{vc}. The electromagnetic shower centroid is at a distance a from the calorimeter front face along the direction of its propagation.

which is compatible with the one obtained with Monte Carlo data: 3 mm at around 3 GeV. Thus, we manage to determine the photon position at the calorimeter front face with a resolution more than 10 times better than the individual block size.

3.3.2 Clustering algorithm

Several particles can hit the calorimeter during one event. These particles can come from the same reaction and arrive perfectly in time, such as the photons coming from a π^0 decay. No information in time can be used to separate each particle and a spatial clustering is then necessary to deal with this kind of event.

The decay of a π^0 is isotropic in the pion center-of-mass, but due to the Lorentz boost photon emission peaks in the forward direction. Often both photons coming from a π^0 decay will hit the calorimeter and generate two electromagnetic showers that partially overlap. The goal of the clustering algorithm is to separate blocks belonging to each of the two showers. The kinematics of the decay imply a minimum angle between the two photons in the lab frame. This minimum angle is 5° for a π^0 of 3 GeV, which means at least two calorimeter blocks between the impact points of each photon.

The algorithm used to separate clusters is based on a cellular automata [54]. The principle, illustrated in Fig. 3.3, is the following. Firstly, local maxima are identified (*viruses*). We then proceed by steps. At each step, every block (*cell*) gets the value of the highest energy neighbor (*it is infected*), with the rule that a cell which has already been infected by a virus, or by a cell which has itself been infected by a virus, does not change anymore. At the end, every cell will have the energy of one of the viruses. All cells with the same value will belong to the same cluster, to which the algorithm described in section 3.3.1 will be applied in order to calculate its energy and position.

Position resolution when two partially overlapping clusters are present is slightly worse than in the case of a single cluster. Application of this algorithm to simulated data demostrated a 4 mm spatial resolution.

			0.2		
			3.0	1.0	0.2
0.3	0.2	0.4	7.0	2.0	0.2
2.0	8.0	1.0	0.4		
0.2	0.6	0.3	0.2		

			3.0		
			7.0	7.0	2.0
8.0	8.0	8.0	7.0	7.0	2.0
8.0	8.0	8.0	7.0		
8.0	8.0	8.0	1.0		

			7.0		
			7.0	7.0	7.0
8.0	8.0	8.0	7.0	7.0	7.0
8.0	8.0	8.0	7.0		
8.0	8.0	8.0	8.0		

Figure 3.3: Illustration of the cellular automata procedure. At every step each cell takes the value of its highest energy neighbor. When a cell gets the value of one of the local maxima first determined, it does not change anymore. At the end of the process, all cells with the same value form a cluster.

3.3.3 Waveform analysis optimization

Calorimeter efficiency is very high, as will be shown later. Firstly, the electromagnetic shower develops over several blocks. Secondly, DVCS photons are very energetic (over 1.5 GeV); they are hardly missed even in the high background conditions of the experiment. However, the background has a huge impact on the energy and position resolutions: at 3 GeV energy resolution can vary from 3% to 6% within the calorimeter surface, depending on the distance to the beamline, which is directly related to the background rates.

The DVCS photon determines the kinematics of the reaction, together with the scattered electron, detected by the HRS. The resolution is limited by the calorimeter and using ARS electronics allows for a large improvement according to simulations. At 3 GeV we can go from 10% energy resolution with a classical ADC integrating the signal in a 60 ns window to 6% with ARS electronics for regions close to the beam (around 6° from the beamline). The difference is even larger at around 22° (the calorimeter region furthest from the beam line): 8% with ADCs while it is 3% with ARS (cf. Fig. 3.4 and Fig. 3.5).

Before the experiment started, the waveform analysis algorithm was studied and optimized using a Monte Carlo for the background and adding DVCS events coming from the Monte Carlo simulation of our experimental setup. The clustering and reconstruction algorithms described in the two previous sections were then applied, and the events were analyzed as would have been done with real data. By comparing the reconstructed events to the generated events at the vertex, resolutions and efficiencies were studied as a function of several waveform analysis parameters. The photon impact position in the calorimeter is also an interesting variable, as the resolution is very different for areas close to the beam and those away from it (see Fig. 3.4).

In order to study the influence of the χ^2 thresholds on the energy resolution, we first fixed both χ^2_0 and χ^2_1 to the same value ($\chi^2_0 = \chi^2_1 \equiv \chi^2_t$), and χ^2_2 very large ($\chi^2_2 \sim \infty$). The

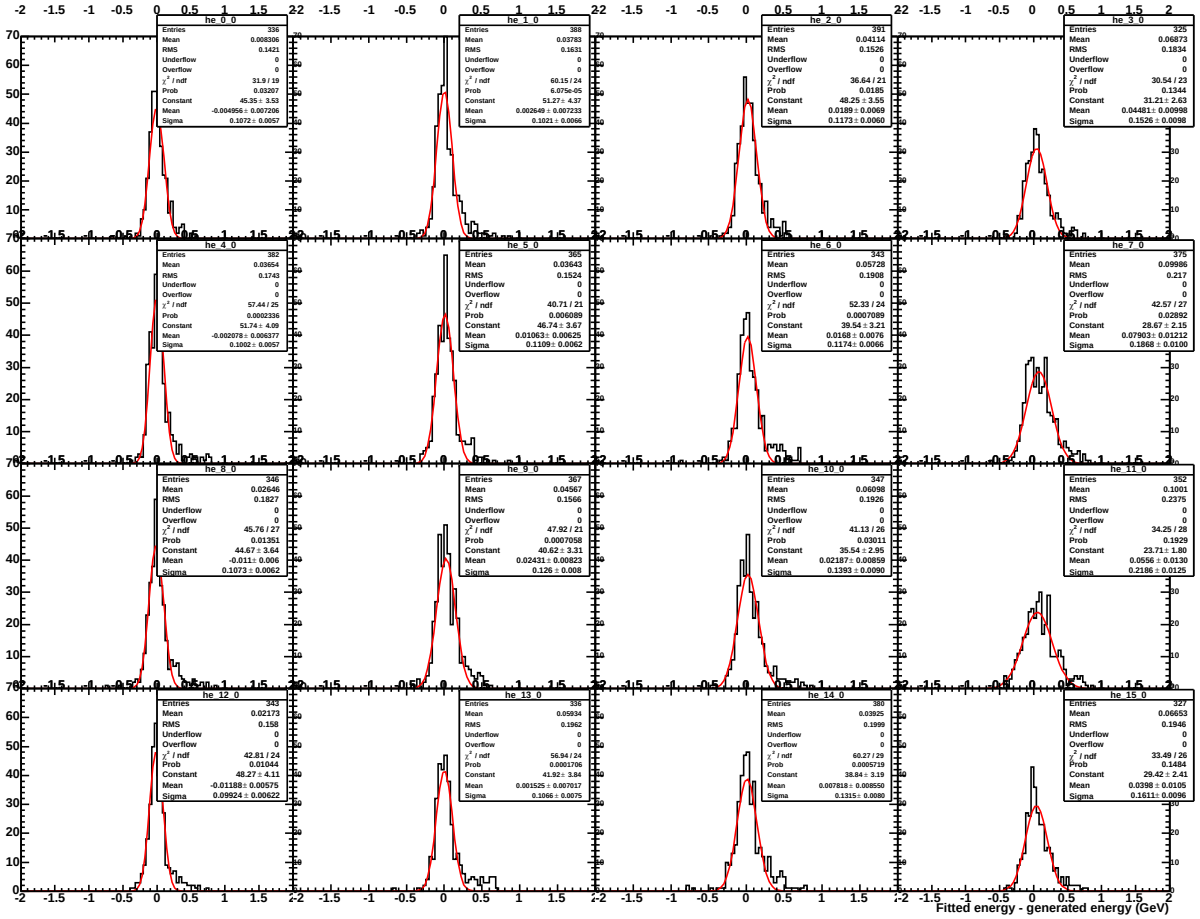

Figure 3.4: Reconstructed energy minus generated energy ΔE in GeV. Each histogram shows the energy resolution in a different region of the calorimeter surface: histograms on the right side correspond to the regions closest to the beam line and histograms on the left correspond to the areas furthest away. Events hitting one of the edge blocks are not considered. These resolutions were obtained by fitting 2 pulses most of the time: $\chi_0^2 = \chi_1^2 = 0.15$ GeV.

energy resolution (σ of distributions) is shown as a function of χ_t^2 for each region of the calorimeter in Fig. 3.5. Dashed lines show the resolutions we would have obtained with classical ADCs integrating the signal over 60 ns. For a value of $\chi_t^2 = 10\,\text{GeV}$, we then studied the independent variation of χ_0^2 and χ_1^2.

The value of χ_0^2 has the biggest impact on the energy resolution and must be sufficiently small. χ_1^2 can have a larger value to reduce computation time. Many other variables were studied as a function of these χ^2 thresholds in a similar manner: position resolution, missing mass resolution and efficiency. All of them present a similar behavior.

The effect of χ_2^2 was also studied. Neglecting blocks where the residual χ^2 of the fit was larger than χ_2^2 was not optimal. Indeed, not considering all blocks in the cluster drastically worsens the energy and position resolutions. The other option is to discard

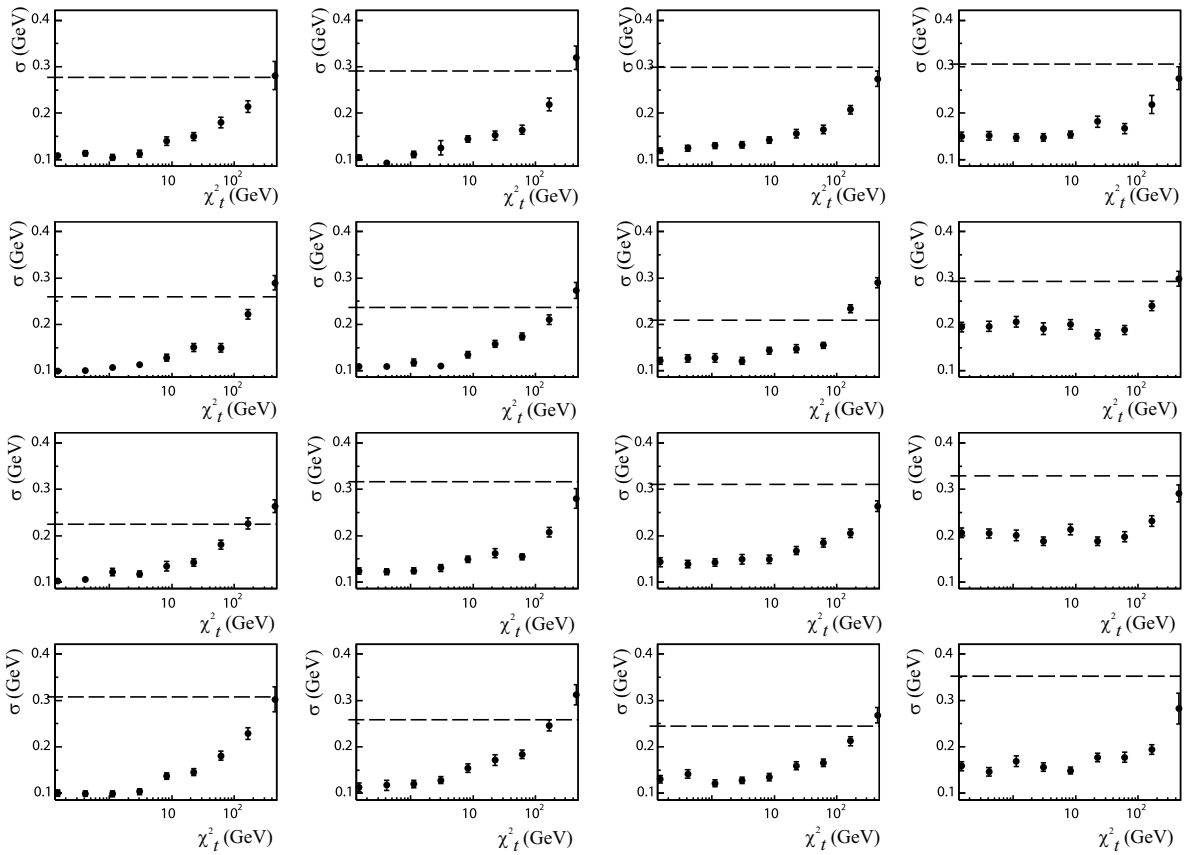

Figure 3.5: For each of the calorimeter regions, sigma's of the gaussian fits to the ΔE (GeV) distributions are plotted as a function of χ^2_t. RMS of distributions obtained integrating the signal over 60 ns (simulating classical ADCs) are represented by dashed lines. The resolutions obtained with ARS are up to 3 times better than with classical ADCs.

the event every time a single block was badly fitted. This can decrease the detection efficiency by up to 10% depending on the calorimeter region. Keeping all blocks after at most a 2-pulse fit is the optimal solution, as resolutions depend on all blocks in the cluster and a bad fit in only one of them barely worsens the resolution of the event.

3.3.4 Real noise study

During the experiment, accidental events were recorded during dedicated runs. In order to do that, the acquisition was triggered by a clock and all electronic channels were recorded. A similar study to the one described above was performed in order to calculate precise values of efficiencies for a given set of waveform analysis parameters and the real experiment background conditions.

The efficiency was computed as a function of the energy of the simulated event and as

a function of the polar angle θ between the beamline and the event impact point in the calorimeter. Noise widens the energy resolution distribution, and the efficiency depends on the cut we make on this distribution, as shown in Fig. 3.6. A cut on the missing mass distribution will be made on the data, which would correspond to a cut on the energy resolution distribution. Fig. 3.6 shows the high efficiency of the calorimeter, as mentioned before. For energies $2.5 < E < 3\,\text{GeV}$, which is the lowest energy of DVCS photons in the kinematic setting 3 (highest background rates), the efficiency is 98% for $6^\circ < \theta < 11^\circ$ and more than 99% for $15^\circ < \theta < 18^\circ$, for a cut on the energy distribution of $\pm 150\,\text{MeV}$. That would imply a cut on the squared missing mass distribution of approximately $\pm 0.1\,\text{GeV}^2$ around the proton mass squared.

A further study was made with real data to test waveform analysis parameters. As it will be shown later, the detection of π^0 when both photons hit the calorimeter is very clean, as requiring two photons in time highly reduces the contamination from accidental

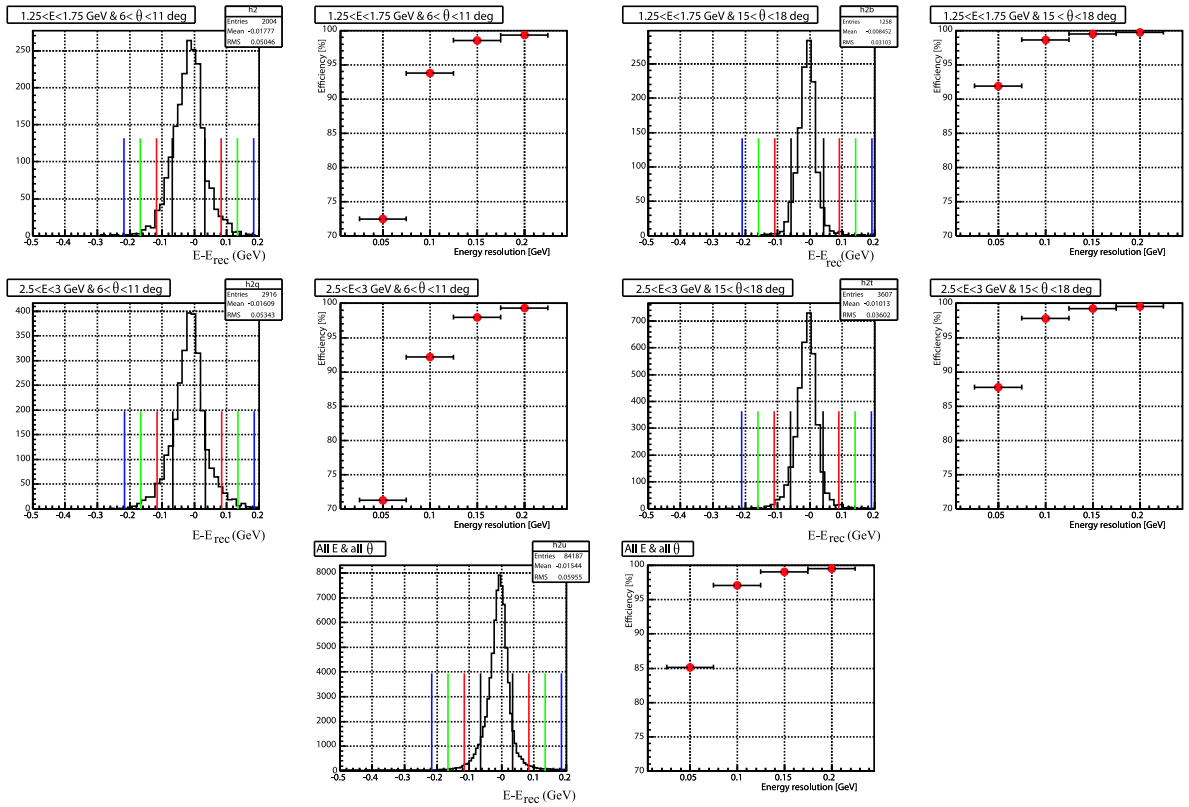

Figure 3.6: Energy resolution and efficiency for low and high energy events and for small and large θ (polar angle with respect to the beamline). The efficiency is plotted as a function of the cut on the energy difference (generated minus reconstructed), shown by different colors lines: $\pm 50\,\text{MeV}$ (black), $\pm 100\,\text{MeV}$ (red), $\pm 150\,\text{MeV}$ (green) and $\pm 200\,\text{MeV}$ (blue). The last plots show the integrated distribution and efficiency for all energies and over the whole calorimeter.

events. Waveform analysis parameters, particularly the χ^2 thresholds, were changed in order to check the stability of the number of reconstructed π^0. We obtained stable results for values of χ^2 thresholds similar to the values found with the Monte Carlo simulation and the real data study mentioned before.

3.4 Proton array

3.4.1 Waveform analysis optimization

The recoil DVCS proton will only hit one proton array block in most cases, and will deposit much less energy than a photon in the calorimeter. The analysis of this detector is therefore very different from the calorimeter analysis and consequently the parameters of the waveform algorithm will also be different.

Efficiency is close to 100% in the calorimeter, as DVCS photons are very energetic (>1.5 GeV). A high energy threshold of around 1 GeV could be set. In addition to this, around 10 calorimeter blocks are hit in every event. However, proton efficiency is the main issue in the proton array analysis. The energy loss by a proton in the detector can go down to zero. The optimal energy threshold is hence the lowest possible value compatible with an accurate computation of the acceptance and efficiency.

In order to optimize waveform analysis, we studied the efficiency as a function of the different parameters.

3.4.2 Efficiency calculation

To measure the inefficiency of the waveform analysis algorithm due to noise we proceeded as follows. Using real data, we selected events where no calorimeter cluster was found in time with the electron in the coincidence window of [-3 ns,3 ns]. For these events, we considered that the ARS signals recorded in the proton array blocks were mostly accidental events (noise). On top of those events, we added a simulated pulse of a given energy E_s at time $t = 0$. We then applied the waveform analysis algorithm and we counted the event as detected if we found one pulse within [-2 ns,2 ns] (this cut should be the same as for the data, for the efficiency calculation to be meaningful).

The efficiency was studied for different parameters of the waveform analysis algorithm and as a function of the simulated energy E_s and the proton array block number. The background rates are very different depending on the block distance to the beamline, as in the case of the calorimeter.

3.4.2.1 Analysis window width and constant level fit

For wide analysis windows, an accidental pulse bigger than the true one arriving in the window can prevent the true one from being fit. We tested the efficiency for 2 different analysis windows, shown in Fig. 3.7 together with the reference shape of a typical block (number 16).

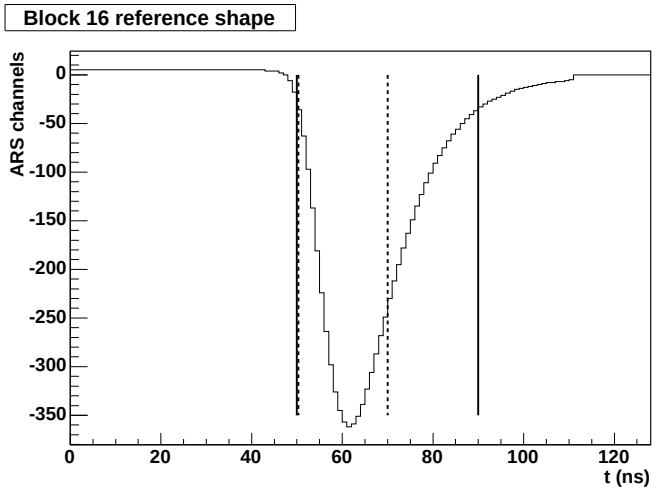

Figure 3.7: Reference pulse of block 16 and the two analysis windows used: [50,70] and [50,90].

Fig. 3.8 shows the efficiency as a function of χ_1^2, the threshold to fit 2 pulses, for these two different analysis windows. For large values of χ_1^2, only 1 pulse is fit all the time. As χ_1^2 decreases, we start fitting a second pulse in the noisiest events and the efficiency increases. Very small values of χ_1^2 correspond to fitting 2-pulses most of the time. Fig. 3.8 shows also the number of accidental events found in the same conditions: the analysis of the event is done without adding the simulated pulse ($E_s = 0$). As it can be seen for very small values of χ_1^2, the number of false events found also increases. A value of χ_1^2 of around 10 MeV seems reasonable to increase the detection efficiency for real pulses without artificially reconstructing too many accidental events.

Fig. 3.8 also shows the effect of fixing the constant level $b = 0$ when fitting. Indeed, this increases the efficiency. Leaving b free can cause bad fits like the one shown in Fig. 3.9, where a large constant level is fit with a "negative energy" pulse. Fixing b to zero slightly worsens the energy resolution of the fit, as shown in Fig. 3.10, but since efficiency is the main concern for the proton detection, we will fix b to zero for the analysis.

3.4.2.2 Energy and block position dependence

The efficiency obtained for the set of waveform parameters chosen will be used to correct the results of the experiment. This efficiency is very dependent on the block position and the energy deposition in the block. Fig. 3.11 shows for three different blocks, the efficiency obtained with b fixed to zero and an analysis window [50,70].

For an energy threshold of 20 MeV the efficiency is higher than 80% in most of the detector. Only blocks very close to the beam, such as block number 2 (at 22°) have lower efficiencies.

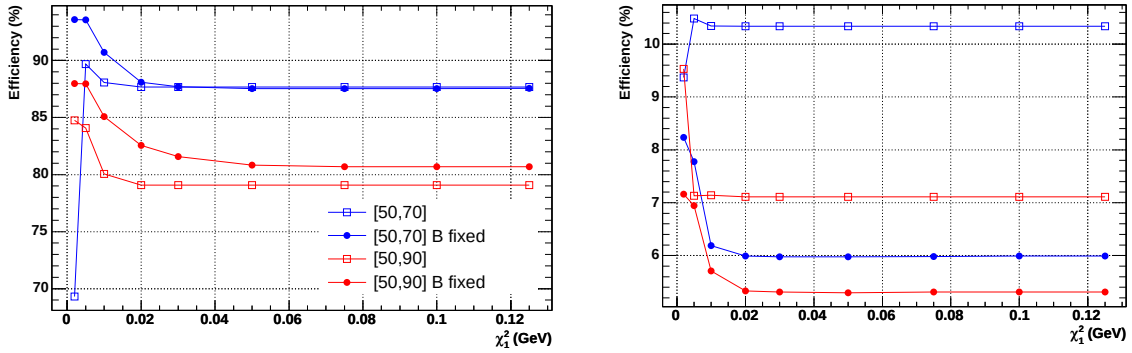

Figure 3.8: Efficiency as a function of χ^2_1 for different analysis windows and with constant level b free and fixed to zero. The reconstruction of accidentals is shown in the right for the same conditions. This plot is for proton array block number 16 and energy $E_s = 25\,\mathrm{MeV}$.

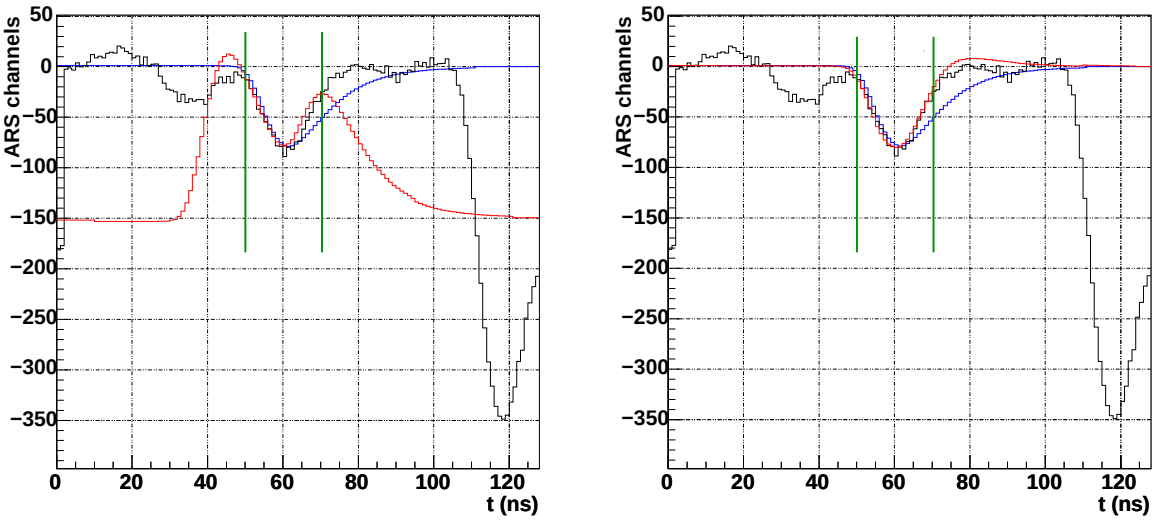

Figure 3.9: Event showing a bad 2-pulse fit for block 16 when the constant level b is free (left) and the result when $b = 0$ (right). The blue signal is the simulated pulse added ($E_s = 25\,\mathrm{MeV}$), the black one is the total signal (simulated pulse and noise) and the red one is the fit. The analysis window is [50,70] ns (shown by vertical lines).

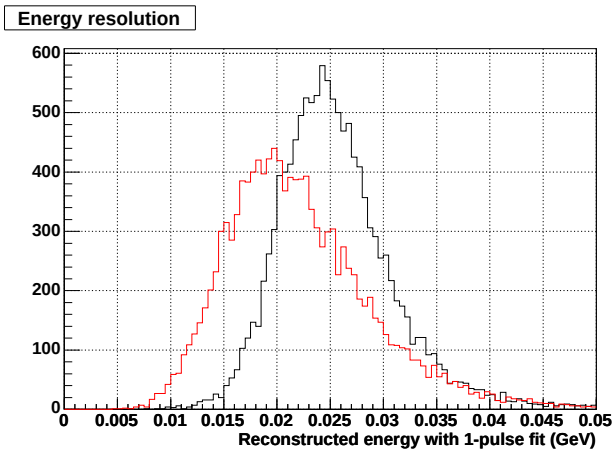

Figure 3.10: Energy distribution of events (arrival time of the fit $-2 < t < 2\,\mathrm{ns}$) for free b (black) and $b = 0$ (red), for an energy $E_s = 25\,\mathrm{MeV}$. The overall shift of the red distribution is due to the fact that the calibration coefficient used for this study was obtained for free b. The FWHM of the distribution for fixed $b = 0$ is 13.6 MeV whereas it is only 9.9 MeV for free b.

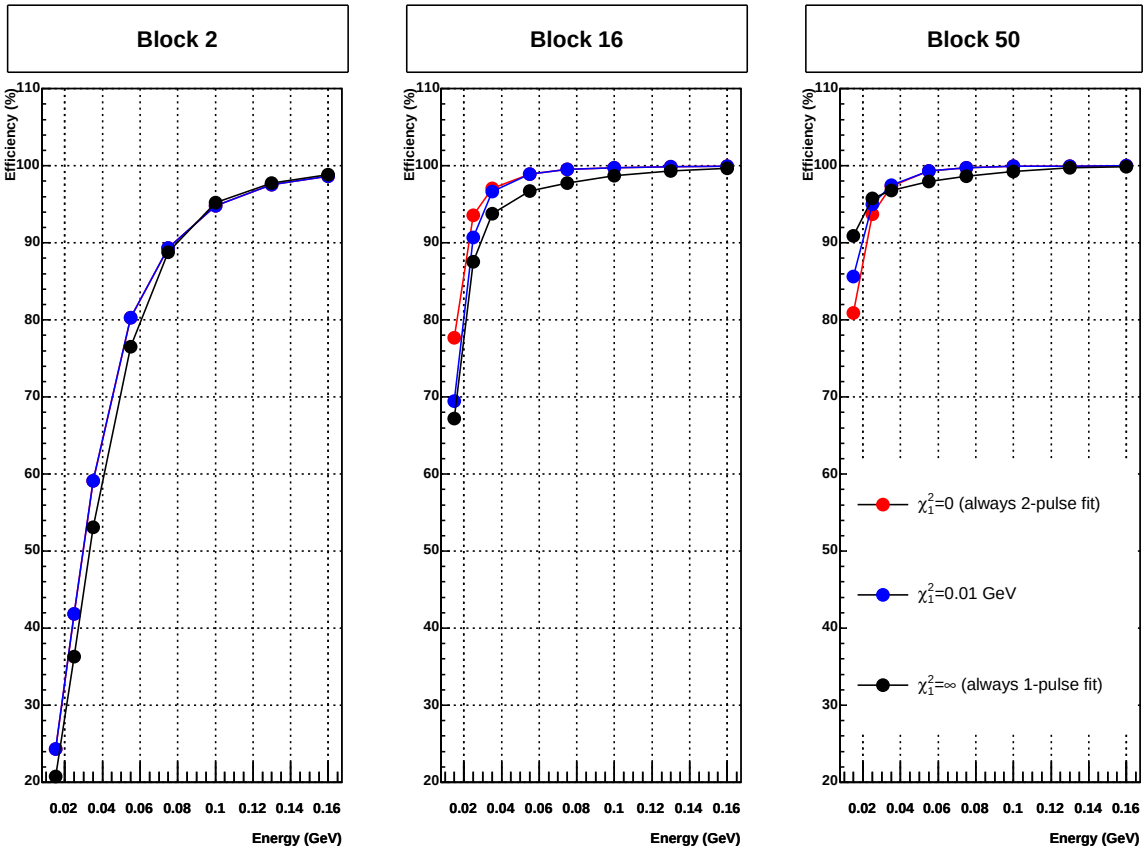

Figure 3.11: Efficiency as a function of the energy deposition E_s for three different blocks: block 2 (22° from the beamline), block 16 (35°) and block 50 (51°). For block number 2, the red and the blue points coincide: $\chi_1^2 = 0.01\,\mathrm{GeV}$ means fitting always 2 pulses for this block.

Chapter 4

Detector calibration

This chapter describes how the HRS, the electromagnetic calorimeter and the proton detector were calibrated, and the results obtained.

4.1 HRS

The core of the HRS reconstruction is the transport matrix (cf. section 3.1). This optics matrix is, however, quite stable and for our precision requirements no special optics calibration was considered necessary. This would have required dedicated runs and a long optimization process. The transport matrix of a previous experiment with the same magnet configuration was used. However, two optimizations in the HRS analysis were made and are described in this section.

4.1.1 VDC t_0 optimization

As described in section 3.1, in order to compute the particle track through the VDC planes, TDC information is used together with the relationship between drift time and drift distance. This relationship has proven to be very stable and previous measurements can be trusted. It is common for all wire cells and assumes that zero drift time corresponds to a zero drift distance. It is therefore necessary to make sure that the TDC offsets of each wire are as close to zero as possible (after correction).

TDC offsets for each VDC wire were optimized using a single arm HRS run on LH2 (200k events). Wires in each VDC plane were grouped together in bunches of 16 in order to increase the statistics of each TDC spectrum. These bunches are physically grouped together in the same TDC module. Each TDC spectrum was then smoothed and differentiated. The maximum slope point was then adjusted to the same value close to zero.

Fig. 4.1 shows some typical TDC spectra before and after correction. After the t_0 optimization, the small TDC offset is corrected.

An equivalent run taken 5 weeks later was analyzed with the same database. Results of a similar quality were obtained, proving the stability of the correction during the

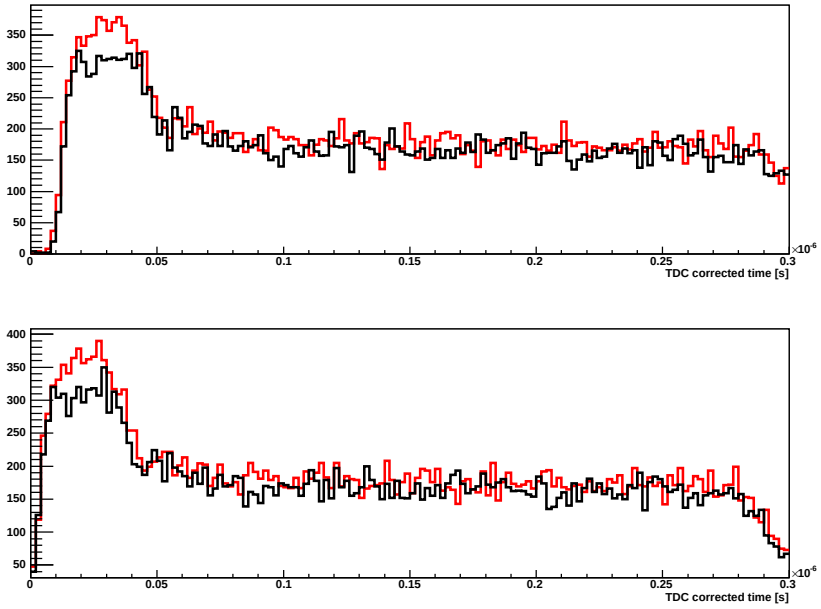

Figure 4.1: TDC corrected time for two different bunches of 16 wires of one VDC plane, before (top) and after (bottom) the offsets optimization. The TDC offset observed in the upper plot is corrected after the optimization.

experiment.

4.1.2 Beam position optimization

Beam Position Monitor (BPM) values are recorded on an event-by-event basis along with the rest of the data. However, the fluctuations of these values due to BPM noise are large, of the same order of magnitude that the real fluctuations of the beam (cf. Fig 4.2).

Real fluctuations of the beam position happen in a time scale greater than 1 s, much larger than the time between two recorded events. In order to reduce the artificial fluctuations of the beam position that are due to BPM noise, a running average of BPM values was studied. The test was made on a long (3 hour) multi-foil carbon target run. Beam positions were computed using a running average as:

$$\langle x\rangle_n = \frac{\alpha P_{n-1}\langle x\rangle_{n-1} + x_n}{\alpha P_{n-1} + 1}\,, \tag{4.1}$$

$$\langle y\rangle_n = \frac{\alpha P_{n-1}\langle y\rangle_{n-1} + y_n}{\alpha P_{n-1} + 1}\,, \tag{4.2}$$

with

$$P_{n+1} = \alpha P_n + 1\,. \tag{4.3}$$

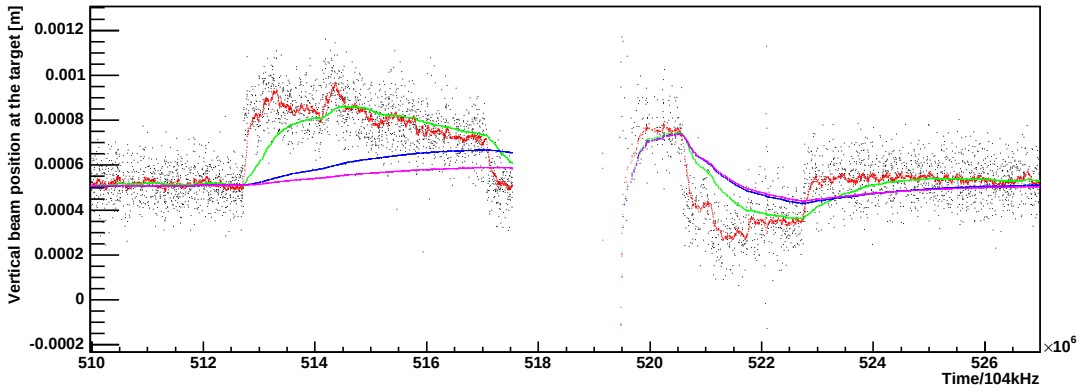

Figure 4.2: Raw vertical beam position at the target and running average for different values of α: 0.95 (pink), 0.995 (blue), 0.9995 (green) and 0.99995 (red). The full horizontal scale correspond to approximately 3 minutes. A beam trip is observed around the middle of the interval.

Recent events are more heavily weighted than older ones. The *dumping factor* α allows one to change this relative weight and several values of it were studied. Results are shown in Fig. 4.2.

After a beam trip, the running average was reset as the beam does not come back to the previous position. A beam trip was considered when the time between two consecutive events was greater than one second (the counting rate for this run was about 35 Hz).

A value of α between $\alpha = 0.99995$ and $\alpha = 0.9995$ seems appropriate to correctly account for beam fluctuations. The value $\alpha = 0.99995$ was chosen for the HRS data analysis.

4.2 Electromagnetic calorimeter

This section describes the calibration and tests performed in the calorimeter before the beginning of the experiment using cosmic rays and the LED monitoring system. Both of these systems were used to balance each channel gain, and results obtained will be shown. The last subsection describes the results of the *absolute* calibration done at the beginning (and the end) of the experiment using elastic scattering.

4.2.1 Cosmic ray calibration

The minimum ionizing energy deposition of cosmic rays crossing our PbF_2 calorimeter crystals is about 35 MeV per block, corresponding to the emission of 35 Čerenkov photons on average (according to the Monte Carlo simulation). This energy deposition is sufficient

to cross-calibrate all calorimeter channels, which means adjusting the high voltage (HV) of each PMT to get the same signal amplitude for the same energy deposition.

The energy deposition of minimum ionizing particles depends only on the length of material they go through. A slight difficulty arises in the calibration procedure. The cosmics read-out of the calorimeter was triggered by two scintillator paddles placed on top of it. The solid angle of the paddles relative to each block is different, and so is the energy distribution in each calorimeter block. We can either correct for this solid angle difference with a Monte Carlo simulation of the energy loss distribution in each block, or only consider vertical cosmics, which loose approximately the same energy in all blocks. The second option was chosen for simplicity, even though long cosmics runs were necessary at every iteration (HV change) in order to accumulate enough statistics. For the typical threshold set in the paddles, we had an acquisition rate of 0.5 Hz, that is 180k events for a typical run of 10 h. The offline selection of vertical cosmics was made by requiring a sufficiently large energy deposition in the top and bottom blocks of the same calorimeter column. This cut left us typically with 300 events per calorimeter column and block, that is 2% of the total number of events.

Waveform analysis of cosmic ARS signals was not used. Indeed, the shape of the signal was significantly different from one event to another. Čerenkov photons are emitted around the incident (vertical) cosmic and so make many reflections in the crystal before reaching the PMT. Depending on the distance between the PMT and the point where the cosmic went through the block, the signal shape is significantly different. The cosmic flux being very small compared to the ARS window (128 ns), the chances of getting two cosmics per event is almost zero and integrating the whole ARS signal is sufficient for our purposes. However, in order to be less sensitive to pedestal fluctuations of ARS samples, the integration of the ARS signal was only made in a 60 ns time window.

Fig. 4.3 shows (in logarithmic vertical scale) the spectra obtained in each calorimeter block after the offline vertical cut. These spectra were fit by gaussians and the HV of each PMT adjusted in order to shift the mean of each block to a common value. Several iterations were necessary (Fig. 4.3 shows the results of the last one) for obtaining the 2.7% cross-calibration shown in Fig. 4.4. This level of cross-calibration is almost the best we can get. Indeed the voltage measurement accuracy of LeCroy HV card model 1461 used is 0.1% of the setting + 1.5 V, which makes about 2.2 V for a typical HV of 700 V. The relative gain variation is

$$G = \alpha V^{\beta} \qquad \Rightarrow \qquad \frac{\Delta G}{G} = \frac{\beta}{V}\Delta V \tag{4.4}$$

The typical value of β for the calorimeter PMTs is around $\beta = 7$, which makes 2.2% relative gain variation for $V = 700$ V.

The systematics of the cross-calibration might, however, be larger than this 2.7%. A completely different method based on the LED system was used and results are presented in section 4.2.2.

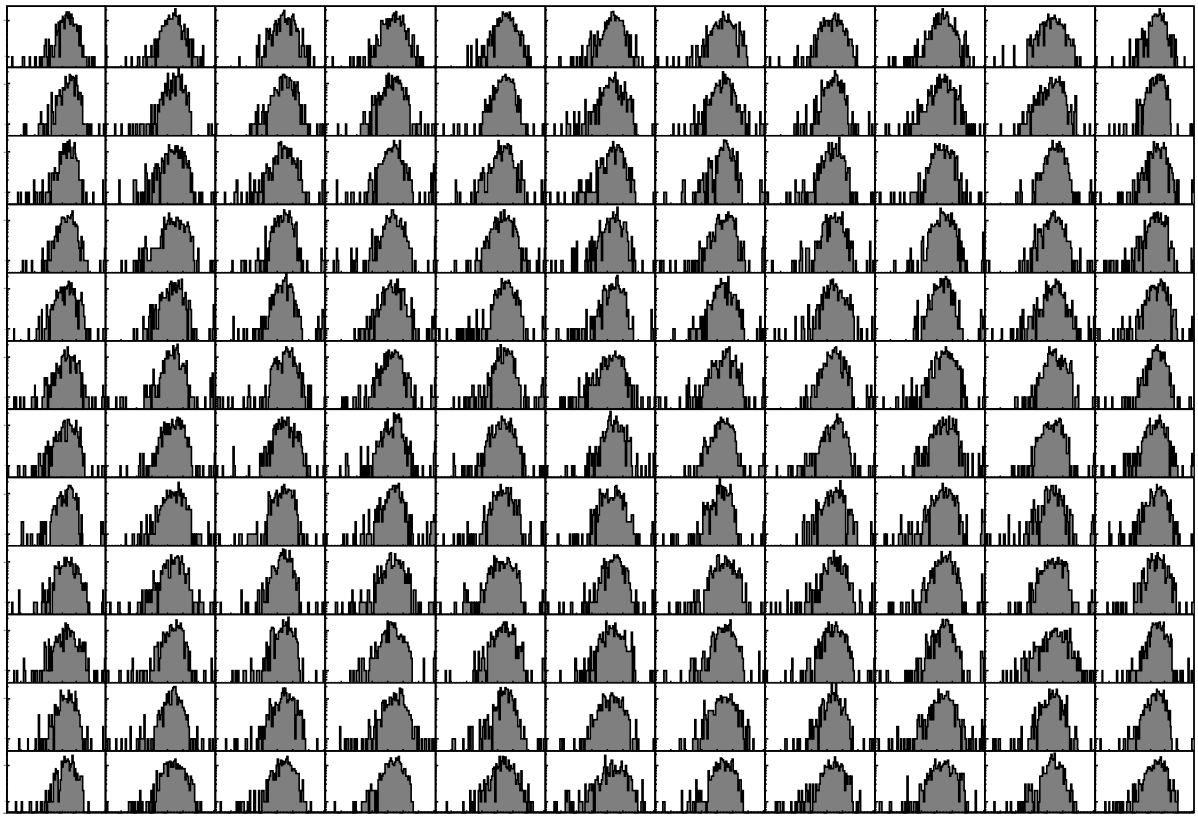

Figure 4.3: Energy spectra for vertical cosmic rays in each of the calorimeter crystals. All vertical and horizontal scales are the same in each plot. Vertical scale is logarithmic.

4.2.2 LED calibration

As mentioned in section 2.3.2, the electromagnetic calorimeter was equipped with a monitoring system based on three pulsed and one continuous LED. This system was very useful during the preparation of the experiment to test and characterize the calorimeter, and during the data taking to monitor the gain changes of each individual channel.

The advantage of this system consists of being able to illuminate each block with exactly the same signal: the same LED is moved in front of each block. This provides a very reliable relative calibration system that is able to detect very small relative gain variations. On the other hand, for the system to work efficiently, a very careful installation followed by many tests was necessary, as numerous systematic effects affect the measurement.

Firstly, the LEDs must be collimated very precisely so that almost all of the light they emit reaches the PMTs. Otherwise, the measurement is sensitive to the distance from the LED to the block, and so it is dependent on the angle between the calorimeter front face and the LED motion plane. Several collimators were constructed and tested in order to best collimate the LEDs light without obstructing too much of it. Sufficient light must reach the PMTs for the measurement to be reliable. Fig. 4.5 shows results with the

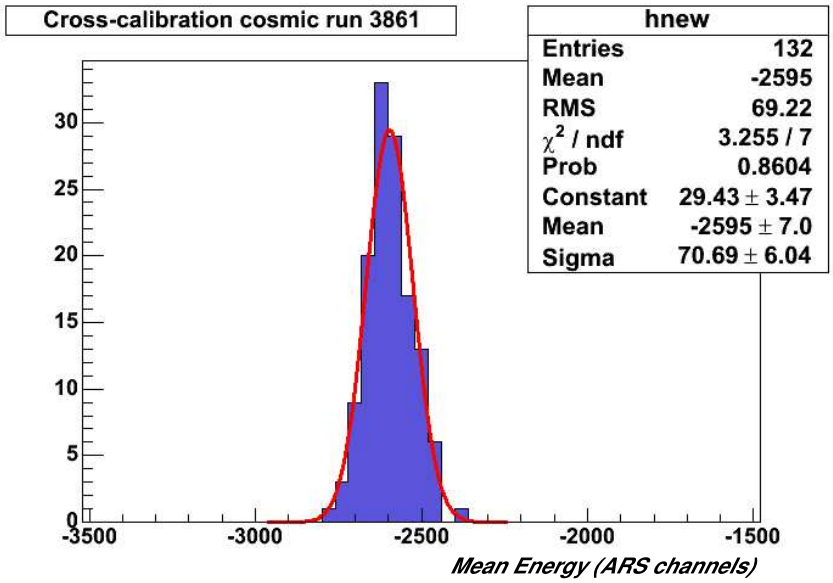

Figure 4.4: Cross-calibration with cosmic data. For each block, the mean of the energy distribution shown in Fig. 4.3 is histogrammed. The dispersion distribution width is 2.7% of its mean.

final collimator. It shows the signal amplitude difference for a 6-mm distance variation between the calorimeter and the LED's. The amplitude change is well below 1% per mm, which is less than the alignment error between the calorimeter front face and the LED's carrier.

Another important issue is the determination of the block centers, that is the positions where the LED carrier must be stopped to illuminate each block. To do that, a thorough scan was made of the blocks. Fig. 4.6 shows the scan of one of the blocks in 1 mm steps. The color scale shows the amplitude of the signal detected. The block center can thus be determined to an accuracy of better than 1 mm. This kind of measurement takes several hours depending on the step size and the number of events measured at each point. Therefore, it was not done for every block, but only for the four corner blocks of the calorimeter. Assuming equal block sizes, which is true to the precision of the block center determination, we inferred the rest of block centers. The measurement of the fourth block center is thus redundant and was used to check the procedure, as the block center measured and the one inferred from the other three measurement should be compatible within errors.

Several interesting tests of the calorimeter performance were possible during the experiment preparation thanks to the LED monitoring system. Fig. 4.7 shows PMT gain variations for one of the columns of the calorimeter as a function of the time after they are switched on (cold start). After a couple of hours the PMT gains are stable to better than 1%.

An important concern in the calorimeter performances was the possible PMT gain variation due to background noise. As mentioned in section 2.4, low energy background

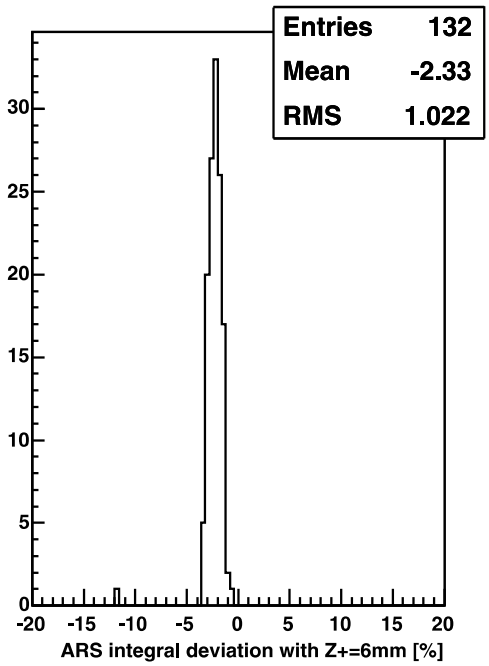

Figure 4.5: ARS integral deviation for a 6-mm distance variation between the calorimeter and the LEDs.

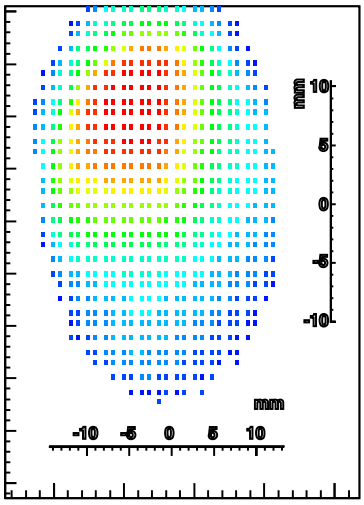

Figure 4.6: Block scan at 1 mm steps. The color scale represents the intensity (amplitude) of the signal.

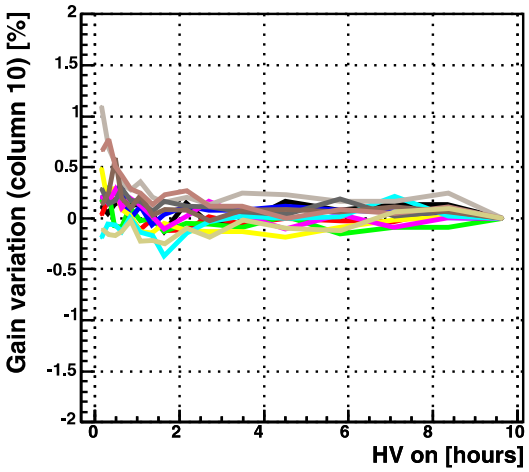

Figure 4.7: PMTs relative gain variation (with respect to the last value) as a function of the time after they are switched on for 12 different calorimeter blocks (first column).

noise, mainly coming from Møller electrons and low energy photons, can be very damaging to the calorimeter and can affect PMT gain and lifetime. A continuous LED was added to the carrier to simulate this background, similar to a light leak. Fig. 4.8 shows the gain variation of each PMT for different anode currents. The gain variation is below 1% even for relative large anode currents (up to $20\,\mu$A). PMT anode current was continuously monitored during the experiment. As ARS filter the signal DC level, the PMT signal was amplified and split, and the DC current was measured by ADCs whose readings were available online during the whole experiment data taking.

As mentioned before, 3 pulsed LED were installed in the LED carrier. All combinations of LEDs could be switched on and off simultaneously in order to test the linearity of each electronic channel. Fig. 4.9 shows the deviation from linearity when two different combinations of LEDs were tested. It remains below 0.5% on average.

Finally, Fig. 4.10 shows the cross-calibration results. It shows the signal integral for all channels with the HV obtained by cross-calibrating with cosmics (see section 4.2.1). Results obtained with this independent method of cross-calibrating the calorimeter blocks are within 9%.

During the experiment, calorimeter gains were monitored on daily basis during a special LED calibration run, of around 20 min duration. Several blocks lost their gain more rapidly than others and the HV of some of them was increased according to the results of the LED runs. However, the precise values of the gain variations obtained from LEDs were not completely reliable. Indeed, radiation damage takes place primarily in the block surface, preventing LED light from reaching the PMT. Electromagnetic showers (and the emission of Čerenkov photons), however, begin a few centimeters from the calorimeter surface, and thus are less sensitive to radiation damage in the block's surface. Therefore, the LED monitoring system provided a qualitative evolution of calorimeter block calibration, but only the elastic runs, described in the next section, provided us with an absolute

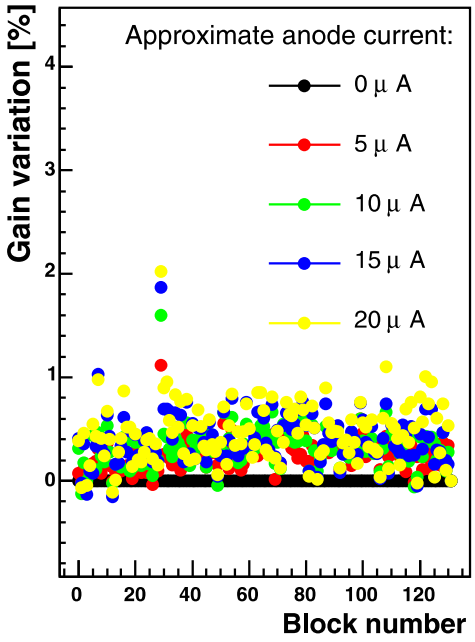

Figure 4.8: PMTs relative gain variation for different anode currents.

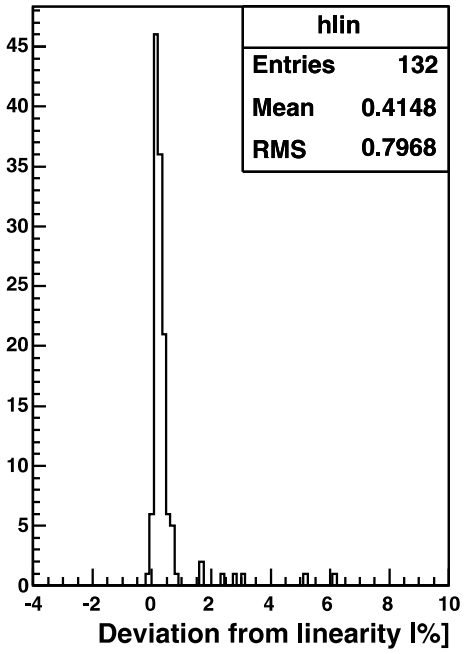

Figure 4.9: Deviation from linearity for two different linear combinations of LEDs.

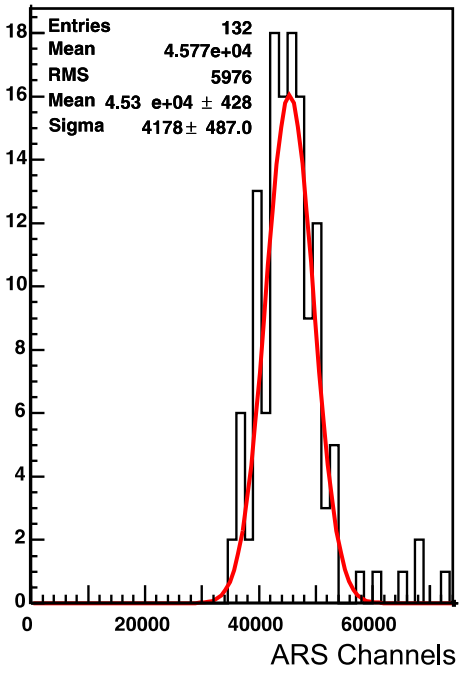

Figure 4.10: Calorimeter cross-calibration as measured by LEDs for the HV calculated with cosmics (cf. section 4.2.1).

and reliable calorimeter calibration.

4.2.3 Elastic calibration

In order to calibrate the *absolute* response of the electromagnetic calorimeter, we used a very constrained reaction : elastic scattering ($e\,p \rightarrow e'\,p'$). The recoil proton was detected in the HRS and the scattered electron response was measured in the calorimeter. Thanks to the high resolution of the HRS, the energy of the electron incident on the calorimeter could be determined very accurately.

At 1.1 m from the target, only a small portion of the calorimeter is illuminated by elastic electrons, due to the small acceptance of the HRS. Rather than moving the calorimeter vertically, it was moved back to a distance of 5.5 m. This distance is still not enough to cover it horizontally by elastic electrons, which meant that several horizontal settings of the HRS were necessary. The optimal number of setting (and their angles) were determined by Monte Carlo simulation. Even though two settings would have been enough to completely illuminate the whole calorimeter, three were actually made, as it was faster due to the elastic cross section dependence on the scattering angle.

4.2.3.1 Calibration procedure

Each electromagnetic shower leaves energy in several blocks (typically nine). The calibration procedure consists on a global fit of all calibration coefficients to best reproduce the data.

For an event j, considering the target proton at rest and neglecting the electron mass, conservation of energy yields the following energy E_j for the scattered electron:

$$E_j = E_b + m - E_j^p \tag{4.5}$$

where E_b is the beam energy, m the proton mass, and E_j^p is the recoil proton energy for that event, measured in the HRS.

If we call A_j^i the signal amplitude of calorimeter block i in event j, and C_i the block calibration coefficient, we can define a χ^2 as:

$$\chi^2 = \sum_{j=1}^{N} \left(E_j - \sum_i C_i \cdot A_j^i \right)^2 \tag{4.6}$$

where N is the total number of events and the sum over i runs for all blocks belonging to the reconstructed calorimeter cluster of event j.

The calibration coefficients are then those minimizing this χ^2:

$$\frac{\partial \chi^2}{\partial C_k} = -2C_k \sum_{j=1}^{N} (E_j - \sum_n C_i \cdot A_j^i) A_j^k = 0 \qquad \forall k = 0, 1 \ldots 131 \,. \tag{4.7}$$

This yields the following linear set of equations:

$$\sum_i \left[\sum_{j=1}^{N} A_j^k A_j^i \right] C_i = \sum_{j=1}^{N} E_j A_j^k \qquad \forall k = 0, 1 \ldots 131 \,. \tag{4.8}$$

Calibration coefficients can be obtained by inverting the 132×132 matrix $M_{ik} = \sum_{j=1}^{N} A_j^i A_j^k$.

4.2.3.2 Implementation

First of all, a cut on HRS variables was made to select good elastic events. Fig. 4.11 shows the reconstructed momentum versus the scattering angle ϕ_{tg} for each elastic setting, together with the corresponding impact position on the calorimeter. The cut applied to each setting is shown in red in the left plot.

A careful waveform analysis of every calorimeter event was made. Only events where all blocks were fit with good quality were included in the analysis. A timing cut was also applied to select calorimeter events in coincidence with the HRS.

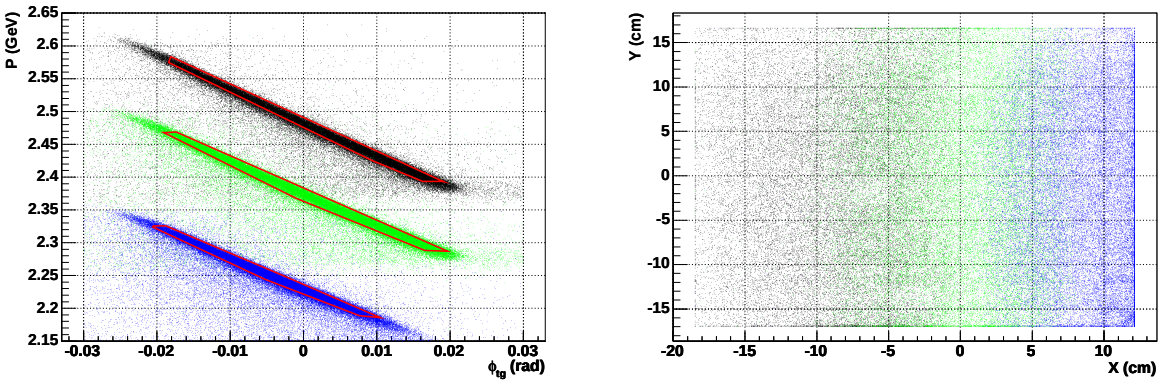

Figure 4.11: Proton momentum versus the scattering angle for each elastic setting (left). Cuts applied to select elastic events are shown in red. The corresponding impact point on the calorimeter is shown in the right plot.

4.2.3.3 Calibration results

Fig. 4.12 shows the distribution of measured energy minus predicted energy (from the HRS proton detection). Two successful elastic calibrations were made, one a few weeks after the experiment started and another one a few weeks after the experiment finished. Calibration coefficients changed considerably for some blocks (as shown in Fig. 4.13). Fig. 4.12 shows the results of both calibrations. Also, the results of the second calibration when the coefficients of the first calibration were used are plotted in Fig. 4.12. The width of the distributions for both calibrations are almost the same. This means that the quality of the calorimeter detection is still good after almost 3 months of data taking. The final resolution is 2.4% at 4.2 GeV (average energy of electrons).

However, in order to keep a good energy resolution all along the experiment, an interpolation of calibration coefficients between these two calibrations was necessary, together with an extrapolation both before and after them. This was done based on the radiation dose accumulated by each block. This dose is proportional to the beam current and depends on the block polar angle with respect to the beam line and also on the target type (LH_2 or LD_2). An estimation of relative dose accumulation for each block was made using the DC current monitoring for each crystal [55].

Fig. 4.14 shows the position resolution obtained in each calibration. However, at 5.5 m the position resolution is limited by multiple scattering (in the target, scattering chamber and in the air between the scattering chamber and the calorimeter). An elastic run at the nominal distance of 1.1 m was made to estimate the position resolution. As can be seen in Fig. 4.14, the angular resolution is almost the same at 1.1 m and 5.5 m and not 5 times better, which would be the case if multiple scattering was negligible. The global shift of the horizontal resolution at 1.1 m appearing in Fig. 4.14 is due to the fact that the calorimeter position was not surveyed at 1.1 m at the elastic scattering angle (at 1.1 m, only the DVCS angular settings were surveyed). The results of the calorimeter

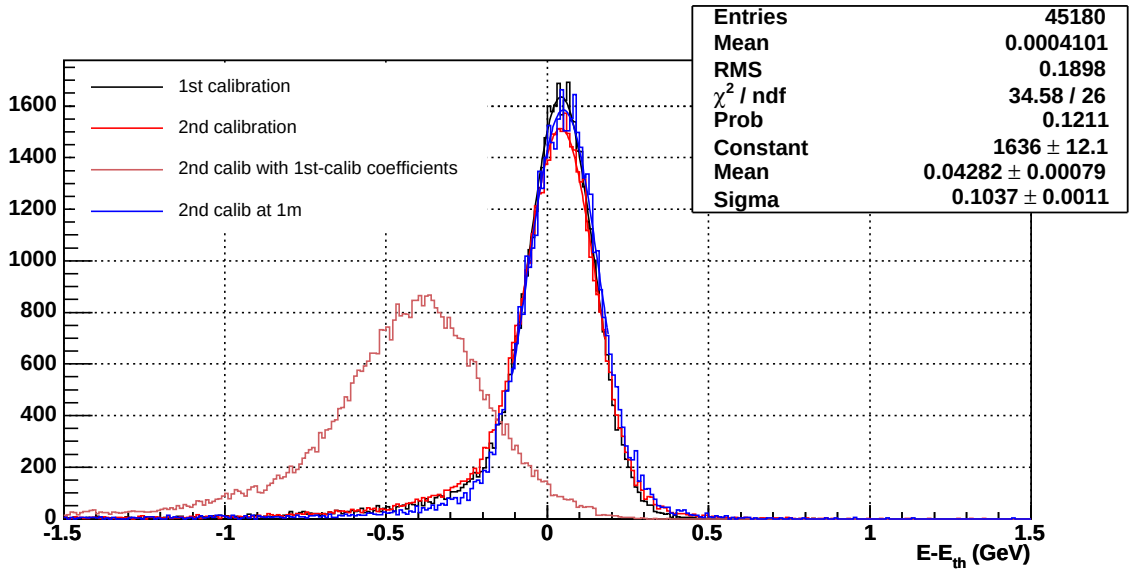

Figure 4.12: Energy resolution obtained in both elastic calibration: 2.4%, the average energy of the incident electron being 4.2 GeV. The results of the second calibration when first calibration coefficients are used are also plotted to show the necessity of a careful monitoring of the coefficients in between these two calibration points.

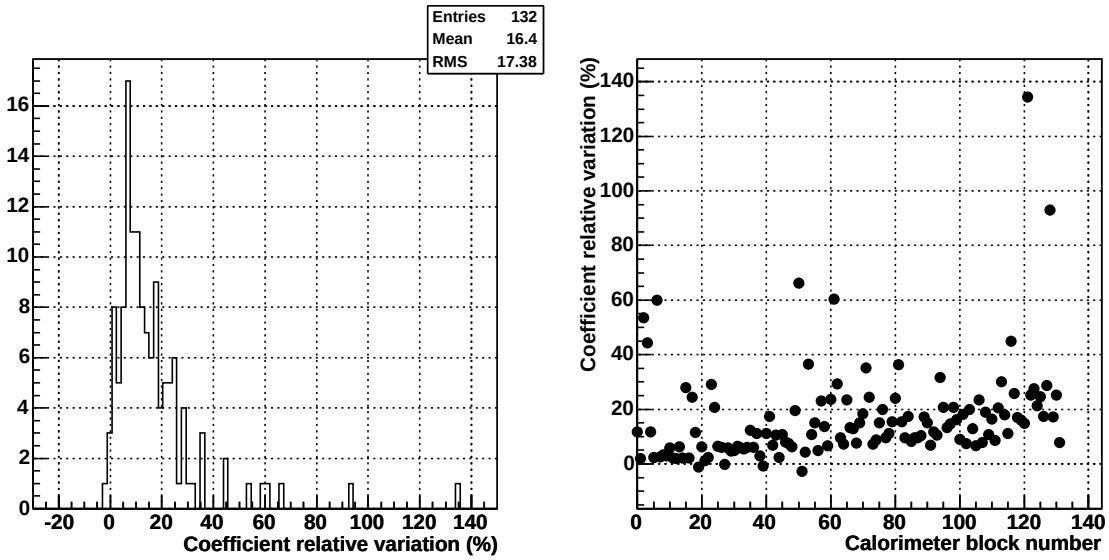

Figure 4.13: Relative variation of the calorimeter calibration coefficients between two elastic calibration. Their values are histogrammed (left) and plotted as a function of the block number (right). Larger block numbers correspond to blocks closer to the beamline. These blocks have accumulated a larger radiation dose and their gain have decreased more than those of other blocks.

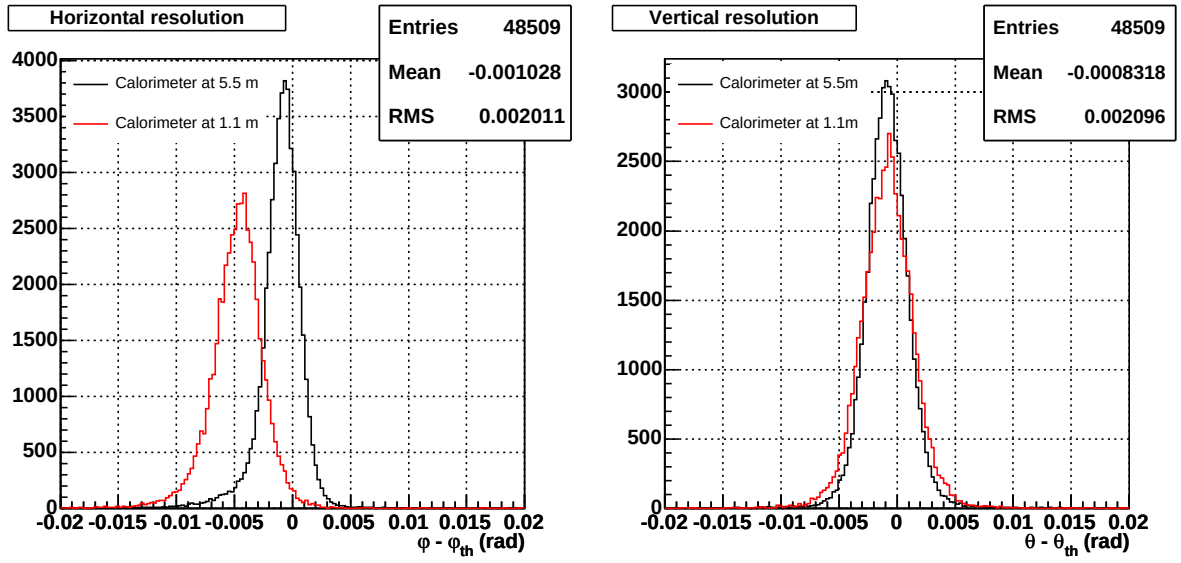

Figure 4.14: Position resolution obtained in the elastic calibrations. An elastic run at 1.1 m was also made and the results are plotted together. The shift in the horizontal resolution at 1.1 m is due to the fact that this calorimeter position was not surveyed.

position survey at 5.5 m were used to tune calorimeter analysis parameters, as mentioned in section 3.3.1.

4.3 Proton array

The vertical acceptance of the HRS is too small to illuminate the proton array by elastic events. The proton detector calibration was done in a completely different way. A careful selection of DVCS events was made by means of very tight cuts. For these events, the block hit by the recoil DVCS proton can be predicted from the HRS and calorimeter information, together with its energy deposition. By performing a linear fit to the measured amplitude versus the predicted energy deposition for these events, a calibration coefficient for each proton detector block can be obtained. Fig. 4.15 shows the result when the calibration coefficients obtained are applied.

DVCS events do not cover the proton detector uniformly. Different proton array blocks are preferentially hit in each kinematic setting. In the large Q^2 setting, the outer blocks are mostly hit, whereas it is the case of the inner blocks for low Q^2. Therefore, the calibration procedure was done for each kinematic setting in order to have enough statistics in each block to calculate its calibration coefficient.

An accurate energy calibration of the proton detector is not necessary. Indeed, only the time information (obtained from waveform analysis of the ARS signal) will be used to decide if there is an event in the predicted proton array block. The energy information will only be used to set a threshold in order to compute the experiment acceptance.

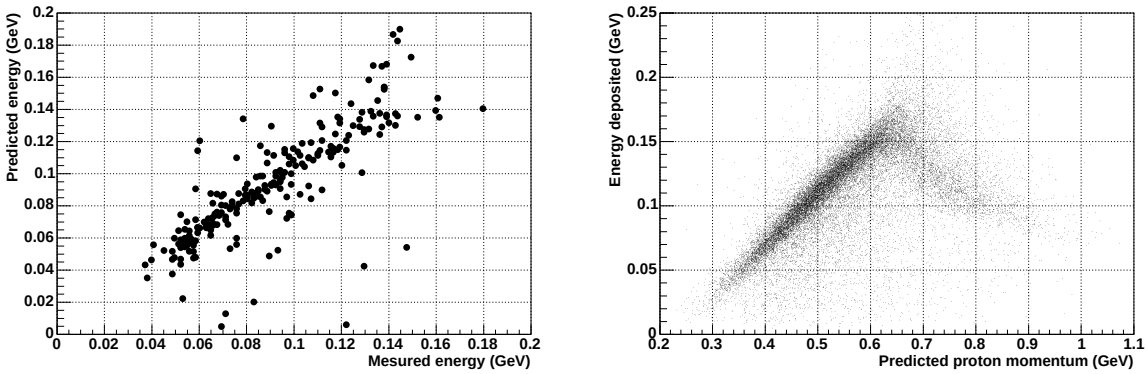

Figure 4.15: Proton array calibration: measured energy versus predicted energy for block number 53 (left) and energy measured versus predicted proton momentum for all blocks (right). Calibration coefficient are already applied in these plots.

Chapter 5

Monte Carlo simulation

A Monte Carlo simulation of the DVCS setup will be used to compute the experiment acceptance. We briefly describe in this chapter its main characteristics. Special attention will be payed to the event generator, used as input to the GEANT 3.21 [56] simulation of detectors. It is within the event generator that the real radiative corrections have been implemented in order to convolute their effects with detector resolutions. For clarity, I will start by describing these radiative corrections and introducing the expressions used later in the event generator. Some reference will be made to virtual radiative corrections. These are not treated in the simulation, but should be applied later as a global correction to the data. Results presented in chapter 6 are not yet corrected for *virtual* radiative corrections, but real radiative corrections are included in the calculation of the acceptance.

5.1 Global simulation strategy

Three different detectors are used in the DVCS experiment: the Hall A HRS, an electromagnetic calorimeter, and a plastic scintillator array.

The Hall A HRS is already well characterized. A VCS experiment successfully used the Hall A Spectrometers at a lower energy [57], where absolute cross sections were calculated. Its acceptance has been measured accurately and an acceptance function that parametrizes it, is available [58]. Also, the angular and momentum resolutions have been measured. This detector has not been fully simulated. Only standard resolutions and acceptances have been applied to it.

On the other hand, the new DVCS detectors, the electromagnetic calorimeter and the proton array, have been simulated in detail.

The simulation is implemented as follows:

- Firstly, the event at the vertex of interaction is generated following the kinematics of the DVCS reaction, and sampling the variables Q^2, x_B, t, φ and φ_e uniformly (φ_e is the scattered electron azimuthal angle). The initial electron energy takes into account real radiative corrections as explained below.

- The scattered electron is simulated up to the entrance window of the HRS in order to take into account external radiative corrections after the vertex of interaction, as well as multiple scattering. The components of the electron momentum at the entrance window of the HRS are later smeared by the nominal HRS resolutions. No magnetic transport or tracking in the HRS VDCs was made.

- The emitted DVCS photon and recoil proton are simulated fully. Multiple scattering in the air between the scattering chamber and the detectors is taken into account.

- Once particles arrive at the detectors, all main electromagnetic and hadronic processes are simulated using GEANT 3.21 cross section libraries. The energy loss in each detector block is written in the output file for each event.

- The same event structure as for real data is filled from the GEANT output file, so that exactly the same analysis can be carried out for both real and Monte Carlo data. Additionally, all variables at the vertex of the interaction are written in the output file.

I describe these steps in some more detail in the following sections.

5.2 QED Radiative corrections

Radiative corrections provide an important contribution to the $ep \to ep\gamma$ reaction. At low Q^2, the contribution is of the order of 20% to the total cross section (see MAMI results at $Q^2 = 0.33$ GeV^2 [59]). The importance of a very good understanding of the radiative corrections is indispensable if one wants to extract nucleon structure information from the $ep \to ep\gamma$ reaction. This is especially true in those kinematical situations where the Bethe-Heitler process is not negligible. The calculation of these QED radiative corrections to the $ep \to ep\gamma$ reaction to first order in $\alpha \simeq 1/137$ has been treated in great detail by Vanderhaeghen *et al.* [60].

Radiative corrections were first calculated by Schwinger for potential scattering [61]. Tsai [62] extended the calculation of the radiative corrections to electron-proton scattering. References [63, 64] review the long history of the field and are widely used in the interpretation of many electron scattering experiments. However, the $ep \to ep\gamma$ reaction is particular in comparison with other electron scattering reactions because the photon can be emitted from both the proton side (this is the VCS process which contains the nucleon structure information of interest) or can be emitted from one of the electrons (which is the parasitic Bethe-Heitler process). The radiative corrections to the Bethe-Heitler process are formally different from those in the case of electron scattering.

The radiative corrections to the leptonic side (where the photon is emitted along one of the electron lines) are dominant. The radiative corrections from the proton side are suppressed compared with those from the electron, due to the much larger mass of the proton.

We want to measure the cross section $\sigma_{\rm th}$ for the $ep \to ep\gamma$ reaction. It cannot be directly measured in an experiment, since in reality the pure $ep \to ep\gamma$ process is accompanied by additional photons, either real or virtual. These radiative effects give rise to a measured cross section $\sigma_{\rm exp}$ which must be corrected in order to obtain the desired cross section $\sigma_{\rm th}$:

$$\sigma_{\rm exp} = (1 + \delta_{\rm tot})\sigma_{\rm th} \, . \tag{5.1}$$

The above equation represents the first order radiative corrections to the cross section. The quantity $\delta_{\rm tot}$ is negative and contains several contributions:

$$\delta_{\rm tot} = \delta_{\rm vac} + \delta_{\rm vertex} + \delta_{\rm R} \, , \tag{5.2}$$

where $\delta_{\rm vac}$ is a correction for vacuum polarization diagrams, $\delta_{\rm vertex}$ is the vertex correction and $\delta_{\rm R}$ is the correction for radiation of one additional photon. The first two terms are usually referred as *virtual* radiative corrections, whereas $\delta_{\rm R}$ is called the *real* radiative corrections.

The radiation of an additional photon generates a *radiative tail* in the missing mass. Experimentally, one needs take the radiative tail into account in the calculation of the solid angle or acceptance. The acceptance is usually computed in a Monte Carlo simulation of the experimental apparatus, where all the resolutions of all detectors are included. It is useful to generate the radiative tail in the same Monte Carlo simulation in order to fold radiative effects with detectors acceptances and resolutions and other effects such as multiple scattering, energy losses...

Virtual radiative corrections do not modify the kinematics of the reaction. Besides, they turn out to be nearly constant for the phase space of interest. As such, the corresponding corrections can be applied as constant correction factors to the measured data. In contrast to real corrections, virtual corrections have the same final state as the DVCS reaction and hence interfere with the DVCS amplitude. Therefore, even though the corrections are made to the leptonic part and are model-independent, one needs a model of the DVCS amplitude to compute the contribution of virtual corrections. Later, some iterations with the measured DVCS cross-section can be made. Virtual corrections to the DVCS experiment are under evaluation and are not yet applied to the data presented in chapter 6. However, real radiative corrections are taken into account in the calculation of the acceptance, as explained below.

5.3 Event generator

5.3.1 Generation of the initial electron energy

This section describes how the real radiative corrections were implemented in the DVCS generator. The procedure follow the recipe used in the MAMI experiment and described in detail in [65], based on the calculations in [60].

5.3.1.1 External corrections before the vertex

There is an additional source of real radiative corrections different from the one described above. An electron passing through a slice of material produces photons due to bremsstrahlung. The energy loss of the electron, ΔE, is equal to the sum of the energies of all produced photons. The energy loss for an electron passing through a material taking into account multiple photon emission for $t < 0.05$ is given to very good approximation by [66]

$$I_{\rm ext}(E_0, \Delta E, t) = \frac{bt}{\Gamma(1+bt)} \left(\frac{\Delta E}{E_0}\right)^{bt} \left[\frac{1}{\Delta E}\left(1 - \frac{\Delta E}{E_0} + \frac{3}{4}\left(\frac{\Delta E}{E_0}\right)^2\right)\right]. \tag{5.3}$$

Here E_0 is the kinetic energy of the electron before bremsstrahlung, $b \simeq 4/3$ and t is the material thickness in units of its radiation length. For Monte Carlo purposes, an efficient way to generate a random energy loss ΔE according to this probability is given by [67]

$$E^{\rm ext} = E_0 R_{\rm Ext}^{1/bt}, \tag{5.4}$$

where and $R_{\rm Ext}$ is a uniform random variable on the interval $[0, 1]$. This generates an external radiation distribution

$$I_{\rm ext}(E_0, \Delta E, t) \;=\; \frac{bt}{\Delta E}\left(\frac{\Delta E}{E_0}\right)^{bt}, \tag{5.5}$$

which reproduces the dominant $1/\Delta E$ dependence of Eq. (5.3). This kind of radiation is known as *straggling* and we refer to it as *external* real radiation to distinguish it from the radiation of a photon at the $ep \to ep\gamma$ vertex of interaction, described before and called *internal* real radiation. Eq. (5.4) will be used in the event generator to create the initial electron energy. The vertex position will be randomly generated along the target length. The distance t is then computed and the electron energy sampled according to (5.4).

5.3.1.2 Internal real corrections

In the radiative correction to the BH where the soft photon couples to an on-shell lepton, as in Fig. 5.1 (a), the original BH amplitude factorizes [60]. The same happens in the case of the DVCS diagram, shown in Fig. 5.1 (c). In these two cases, the same correction as in elastic scattering can be applied. The resulting amplitude leads to logarithmic divergences when integrating over the phase space of the soft photon [60]. In contrast, the diagrams where the photon couples to an off-shell lepton line, as in Fig. 5.1 (b) are finite when the soft photon momentum $l \to 0$, and the corresponding phase space integral vanishes in the limit of soft photons. Therefore, we only need to care about the bremsstrahlung corrections where the BH and DVCS factorize and so we can apply the same corrections as in elastic scattering.

The internal real radiative corrections have been calculated using the equivalent radiator technique [63], which is based on the assumption that the internal radiation is

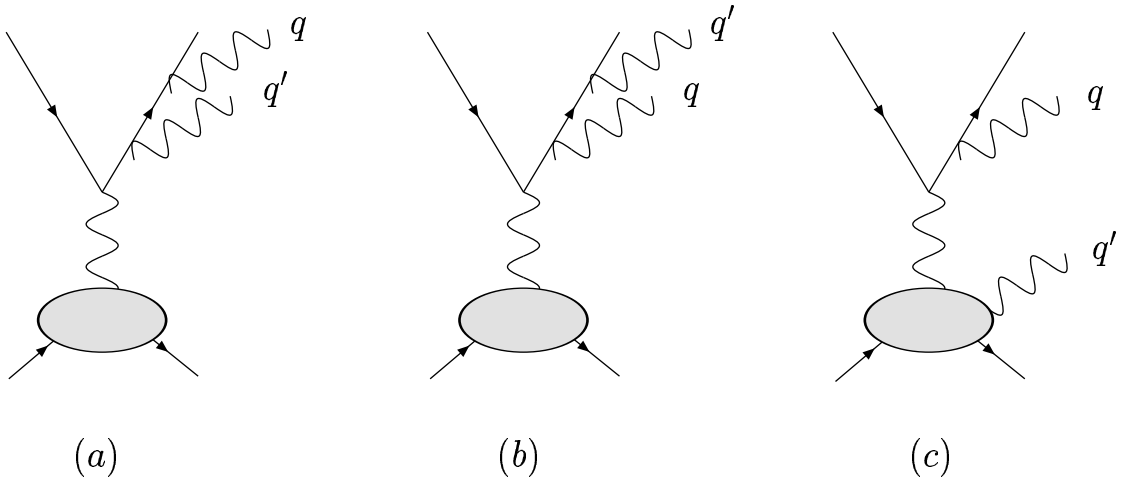

Figure 5.1: Different types of internal real corrections (emission of an additional soft photon q). The BH corrections are of two types: the soft photon is emitted along an external lepton line (a) or from an off-shell line, like in (b). The DVCS radiative internal real correction is shown in (c). Soft radiation along the proton lines are neglected due to its higher mass.

equivalent to placing one radiator before the scattering and another radiator of the same thickness after the scattering:

$$I_{\rm int}(E_0, E, \nu) = \frac{\nu}{\Delta E}\left(\frac{\Delta E}{E_0}\right)^{\nu}, \qquad \nu = \frac{\alpha}{\pi}\left[\ln\left(\frac{Q^2}{m_e^2}\right) - 1\right], \tag{5.6}$$

where ν plays the role of the equivalent radiator thickness (bt). We apply this correction twice. Once before the scattering:

$$E_1^{\rm int} = E^{\rm ext}(R_1^{\rm Int})^{2/\nu}, \tag{5.7}$$

where $R_{\rm Int}^1$ is another uniform deviate, and again after the scattering (see section 5.3.3).

5.3.2 Generation of the scattered electron kinematics

Due to the small acceptance of the Hall A spectrometer, generating events in the full phase space of the DVCS reaction is very inefficient. Only a very limited number would be detected in the experimental setup.

The event will be first generated within the horizontal plane ($\varphi_e = 0$), and will assumed a HRS squared acceptance in the horizontal angle ϕ_e and momentum p_e:

$$\phi_e^{\rm min} < \phi_e < \phi_e^{\rm max}, \tag{5.8}$$
$$p_e^{\rm min} < p_e < p_e^{\rm max}. \tag{5.9}$$

These acceptances $[\phi_e^{\min}, \phi_e^{\max}]$ and $[p_e^{\min}, p_e^{\max}]$ were chosen slightly larger than the real ones in order to be able to use the precise acceptance function later and compute accurately the solid angle (see chapter 6). However, these acceptances are still much smaller than the full phase space. An acceptance in p_e of 5.5% around the HRS central momentum and a 60 mrad acceptance in ϕ_e were used at the generation instead of the 4.5% and 28 mrad nominal ones. The p_e and ϕ_e ranges chosen imply the following ranges in the kinematic variables Q^2 and x_B:

$$(Q^2)^{\min} = 2p_e^{\min}E_1^{\rm int}(1-\cos\phi_e^{\min}) < \quad Q^2 \quad < 2p_e^{\max}E_1^{\rm int}(1-\cos\phi_e^{\max}) = (Q^2)^{\max}\,, \tag{5.10}$$

$$x_B^{\min} = \frac{p_e^{\min}E_1^{\rm int}(1-\cos\phi_e^{\min})}{M(E_1^{\rm int}-p_e^{\min})} < \quad x_B \quad < \frac{p_e^{\max}E_1^{\rm int}(1-\cos\phi_e^{\max})}{M(E_1^{\rm int}-p_e^{\max})} = x_B^{\max}\,, \tag{5.11}$$

where M is the proton mass. For a given value of the initial electron energy $E_1^{\rm int}$, obtained as described in the previous section, the electron kinematics of the event were defined by choosing Q^2 and x_B randomly and uniformly within the ranges of (5.10) and (5.11). A phase space factor $\Delta Q^2 \Delta x_B = [(Q^2)^{\max} - (Q^2)^{\min}]\cdot[x_B^{\max} - x_B^{\min}]$ will be associated with the event, which will account for the small phase space region where the event was generated.

Then, the scattered electron momentum p_e is computed from available energy before the interaction as

$$p_e = E' = E_1^{\rm int} - \frac{Q^2}{2Mx_B}\,, \tag{5.12}$$

where we neglect the electron mass so that $p_e = E'$.

In order to generate the electron scattering angle ϕ_e, the energy available at the vertex is also taken into account:

$$\cos\phi_e = 1 - \frac{Q^2}{2p_eE_1^{\rm int}}\,, \tag{5.13}$$

5.3.3 Internal post-radiation

Finally, the the second half of the equivalent radiator thickness is applied after the scattering:

$$E_2^{\rm int} = E'(R_2^{\rm Int})^{2/\nu}\,, \tag{5.14}$$

using a last random number $R_2^{\rm Int}$, uniformly distributed between [0,1]. The value $E_2^{\rm int}$ is the scattered electron energy as computed in the generator.

5.3.4 Hadronic reaction

The hadronic part of the reaction ($\gamma^*\ p \to \gamma\ p'$) is computed in the center-of-mass frame and then the particles are boosted to the laboratory frame. The variables t and φ are generated randomly. Because of the kinematic bound (1.62), t is chosen in the interval:

$$t \in [t_{\max}, t_{\min}(x_B, Q^2)]\,. \tag{5.15}$$

In principle, $t_{\max}$ also depends on the kinematics, but we chose a small enough absolute value that is does not matter. The variable φ is randomly chosen between [0,2π]. Each event receives an additional phase space weighting factor $|t_{\max} - t_{\min}| \cdot 2\pi$.

Finally all three particles: the scattered electron, the real photon and the recoil proton, are rotated around the beam axis, in order to simulate the vertical acceptance of the HRS. This rotation is slightly larger than the nominal vertical acceptance of the HRS in order to later be able to precisely simulate the HRS acceptance. A final phase space factor $\Delta\varphi_e$ is associated to the event.

The global phase space weight associated with the event is:

$$\Delta\Gamma \;=\; \Delta x_B \Delta Q^2 \Delta\varphi_e \Delta\varphi \Delta t(x_B, Q^2)\,, \tag{5.16}$$

which is basically constant for each event, except for the value of $t_{\min}$.

5.4 GEANT simulation of the experimental setup

Fig. 5.2 shows the main elements of the GEANT Monte Carlo simulation of the experimental setup. All geometrical offsets of the real experiment, measured during the survey of detectors, have been included in the final simulation geometry.

The electromagnetic shower in the calorimeter is fully simulated, following each particle down to an energy threshold of 100 keV. The emission of Čerenkov light and the tracking of all Čerenkov photons within the calorimeter blocks can also be made. However, the tracking of all the Čerenkov photons is very time consuming. It was made in order to estimate the light yield or number of Čerenkov photons emitted by GeV, which was found to be around 1000 per GeV. Later, for speed purposes only the energy losses in each calorimeter block were computed in the simulation. The energy deposited in each calorimeter block was later smeared to take into account the photostatistics due to the number of Čerenkov photons emitted. Thus, the energy loss $E_{\rm loss}$ in each of the calorimeter blocks was smeared by

$$\sigma = \frac{1}{\sqrt{1000\, E_{\rm loss}}}\,. \tag{5.17}$$

An additional smearing was applied to take into account the effect of background noise in the calorimeter resolution. Comparing the experimental energy and missing mass resolutions, a smearing of 5% in the calorimeter energy was applied in order to reproduce the experimental resolution widths. Comparison with data is presented in chapter 6 (section 6.5).

In the case of the proton detector, scintillating light was not simulated either. This option is not implemented in the standard GEANT package. Some other simulation codes exist to deal with a full simulation of scintillators, but results are never very accurate. Instead, only energy losses in the proton detector are simulated, down to the same energy threshold as in the case of the calorimeter, i.e. 100 keV. Scintillation quenching is simulated.

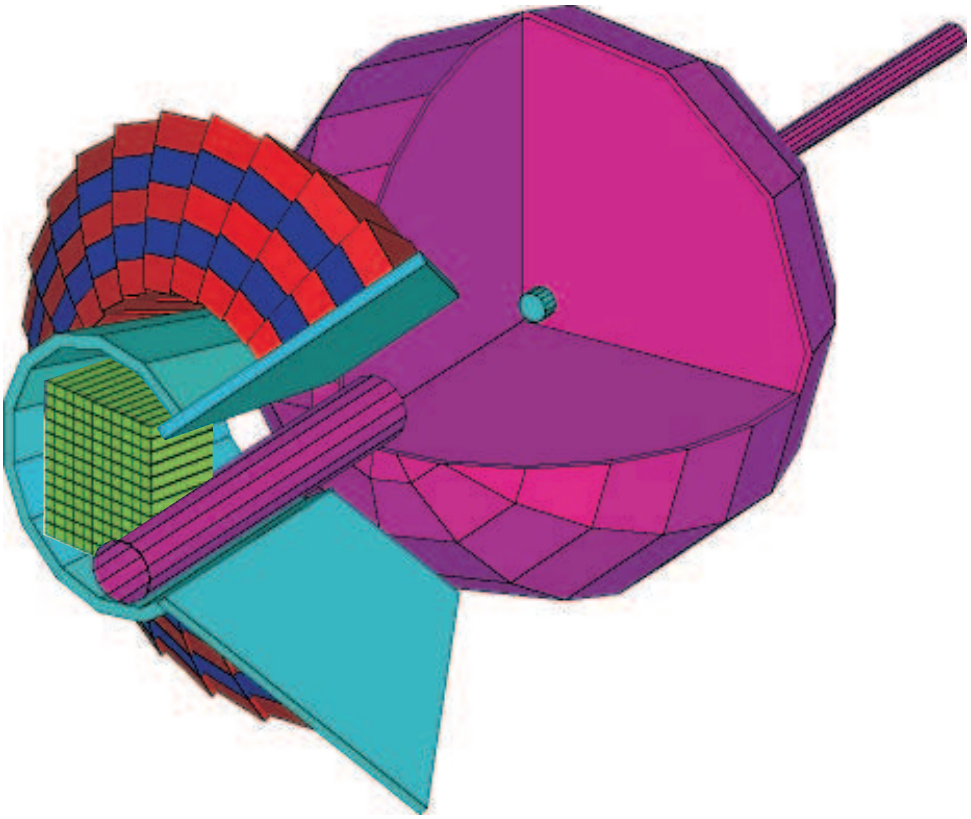

Figure 5.2: Main elements of the simulated experimental setup. This includes the scattering chamber, the electromagnetic calorimeter and the proton scintillator array. An aluminum plate in front of the calorimeter (not shown in the picture) and all other kind of materials in the experimental setup, such as target cell walls, are also simulated. All experimental offsets are included in the geometry.

Chapter 6

Data analysis

This chapter describes in detail the data analysis. After a general introduction to the data processing and global analysis, the criteria and selection cuts for each of the particles of the reaction final state are described. The missing mass distribution when only the scattered electron and the photon are detected will be presented later. The quality of this spectrum suggests that we can select exclusive DVCS events by making a tight cut on the missing mass. In a preliminary analysis, the proton detector will be used to evaluate the contamination from background and to check the acceptance and Monte Carlo simulation. Also, statistics are increased when using only the HRS and the calorimeter in the analysis. Finally, the general procedure to extract observables from the raw data is detailed. Preliminary results on the difference of cross sections with opposite beam helicities will be presented and discussed.

6.1 Raw data analysis

After almost 2 months of running, 2.4 TB of data were recorded for the DVCS experiment. Several analysis passes were done, with increasing reduction of the data volume. A sophisticated data structure was developed for the DVCS experiment based on the analysis tool ROOT [68]. At every pass, the event structure remained the same, with its different parts filled and erased as needed. For instance, the time and energy of a given calorimeter block is empty in the first analysis passes, and only its ARS information is included. When the ARS is analyzed, the time and energy of the block is filled and the ARS information is dropped and not written to file anymore.

I summarize here the main analysis passes on data:

- During the first pass, HRS data was decoded and analyzed. Calorimeter and proton detector data only was decoded and ARS information was filled into the data structure for later analysis. Some useless runs were discarded at this level. Data volume at this point was 1.6 TB.
- After carefully studying the calorimeter waveform analysis, a pass to analyze this detector was performed. ARS information from the calorimeter was dropped and

Pass	Input file size (MB)	Output file size (MB)	Memory (MB)	CPU time (h)
1	3500	2000	100	0.5
2	2000	1700	600	3.3
3	1700	280	550	9.5
4	280	85	100	0.6

Table 6.1: Typical computer resources required for the analysis of a single run during each of the analysis passes. Passes 2 and 3 are waveform analysis passes and need large CPU and memory resources. The total number of production runs of the experiment is 707. A full analysis of the data takes about one week with 50 to 100 jobs running simultaneously in a computer cluster.

only waveform analysis results were written to file. Total data volume after this pass was 1.2 TB.

- Next step was waveform analysis of the proton detector, after optimization of its parameters. After all ARS data was removed, the total size was reduced to 228 GB (0.23 TB).

- A final pass was made to turn data files in an *ntuple-like* format for easy analysis. Some further data reduction was made at this point also, with a total final size of 64 GB, with only 2.1 GB used by the HRS and calorimeter data.

Tab. 6.1 summarizes the computer resources needed in each of these passes. CPU time is real elapsed time using an average performance computer (Pentium IV).

Many parameters of the analysis change with time, such as calibration coefficients, waveform analysis parameters, time offsets, detectors positions... In order to take all these variations into account during the data processing, DVCS software was interfaced with a MySQL© relational database (DB), to keep track of all changes in a run-to-run basis. At the beginning of the analysis, all geometrical and calibration parameters are loaded from the DB, and updated when the run number changes.

6.2 Electron selection

6.2.1 Čerenkov detector

A Čerenkov detector was used for particle identification in the HRS. Its thickness is 1 m, with a path length of 80 cm, and it is filled with CO_2 at atmospheric pressure. The refraction index is $n = 1.00041$, which gives a threshold for Čerenkov light emittance of

- $p_{\min} = 17\,\mathrm{MeV/c}$ for electrons,

- $p_{\min} = 4.8\,\mathrm{GeV/c}$ for pions.

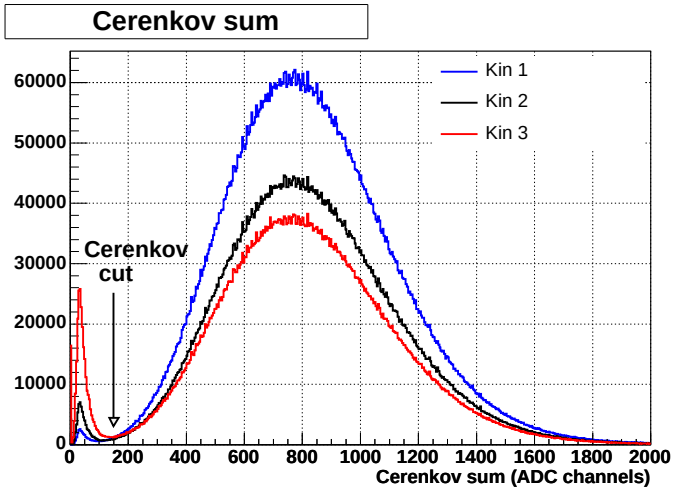

Figure 6.1: Distribution of the sum of all Čerenkov mirrors, for each kinematic setting. The cut applied to remove 1-photoelectron signal from data is also shown.

The electron identification efficiency of the Čerenkov detector is 99.8%. The Čerenkov includes 10 photomultiplier tubes and 10 mirrors. The number of photoelectrons is 7 on average, so that the distribution is a Poissonian distribution. Fig. 6.1 shows the distribution of the sum of all 10 mirrors (in ADC channels). The first peak of Fig. 6.1 corresponds to a 1-photoelectron signal, which can be produced by electronic noise. It is certainly not due to electrons, which produce the Poissonian distribution around 800 ADC channels shown in Fig. 6.1. We will cut 1-photoelectron events by applying a cut on the Čerenkov sum to avoid events whose value is smaller than 150 ADC channels.

Given the momentum acceptance of the HRS (±4.5% with a maximum central momentum of $P = 4\,\mathrm{GeV}$), pions should leave no signal in the Čerenkov counters. However, pions can produce a δ-ray by scattering on an atomic electron in the gas, which in turn generates an electron signal. The purity of the electron sample is not 100%. The measured value during the Čerenkov detector commissioning was 98.8%. The exact value for our experiment is under evaluation, using the total absorption shower detector (usually called the pion rejector). However, only a very small fraction of this 1.2% impurity of the electron sample will give a likely DVCS signal, i.e. a good missing mass when a photon is detected in coincidence in the DVCS calorimeter.

6.2.2 Number of tracks

As mentioned in section 3.1.1, the analysis of multiple tracks events in the HRS is very complex. We will discard multi-track events in our analysis and correct for the inefficiency of doing this. Fig. 6.2 shows the distribution of the number of HRS tracks n_t for each of the kinematic settings. The ratio of 1-track event to the total number of events is shown in Tab. 6.2. The number of multi-track events increases for small HRS angles, as the single counting rates are higher. We will multiply our results by the inverse of the ratios

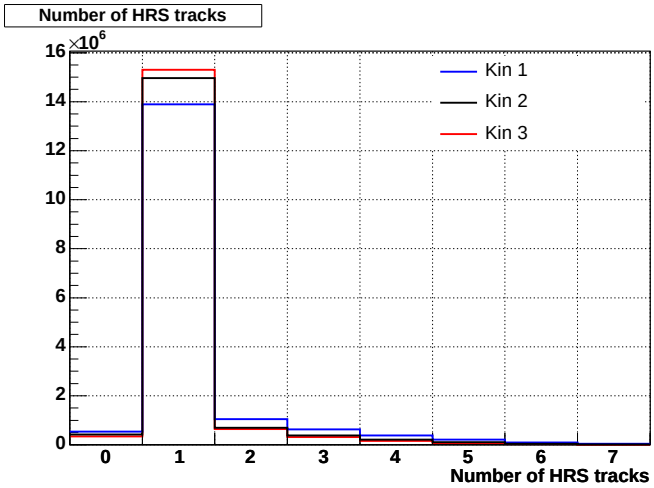

Figure 6.2: Number of tracks n_t in the HRS for each of the kinematic settings, normalized to the same number of events. Tab. 6.2 shows the percentage of 1-track events for each setting.

Kinematic setting	HRS angle (deg.)	Ratio $N_{n_t=1}/N_{n_t>0}$
1	15.58	+0.8499±0.0001
2	19.32	+0.9098±0.0001
3	23.91	+0.9264±0.0001

Table 6.2: Ratio of 1-track events to total number of events (number of tracks greater than zero) for each kinematic setting. Only 1-track events are considered for analysis, so results must be multiplied by the inverse of these ratios.

presented in Tab. 6.2 to correct for multi-track events.

6.2.3 Acceptance cut: R-function

A cut on data will be applied to select events in a flat acceptance region of the HRS. Trajectories very close to the nominal acceptance of the spectrometer are poorly reconstructed. Most importantly, a cut defining the HRS acceptance must be applied to *simulated* data in order to compute the solid angle of the experiment properly.

The acceptance region is complicated and depends on 5 variables: x_{tg}, y_{tg}, θ_{tg}, ϕ_{tg} and δ_{tg} (cf. section 3.1.2). These variables are correlated. Trajectories of higher momentum particles have lower curvature in the dipole, and in order for them to fit into the spectrometer they must have lower θ_{tg}. The dipole magnet has a trapezoidal cross section and higher momentum particles tend to fly closer to its shorter base (high magnetic field) side, and this makes the accepted range of ϕ_{tg} smaller for higher δ_{tg}. Finally, increasing y_{tg} requires decreasing ϕ_{tg} in order for the particle to get into the spectrometer entrance win-

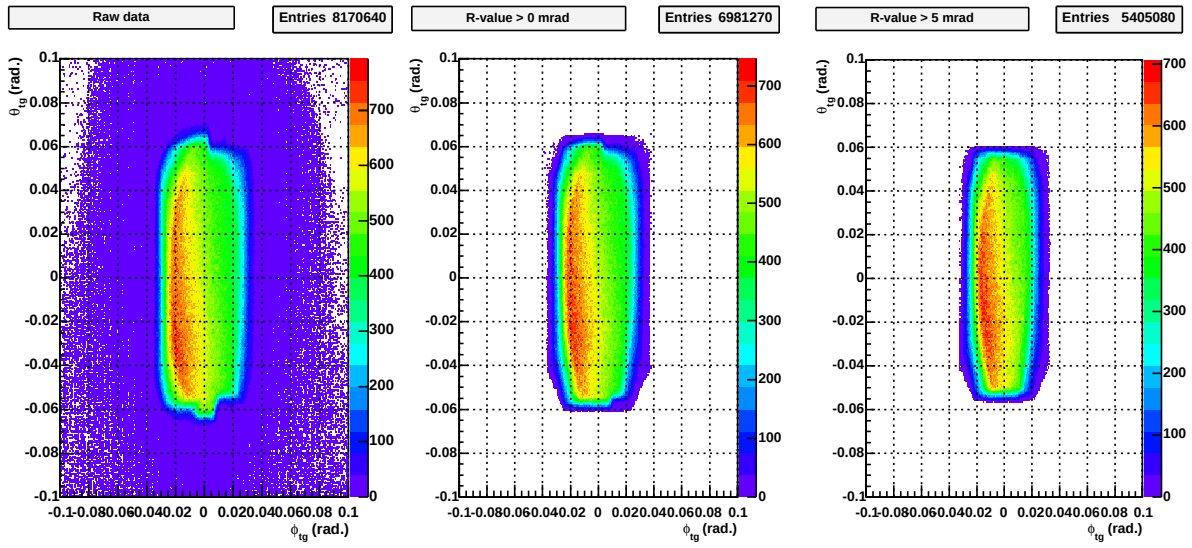

Figure 6.3: θ_{tg} vs. ϕ_{tg} for all data (kinematic 3), when only 1-track HRS events were selected, and for different values of the acceptance R-function. A cut requiring $R_{\rm val} > 0$ seems not sufficient to eliminate geometrical irregularities, such as the position of the NMR probes at the edges of the dipole gap. A cut requiring $R_{\rm val} > 5\,$mrad will be applied to both data and simulation to correctly compute acceptance.

dow. Making cuts independently in each of the variables to limit events to flat acceptance regions in each of them is very inefficient due to this kind of correlation. M. Rvachev *et al.* [58] have developed a more sophisticated acceptance function, called R-function, which allows one to place a 4-dimensional cut ($x_{tg} = 0$ is assumed) that is almost 2 times more efficient than "square" acceptance cuts. This function takes the arguments y_{tg}, θ_{tg}, ϕ_{tg} and δ_{tg} and returns a value which is the minimum distance (in radians) to the (θ_{tg}, ϕ_{tg}) solid angle acceptance region appropriate for a given value of y_{tg} and δ_{tg}.

Fig. 6.3 shows raw data with two different cuts on the return value $R_{\rm val}$ of the HRS R-function. A cut on $R_{\rm val} > 0$ includes everything inside the "nominal acceptance", which is defined by a magnetic field model of the HRS. Making a cut requiring $R_{\rm val} > 0.005\,$rad would include only the trajectories that lie 5 mrad or more inside the solid angle defined by the model for the specified y_{tg} and δ_{tg}. A cut on $R_{\rm val} > 0.005$ seems more appropriate. For $R_{\rm val} > 0$, we still see the locations of the NMR probes (used to measure the magnetic field) at the very edges of the dipole gap. In order to choose a flat acceptance region, which will match the Monte Carlo simulation, a cut on $R_{\rm val} > 0.005$ was made to data.

6.2.4 Cut on target length

Fig. 6.4 shows the distribution of the reaction point along the beam, v_z, reconstructed by the HRS after applying the HRS cuts described before. The overall location of the target relative to the Hall center is 7.8 mm downstream, as can be seen in Fig. 6.4. A cut was

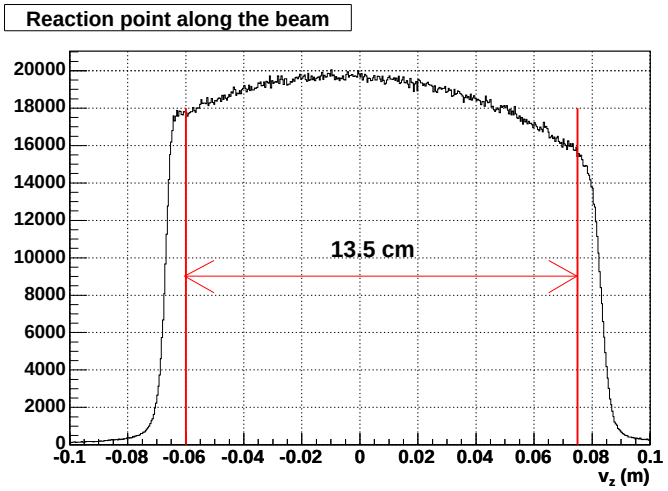

Figure 6.4: Reaction point along the beam reconstructed by the HRS. The cut on the target length applied is shown by the vertical lines. The figure shows the 7.8 mm downstream shift of the target during the experiment.

applied to the data in order to avoid the contribution from the target cell wall:

$$-6.00\,\text{cm} < \quad v_z \quad < 7.50\,\text{cm}\,.$$

Fig. 6.5 shows the resolution of the vertex reconstruction as measured with a carbon multifoil target. The thickness of each foil is 1 mm, and the HRS was at 37.69° during this run. The HRS vertex resolution varies as:

$$\sigma = \frac{\sigma_{90^\circ}}{\sin\theta_{\text{HRS}}}\,. \tag{6.1}$$

The σ measured at 37.69° is 1.87 mm, which means 1.2 mm at 90° (the σ introduced by the foil thickness is $1/\sqrt{12}$ mm and can be neglected).

The luminosity will be computed from the measured electron beam charged by assuming a 13.5 cm-long target (cf. section 6.8.1), in order to compensate for the cut applied on the target length.

6.3 Photon selection

We describe now how the electromagnetic calorimeter was analyzed and the cuts applied to select DVCS photons. The calorimeter trigger energy threshold was about 1 GeV during the experiment.

6.3.1 Waveform analysis parameters

The core of the calorimeter analysis is the ARS waveform algorithm described in chapter 3. Only 80 out of the 128 ARS samples were used for the calorimeter analysis in order

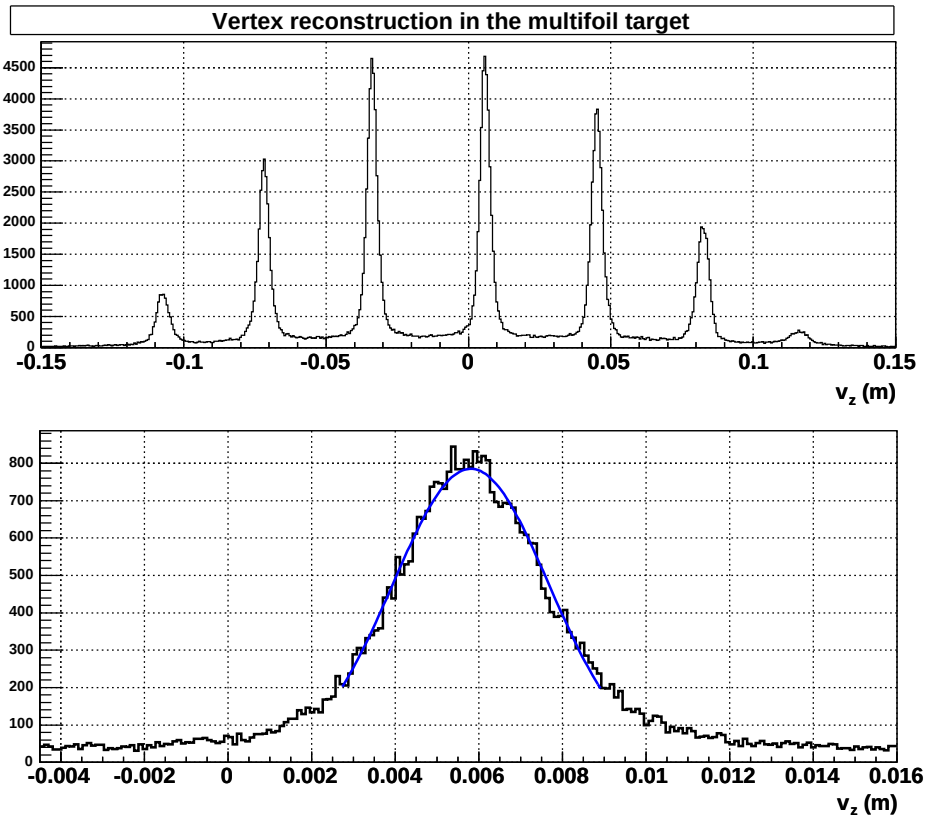

Figure 6.5: Resolution of the vertex reconstruction in a multifoil target (up). The central foil fit (bottom) leads to $\sigma = 1.9\,\text{mm}$. The foil thickness is 1 mm and the HRS was at 37.69° during this run.

to reduce the impact of accidental events. These 80 samples were chosen around the expectation time of the event in each calorimeter block. We searched for pulses in 45 ns time windows. The χ^2 of the fit was computed in a 40 ns window. Tab. 6.3 summarizes the waveform parameters used for the calorimeter analysis (the notation is explained in chapter 3). Fig. 6.6 shows the distribution of the number of pulses fit for kinematic 3.

6.3.2 Clustering

The calorimeter clustering algorithm was explained in section 3.3.1. The number of clusters in a given event is the number of local energy maxima within the clustering time window. This window was set to [-3,3] ns. Fig. 6.7 shows the calorimeter time spectrum for kinematic 3. The time resolution is 0.6 ns. The [-3,3] ns cut extends beyond 3σ and the number of events missed by this cut is less than 0.02% and can be neglected safely.

Fig. 6.8 shows the number of clusters in time (coincidence window [-3,3] ns) for each of the three kinematics settings. In order to select good DVCS event candidates, only events where the number of calorimeter clusters was equal to one were considered. The purity

Analysis window	$[i_{min},i_{max}]$	[0,80]	*Channel dependent*
χ^2-window	$[\chi^2_{min},\chi^2_{max}]$	[-20,20][1]	*Event and channel dependent*
1st-window	$[t_1^{min},t_1^{max}]$	[-20,25]	*Event and channel dependent*
2nd-window	$[t_2^{min},t_2^{max}]$	[-20,25]	*Event and channel dependent*
Resolution	$\Delta\tau$	4 ns	*Fixed*
0-pulse χ^2 threshold	χ^2_0	42 MeV	*Channel dependent*
1-pulse χ^2 threshold	χ^2_1	283 MeV	*Channel dependent*
2-pulse χ^2 threshold	χ^2_2	∞	*Fixed*

[1] This window is centered around the minimum of the pulse (remember PMT pulses are negative).

Table 6.3: Waveform analysis parameters for calorimeter analysis. See chapter 3 for more details. Analysis windows are channel and event dependent, so only the widths shown in this table are significant.

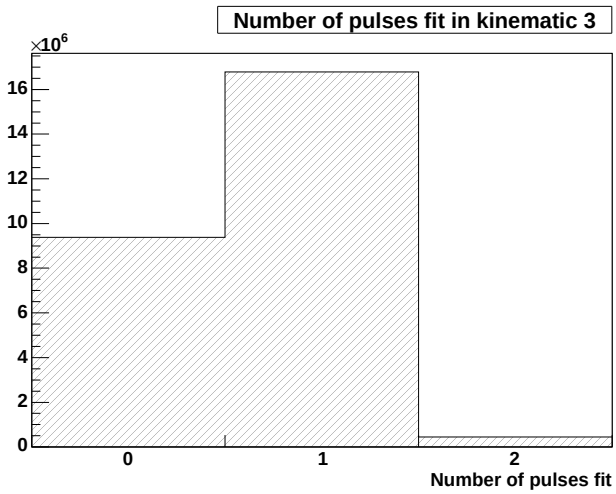

Figure 6.6: Number of pulses fit in calorimeter ARS analysis of kinematic 3. This is the average over the whole calorimeter. However, blocks closer to the beamline are noisier than those far away, and the number of pulses fit in these blocks is higher.

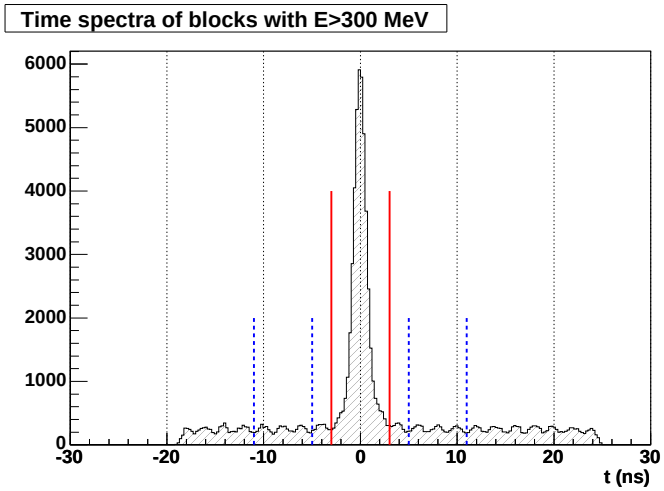

Figure 6.7: Time spectrum of blocks with $E > 300$ MeV in kinematic 3. It shows the 45 ns time window of waveform analysis. The 2 ns CEBAF beam structure can be seen. The coincidence [-3,3] ns window used for clustering is shown by the solid line. Dashed lines show windows used for HRS–calorimeter accidental subtraction.

and efficiency of this cut is a key issue of the analysis. It will be discussed in section 6.5, once the missing mass technique is presented.

6.3.3 Calorimeter geometrical cuts

A cut on the x_c and y_c reconstructed positions of clusters in the calorimeter is applied in order to eliminate events very close to the edges. These events are poorly reconstructed as most of the electromagnetic shower is not detected. Moreover, the simulation of showers at the edges is not as reliable as in the center of the calorimeter. Cutting events at the edges makes the acceptance calculation more accurate. A cut to eliminate all events reconstructed in one of the edge blocks of the calorimeter was made as follows:

$$\begin{aligned} -15\,\text{cm} < \quad & x_c \quad < 12\,\text{cm} \\ -15\,\text{cm} < \quad & y_c \quad < 15\,\text{cm}\,. \end{aligned}$$

The origin of this coordinate system is the intercept of the front face of the calorimeter with a normal line passing through the center of the Hall. This point is not the geometrical center of the calorimeter, which is shifted by 1.5 cm away from the beamline, due to geometrical and mechanical constraints. This explains the apparent asymmetrical cut on the variable x_c. Remember also that the calorimeter dimensions are $33 \times 36\,\text{cm}^2$, which explains the different sizes of the horizontal and vertical cuts.

Of course, identical cuts are applied to simulated events.

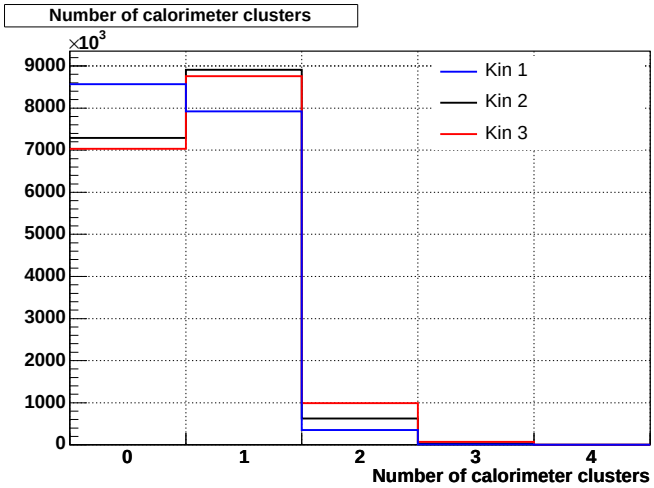

Figure 6.8: Number of calorimeter clusters in the coincidence window [-3,3] ns for each of the three kinematic settings. Distributions are normalized to the same number of events.

6.4 Proton selection

The proton selection is made by fixing an energy threshold and checking if there is a signal in time in the detector block expected by the DVCS kinematics, which can be fully determined by the electron and the photon.

Raw ARS data has been analyzed following the same algorithm used for the calorimeter, but with a different set of parameters, determined as explained in chapter 3. We give the values used here.

6.4.1 Waveform analysis parameters

Tab. 6.4 summarizes waveform analysis parameters used for the proton detector, with the notation explained in chapter 3. Fig. 6.9 shows the distribution of the number of pulses fit in the proton detector in kinematic 3. The number of pulses fit is much higher on average in the proton detector than in the calorimeter (cf. Fig. 6.6). The Čerenkov threshold in the calorimeter eliminates all the low energy hadronic background. This is not the case in the proton detector, where we are interested in detecting very low momentum protons.

6.5 Missing mass squared $M^2_{ep\to e\gamma X}$

With the information from the HRS and the calorimeter only, we can construct the missing mass squared

$$M^2_{ep\to e\gamma X} = (k + p - k' - q')^2 \,, \tag{6.2}$$

where k and p are the initial 4-vectors of the electron and the proton, and k' and q' the 4-vectors of the scattered electron and real photon respectively. Fig. 6.10 shows the result

Analysis window	$[i_{min},i_{max}]$	[45,75]	*Channel dependent*
χ^2-window	$[\chi^2_{min},\chi^2_{max}]$	[-20,20][1]	*Event and channel dependent*
1st-window	$[t_1^{min},t_1^{max}]$	[-20,20]	*Event and channel dependent*
2nd-window	$[t_2^{min},t_2^{max}]$	[-20,20]	*Event and channel dependent*
Resolution	$\Delta\tau$	4 ns	*Fixed*
0-pulse χ^2 threshold	χ^2_0	2.3 MeV	*Channel dependent*
1-pulse χ^2 threshold	χ^2_1	15.3 MeV	*Channel dependent*
2-pulse χ^2 threshold	χ^2_2	∞	*Fixed*
Baseline level	b	Fixed to 0	*Fixed*

[1] This window is centered around the minimum of the pulse (remember PMT pulses are negative).

Table 6.4: Waveform analysis parameters for the proton detector. See chapter 3 for more details. As in the case of Tab. 6.3, only the widths of these waveform analysis windows are significant, their absolute ranges varying event by event and channel by channel.

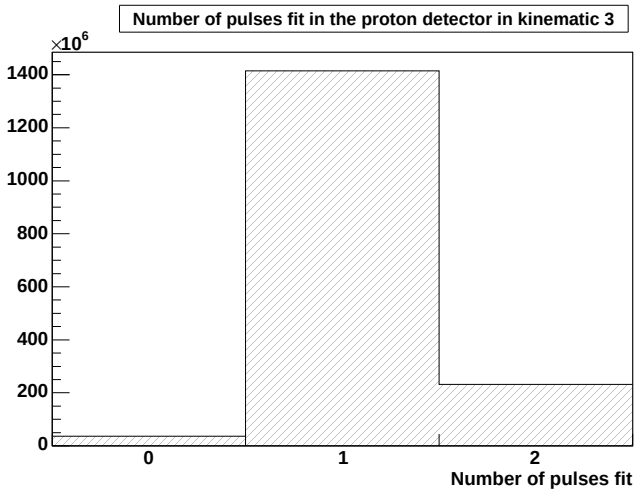

Figure 6.9: Number of pulses fit in the proton detector ARS analysis of kinematic 3. As in the case of the calorimeter, this shows the average over the whole detector. Blocks closer to the beamline have a higher number of pulses fit.

for kinematic 3, after accidental subtraction. The excess of events around the proton mass squared correspond to DVCS events (I will make no further difference between DVCS and BH from this point, as they are indistinguishable experimentally).

6.5.1 Sources of background

The main competing reactions that make the identification of the DVCS channel difficult are the following:

- Electroproduction of π^0: $e\ p \to e'\ p'\ \pi^0$, where the π^0 decays into two photons. The missing mass does not allow us to distinguish DVCS events from a very asymmetric decay of a π^0, where one of the photons takes most of the original π^0 energy and looks very much like a DVCS photon. This source of background needs to be subtracted, using the events where both photons from the π^0 decay are detected in the calorimeter and so the π^0 can be identified cleanly. The subtraction procedure is presented in section . However, the effect of π^0 electroproduction is expected to be small for several reasons:
  - the π^0 electroproduction cross section decreases $1/Q^2$ faster than DVCS [30],
  - no interference enhances the π^0 cross section, in contrast to the DVCS which is amplified by the BH,
  - theorists expect the beam helicity asymmetry of π^0 electroproduction to be very small.

  The π^0 cross section is in itself a very interesting measurement. In the DVCS kinematics, it is sensitive to another combination of GPDs [30]. This measurement has been done with data from this experiment and preliminary results can be found in [69].

- Associated DVCS (non-resonant): $e\ p \to e'\ N\ \gamma\ \pi$. It consists of the emission of an additional π. This reaction, which is suppressed with respect to DVCS [70], has a missing mass $M^2_{ep\to e\gamma X}$ starting at $(M_p + m_{\pi^0})^2$, where the π^0 is produced at rest. Higher momentum π's give higher missing masses. A cut on the missing mass squared will be applied to the data, as shown in Fig. 6.10, at the value $(M_p + m_{\pi^0})^2$ in order to eliminate this contribution. Due to detector resolutions, a small fraction of this kind of event can still satisfy the cut. An evaluation of this effect is presented below.

- Associated DVCS through a resonance: $e\ p \to e'\ (\Delta \text{ or } N^*)\ \gamma$, where the resonance decays into a nucleon and a pion. The first resonance $\Delta(1232)$ gives a contribution to the missing mass squared distribution at around $1.5\,\text{GeV}^2$. Taking into account its width and the detector resolutions, the probability of contamination under the tight cut $M_X^2 < (M_p + m_{\pi^0})^2$ is small. However, an estimate is presented below. Also, the $\Delta(1232)$ cross section ($e\ p \to e'\ \Delta\ \gamma$) has been estimated to be one order of

magnitude smaller than the DVCS in our kinematics [71]. Moreover, the asymmetry is predicted small compared to that of DVCS.

Fig. 6.11 shows the same missing mass squared when a DVCS proton is detected in the proton detector: a signal over 30 MeV in the detector block expected by DVCS kinematics in a coincidence time window [-1,1] ns. Accidentals in a triple coincidence are negligible and were not subtracted from this histogram. Most of the high missing mass background disappears in the case of exclusive detection. The tail at high missing mass has a multiple origin. Calorimeter leaks and radiative corrections both generate this kind of tail. These two effects are well described by the Monte Carlo simulation. Physical background not taken into account in the simulation can explain the difference between the data and the simulation (cf. Fig. 6.11).

Even though the missing mass distribution is much cleaner when the recoil proton is detected, the acceptance of the experiment is highly reduced. Indeed, many DVCS photons can hit the calorimeter with the associated recoiling proton falling outside the acceptance of the proton detector. This happens especially for low $-t$ events, where the proton goes through the electromagnetic calorimeter without being detected.

By making a tight cut on the missing mass squared distribution of Fig. 6.10, so that the contamination from background can be neglected, the acceptance of the measurement is greatly increased, reducing the statistical errors. A cut $M_X^2 < (M_p + m_{\pi^0})^2$ was applied to data. The possible contamination from background with this tight cut is very small. In order to make such a tight cut safely, the distribution width and tail should be well reproduced in the Monte Carlo simulation, where an identical cut will be made to compute the acceptance. Fig. 6.11 shows the distribution obtained in the simulation (green), compared to the one when all three particle in the final state are detected in the experiment. The distribution width and tail are remarkably well reproduced well above the applied cut.

Fig. 6.12 shows an estimate of the background remaining under the $M_X^2 < (M_p + m_{\pi^0})^2$ cut. The raw HRS–calorimeter missing mass squared spectrum of Fig. 6.10 (in black) was fit up to 1.1 GeV^2 with the exclusive distribution of Fig. 6.11. The background that remains below $M_X^2 = (M_p + m_{\pi^0})^2$ is only 1.71% of the total. Bear in mind that only background which shows a single spin asymmetry would contaminate the observable presented at the end of this chapter. This estimate does not include the effect of π^0 electroproduction, which must be subtracted independently. The exclusive distribution of Fig. 6.11 was multiplied by 4.7 to fit the HRS–calorimeter distribution. This factor corresponds the acceptance decrease that is imposed by a requirement of proton detection.

Finally, the stability of results over the variation of the missing mass cut will be shown in section 6.10.

6.5.2 Efficiency of the 1-cluster cut

When only 1-cluster events are considered for analysis, two essential issues arise:

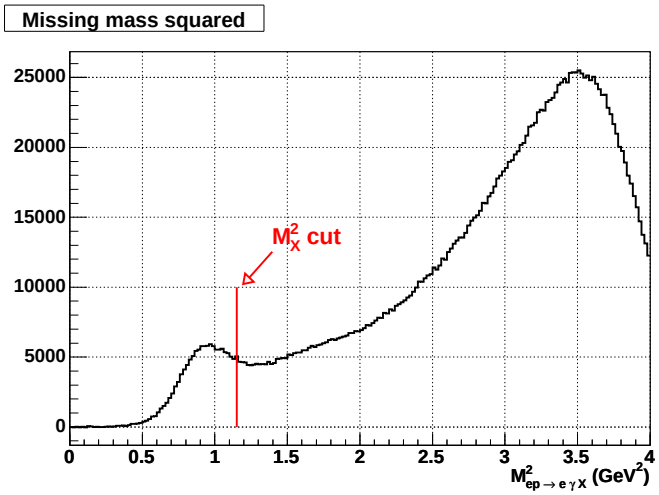

Figure 6.10: Missing mass squared $M^2_{ep\to e\gamma X}$ for kinematics 3 with all HRS and calorimeter cuts described before. The cut on the missing mass applied on data $M^2_X < (M_p + m_{\pi^0})^2$ is shown by the solid line. Accidental events have been subtracted using the time windows of Fig. 6.7.

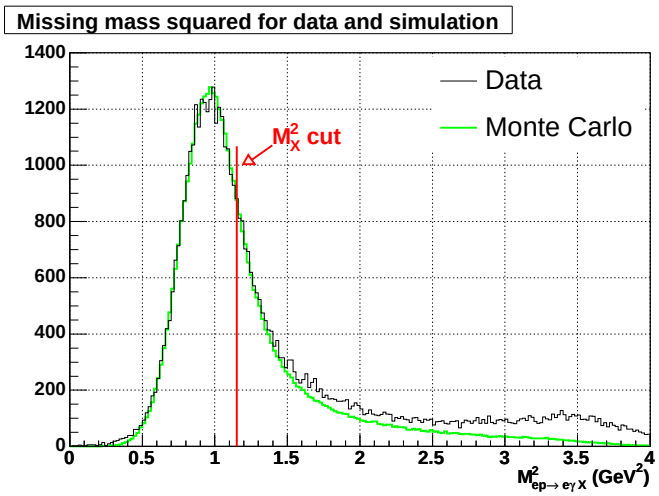

Figure 6.11: Missing mass squared $M^2_{ep\to e\gamma X}$ when an event over 30 MeV is detected in the expected proton detector block in a coincidence time window of [-1,1] ns. The missing mass squared cut applied on data is also shown. A comparison with the missing mass squared distribution obtained in the Monte Carlo simulation is plotted, normalized to the same maximum value. The missing mass squared distribution is well reproduced by the Monte Carlo simulation up to the cut applied to data and beyond.

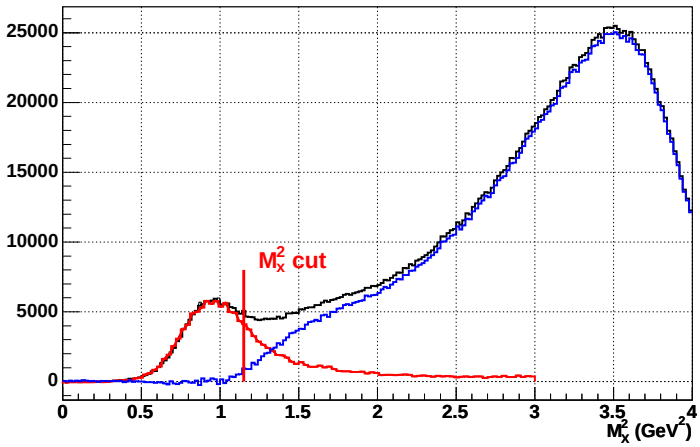

Figure 6.12: The raw HRS–calorimeter missing mass squared spectrum of Fig. 6.10 (in black) was fit up to 1.1 GeV^2 with the exclusive distribution of Fig. 6.11. This allow the evaluation of the background under the cut $M_X^2 < (M_p + m_{\pi^0})^2$ in the raw spectra, which is 1.7%. As a result of the fit, the exclusive distribution was multiplied by 4.7 to fit the HRS–calorimeter one.

- The purity of the cut, i.e. how many 1-cluster events are not DVCS events. This issue was treated in section 6.5.1.

- How many DVCS events, originally 1-cluster events, will appear as 2-cluster events in the data, and so be missed in the analysis. This can happen if an accidental event elsewhere in the calorimeter occurs in the coincidence window [-3,3] ns.

  When dealing with 2 clusters, several combinations are possible:

  - Both clusters are in coincidence (with the electron detected in the HRS). This is a likely π^0 event. I will call N^{cc} the total number of this type of event.
  - Both clusters are accidental (not in coincidence with the HRS electron), but in time between themselves. This is the case of an accidental π^0, when the two photons of the decay are detected in the calorimeter. I will call the number of these events N^{aa}.
  - Finally, the case where one of the clusters is in time with the HRS, and the other cluster is accidental. These events are the ones that are likely to be a DVCS events. The number of this kind of events, N^{ac}, must be evaluated. The number of events of this kind where one of the clusters gives a contribution to the missing mass squared below the cut applied $M_X^2 < (M_p + m_{\pi^0})^2$ would represent a correction to the data, accounting for the inefficiency of the 1-cluster cut.

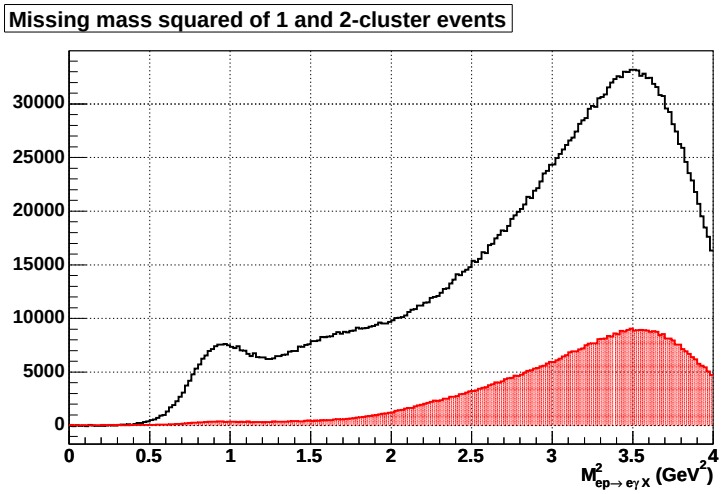

Figure 6.13: Missing mass squared for 1-cluster events and for each of the clusters in 2-cluster events (shaded histogram), after accidental subtraction, and for the kinematic setting 3. The number of 2-cluster events with $M_X^2 < (M_p + m_{\pi^0})^2$ is 5.5% of the number of 1-cluster events in the same M_X^2 region.

The total number of 2-cluster events is:

$$N_{2c} = N^{cc} + N^{aa} + N^{ac} \,. \tag{6.3}$$

The contribution of N^{aa} to N_{2c} can be easily evaluated by doing exactly the same analysis of the data, but with a clustering window that is shifted by a few ns from the coincidence peak (cf. Fig. 6.7). Once this subtraction has been made, the missing mass squared $M^2_{ep\to e\gamma X}$ distribution for each of the clusters in 2-cluster events have been plotted (Fig. 6.13). Accidental π^0's, whose contribution has been noted N^{aa} above, do not yield photons under the missing mass of a proton and below the cut $M_X^2 < (M_p + m_{\pi^0})^2$. However, events N^{ac} can have one of the photons at the right missing mass. We must correct for these events. Fig. 6.13 shows also the missing mass squared distribution for 1-cluster events (where accidentals have also been subtracted), in order to estimate the size of the correction. The correction factors to be applied to data to account for the omission of 2-cluster events are calculated as the number of 2-cluster events under $M_X^2 < (M_p + m_{\pi^0})^2$ with respect to the number of 1-cluster events under the same missing mass squared cut. The correction factors for each of the kinematic settings are shown in Tab. 6.5. The correction depends on the accidental rate, which is larger for smaller calorimeter angles θ_{γ^*}. As can be seen from the values of Tab. 6.5, this correction is small. This justifies the omission of 2-cluster events in this analysis, with a correction being made to the final result. Furthermore, we can neglect the correction for the case of 3-cluster and higher-cluster events.

Kinematic setting	θ_{γ^*} (deg.)	N_2/N_1 (%)	Correcting factor
1	22.29	1.2	1.012
2	18.25	2.0	1.020
3	14.80	5.5	1.055

Table 6.5: Ratio of 2-cluster events N_2 with $M_X^2 < (M_p + m_{\pi^0})^2$ to 1-cluster events N_1 in the same M_X^2 region for each of the kinematic settings. The correcting factor to be applied to data due to the omission of 2-cluster events in the analysis is also shown.

6.6 π^0 electroproduction subtraction

The π^0 decay into two photons in the center-of-mass is isotropic, each of the two photons carrying half the π^0 initial energy. In the lab frame, we can find two different kinds of decays, illustrated in Fig. 6.14. If the direction of the boost and the direction of the

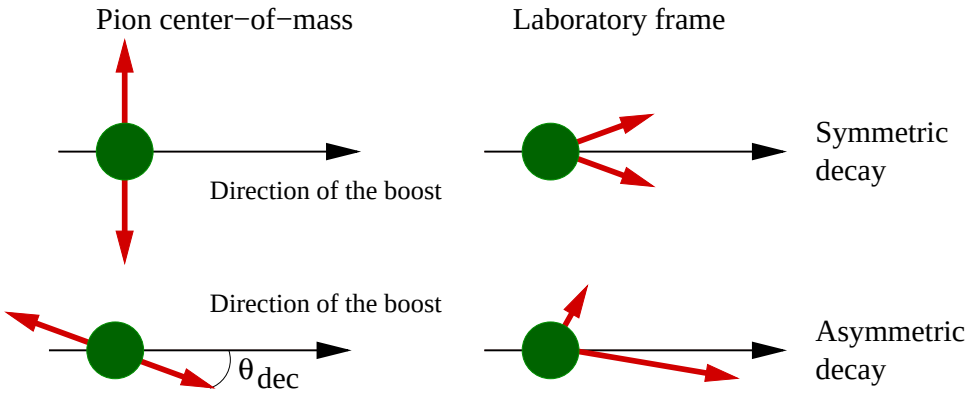

Figure 6.14: Two different kinds of π^0 decays. When both photons are emitted perpendicular to the direction of the boost in the π^0 center-of-mass, the decay is symmetric in the lab frame, with both photons emitted in the forward direction and each carrying half of the π^0 energy. When both photons hit the calorimeter they generate two distinct clusters and do not contaminate the DVCS sample. If the direction of the emitted photons in the π^0 center-of-mass is very close to the direction of the boost, one of the photons carries most of the π^0 energy in the lab frame; the other is emitted at large angle and has low energy so that it is rarely detected in the calorimeter. This kind of events are the ones which contaminate DVCS events.

photons emission in the center-of-mass frame are nearly perpendicular, the decay is almost symmetric in the lab frame, i.e. each photon carries half of the π^0 initial energy and both photons are emitted in the forward direction. This is the typical case where both photons are detected in the calorimeter. The kinematics of the decay imply an angle α between both photons given by

$$\cos\alpha = 1 - \frac{m_{\pi^0}^2}{2E_1E_2},$$

which is minimum when the energy of each of the photons E_1 and E_2 are both equal to half of the π^0 energy. The maximum π^0 energy in our kinematics is around 3.5 GeV. This maximum value is a consequence of the 5.75 GeV beam energy and the fact that a scattered electron is detected in the HRS, with at least 2.35 GeV (lowest momentum setting). The smallest angle between the two photons of a π^0 decay is then $\alpha_{\min} = 4.4°$. Each calorimeter block has a transverse size of 3 cm, which at a distance of 1.1 m makes 1.6°. This implies that there are always more than two blocks between the impact points of each of the photons in the calorimeter. The clustering algorithm described in section 3.3.2 can thus separate both clusters, as there are two local energy maxima in the calorimeter. This kind of π^0 decays are well identified as 2-cluster events and do not constitute a source of background for DVCS events.

The case where the angle θ_{dec} between the direction of the boost and the direction of the photons emission in the center-of-mass frame is small yields a very asymmetric decay in the lab frame, with one of the photons carrying most of the π^0 energy and emitted very close to the initial π^0 direction. In this case, only this high energy photon is typically detected in the calorimeter, the event looking very much like a DVCS event. The other photon is not detected either because it is emitted at a very large angle, outside the calorimeter acceptance, or because its energy is below the calorimeter energy threshold. This kind of events contaminate the DVCS sample and their contribution need to be subtracted.

In principle, in order to subtract π^0 events from our DVCS sample accurately, we need to know their cross section as a function of the relevant kinematic variables such as Q^2, t, x_B and φ, convolute the result by the acceptance of the experimental apparatus and calculate the number of π^0 events in each of the experimental bins in Q^2, t and φ, using the value of the experiment integrated luminosity. We develop in the following section a much more elegant and direct way to determine the π^0 contamination to the DVCS event sample [72].

6.6.1 Subtraction procedure

In order to subtract π^0 events where only one photon is detected in the calorimeter, we will use the events where both photons hit the calorimeter. By using 2-cluster events from π^0 decays, we have the right distribution of events as a function of the kinematic variables Q^2, t, x_B and φ. The decay itself is isotropic and we can simulate it, by randomly sampling the angle θ_{dec} between the direction of the boost and the direction of the photons emission in the center-of-mass frame. By this procedure we can determine the *number* and the *kinematics* of 1-cluster events generated by each π^0 of the measured sample (2-cluster events). The detailed procedure is explained in the following.

6.6.1.1 π^0 selection

The standard photon cuts described in section 6.3 were applied to each of the 2 clusters used to identify a π^0, in addition to the standard electron cuts of section 6.2. Moreover,

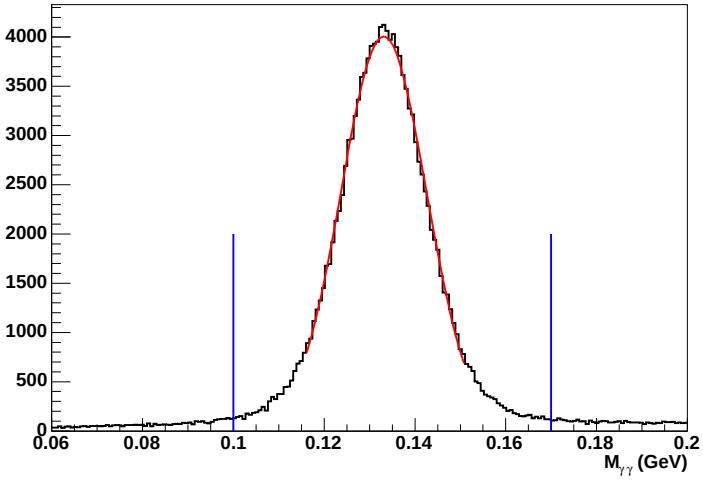

Figure 6.15: Invariant mass of 2-cluster events with the electron cuts of section 6.2 and the photon cuts of section 6.3 in each of the clusters. Additionally, each of the clusters has an energy greater than 0.9 GeV. The width of the distribution is 9.5 MeV and is centered around 133 MeV. Vertical lines show the cut applied to select π^0 events, which is beyond $\pm 3\sigma$ from the mean.

a cut was applied on the invariant mass $M_{\gamma\gamma}$ of the 2 photons, defined by:

$$M_{\gamma\gamma} = \sqrt{(q_1 + q_2)^2}\,, \tag{6.4}$$

where q_1 and q_2 are the 4-momenta of each of the photons. Fig. 6.15 shows the invariant mass of events where both clusters have more than 0.9 GeV for kinematic setting 3. The distribution width is 9.5 MeV. A cut of ± 35 MeV around the π^0 mass was applied in the invariant mass of the event, and is shown by the vertical lines in Fig. 6.15.

6.6.1.2 Randomization of the decay

For each selected π^0, its decay is randomized a large number of times $n_{\rm dec} = 5000$. This is made by uniformly sampling the variable $\cos\theta_{\rm dec}$ between -1 and 1 and the azimuthal angle of the decay $\phi_{\rm dec}$ between 0 and 2π. The impact point of each photon at the surface of the calorimeter is then computed. The number of photons above the calorimeter threshold which fall within the calorimeter acceptance are then determined:

n_0 : number of events where none of the photons are detected,
n_1 : number of events where one and only one photon is detected,
n_2 : number of events where both photons are detected,

with

$$n_0 + n_1 + n_2 = n_{\rm dec} = 5000\,. \tag{6.5}$$

Each of the n_1 events where one and only one photon is detected is subtracted from the corresponding experimental bin of DVCS events, according to its kinematics. As a

large number of events $n_{\rm dec}$ were generated for each 2-cluster π^0 event, each 1-cluster event is weighted by $1/n_{\rm dec}$. Moreover, only the 2-cluster subset of π^0 events was used for the subtraction. In order to account for this effect, each event is additionally weighted by $(n_0+n_1+n_2)/n_2$. The final weight that each 1-cluster event receives is:

$$W = \frac{1}{n_{\rm dec}} \cdot \frac{n_0+n_1+n_2}{n_2} = \frac{1}{n_2}\,. \tag{6.6}$$

6.6.2 Systematic errors

There are two main sources of systematic error in this procedure. The first one is due to edge effects in the calorimeter. Only π^0 where both photons hit the calorimeter are subtracted. However, the calorimeter acceptance for 2-cluster events is smaller than the one for 1-cluster events. A π^0 aiming close to one of the calorimeter edges may only leave 1 photon in the calorimeter, in spite of decaying in a very symmetric way. This kind of events are not subtracted with the procedure described before, which underestimates the contamination in areas close to the calorimeter edges. In order to estimate the efficiency of the subtraction procedure, it has been simulated with Monte Carlo events. π^0 events have been generated in the phase space of the experiment, the response of the calorimeter simulated using the Monte Carlo package described in chapter 5, and the subtraction procedure applied. Figure 6.16 shows the efficiency of the algorithm, i.e. the number of 1-cluster π^0 events found with the subtraction procedure, normalized to the number of 1-cluster events found in the Monte Carlo simulation. The efficiency in Fig. 6.16 is plotted as a function of a cut in the $x_c - y_c$ position of the 1-cluster event found by the subtraction method:

$$\sqrt{x_c^2+y_c^2} < \text{Distance to center cut}\,. \tag{6.7}$$

As shown in Fig. 6.16, the efficiency is higher than 80% up to the useful edges of the calorimeter (15 cm and 16.5 cm in the horizontal and vertical direction respectively), and slightly smaller ($\sim$ 72%) if we include the corners. A careful Monte Carlo simulation (with some input on the π^0 electroproduction cross section) can be used to correct for these edges effects. At this point, as we shall see, the contamination of π^0 in the difference of DVCS cross-sections is found to be small and we have not corrected for this systematic error.

The second source of systematic error is the uncertainty in the knowledge of the calorimeter threshold, which directly affects the values n_1 and n_2 of 1-cluster and 2-cluster events found. Indeed, the energy distribution of each of the photons in the lab frame is flat:

$$E^{lab} = 1/2\ m_{\pi^0}\gamma(1-\beta\cos\theta_{\rm dec})\,, \tag{6.8}$$

where $\beta = v/c$ is the π^0 relative velocity and $\gamma = 1/\sqrt{1-\beta^2}$ the usual Lorentz boost parameter. The number of photons below or above a given energy threshold E_{th} is proportional to the threshold value:

$$n_1 = C\cdot E_{th} \;\Rightarrow\; \frac{dn_1}{n_1} = \frac{dE_{th}}{E_{th}}\,. \tag{6.9}$$

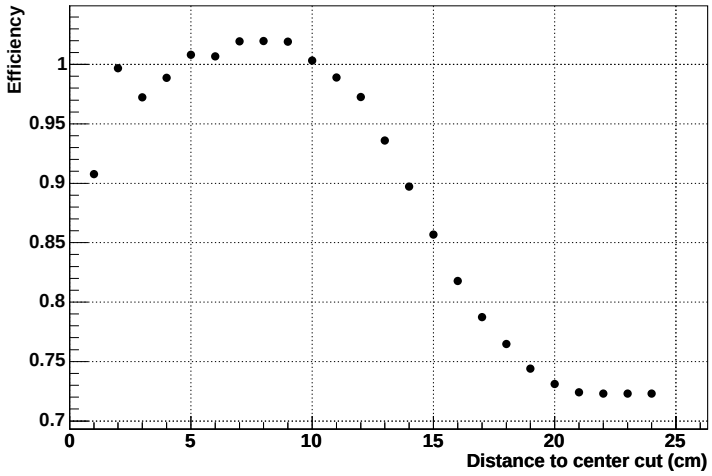

Figure 6.16: Efficiency of the π^0 subtraction procedure as a function of a circular cut around the calorimeter center, evaluated by Monte Carlo simulation. The efficiency is higher than 80% up to the calorimeter edges and $\sim 72\%$ taking the corners into account.

Thus, the relative increase of 1-cluster events (or decrease of 2-cluster events) is equal to the relative uncertainty of the calorimeter energy threshold. The calorimeter threshold has been calculated in a run-by-run basis and as a function of the calorimeter block in the same way as the calorimeter calibration coefficients. A very conservative estimate of its systematic error is 5%. The weights of Eq. (6.6) are affected by this uncertainty, i.e 5%.

6.6.3 Results

Fig. 6.17 shows the missing mass squared distribution of 1-cluster π^0 events for the kinematic setting 3. Under the missing mass squared cut $M_X^2 < (M_p + m_{\pi^0})^2$, the contamination of π^0 is 14% of the total number of 1-cluster events (π^0+ DVCS). However, we are interested in the difference of DVCS cross sections for opposite helicities. Fig. 6.18 shows an estimate of the π^0 single single spin asymmetry (SSA):

$$\mathrm{SSA} = \frac{\sigma^{\rightarrow} - \sigma^{\leftarrow}}{\sigma^{\rightarrow} + \sigma^{\leftarrow}}. \tag{6.10}$$

Accidentals have not been subtracted for this estimate, but their number is small in the case of a π^0 detection (as shown in Fig. 6.15) because a triple coincidence is required (scattered electron and the two photons of the π^0 decay). The π^0 electroproduction SSA is around 4%. The overall contamination of π^0 to our observable is then much smaller than 14%. The exact treatment will be discussed in section 6.10, once results on DVCS are presented.

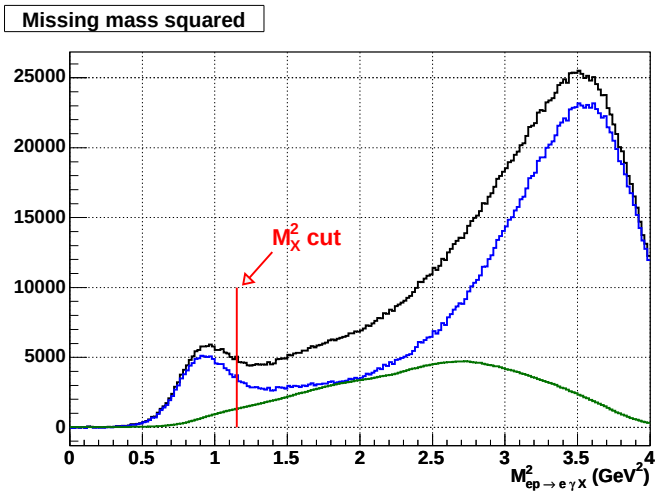

Figure 6.17: Missing mass squared distribution $M^2_{ep\to e\gamma X}$ for kinematic 3 (black). The contribution of 1-cluster events is plotted in green. The missing mass squared distribution, once 1-cluster π^0 events has been subtracted, is shown in blue. The contribution of π^0 under the missing mass squared cut at $(M_p + m_{\pi^0})^2$ is 14% of the total number of events under the cut.

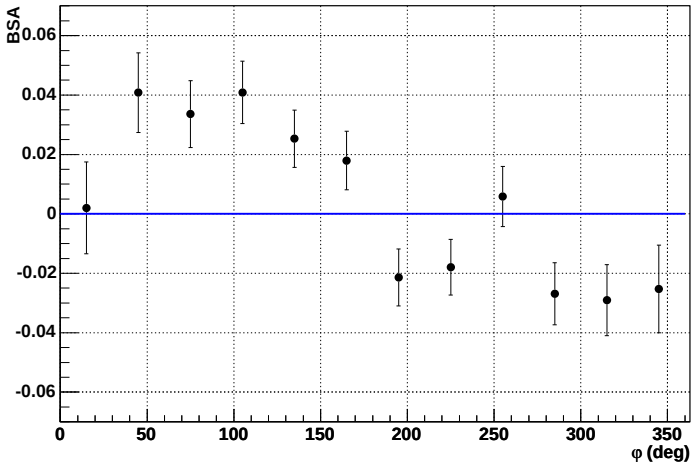

Figure 6.18: Estimate of π^0 electroproduction SSA for kinematic setting 3. Accidentals have not been subtracted, but their number is small (cf. Fig. 6.15).

6.7 Computation of kinematic variables

The calorimeter resolution is the limiting factor in the determination of the reaction kinematics, the electron measurement by the HRS being much more accurate. However, the angular resolution of the calorimeter is much better than its energy resolution. Since the DVCS reaction is over constrained, we can use the angles of the detected particle in the calorimeter, and not its measured energy, when computing the kinematics of the event. Fig. 6.19 shows the resolution in the kinematic variable t obtained in the Monte Carlo simulation. The black histogram shows the difference between the measured variable t at the calorimeter and the one at the vertex of interaction, when t is computed using the 4 components of the detected particle q' as:

$$t = (k - k' - q')^2 . \tag{6.11}$$

By assuming the kinematics of a DVCS event and using only the *position* of the detected photon in the calorimeter, we can compute t as:

$$t = \frac{Q^2 M + 2\nu M(\nu - \sqrt{\nu^2 + Q^2}\cos\theta_{\gamma\gamma^*})}{\sqrt{\nu^2 + Q^2}\cos\theta_{\gamma\gamma^*} - \nu - M} , \tag{6.12}$$

where no calorimeter variable appears other than the angle $\theta_{\gamma\gamma^*}$ between the detected photon and the virtual photon $q = k - k'$. The resolution obtained with this procedure is shown in red in Fig. 6.19, and is 3 times better than the resolution obtained using full 4-vectors as in (6.11).

The same technique can be used to calculate which block of the proton detector should be hit by a DVCS event, further increasing the accuracy of the calculation.

6.8 Normalization

Other than detector efficiencies, several global normalization must be applied to the data in order to obtain absolute cross sections. These section describes how these normalizations were determined.

6.8.1 Luminosity

For electrons of a total charge Q passing through the target of length l containing LH_2 of density ρ, the integrated luminosity is given by

$$\int \mathcal{L}\, dt = \frac{Q}{e}\frac{N_A \rho l}{A_H} , \tag{6.13}$$

where $e = 1.602 \cdot 10^{-19}$ C is the electron charge, $A_H = 1.0079\,\mathrm{g/mol}$ is the atomic mass of H, and $N_A = 6.022 \cdot 10^{23}\,\mathrm{mol}^{-1}$ is Avogadro's number.

The charge Q passing through the LH_2 target during a run can be found with a high precision with BCMs (section 2.2.2.3). The target length l was measured to be

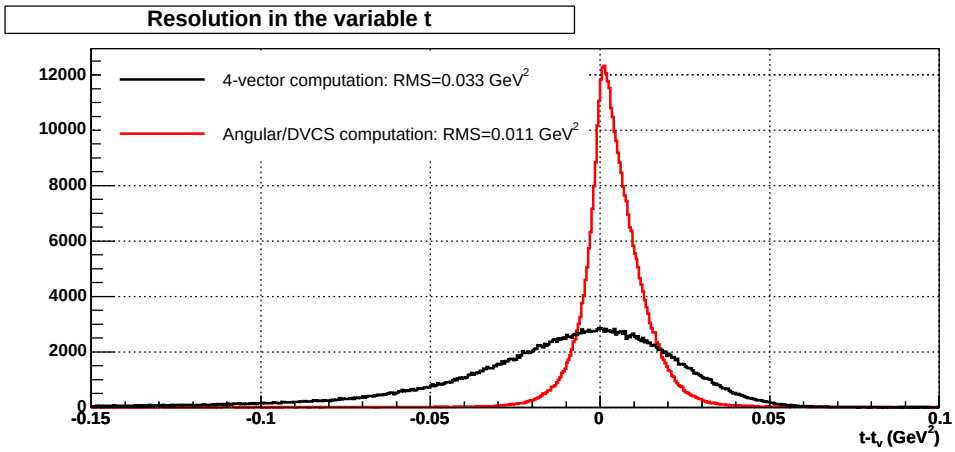

Figure 6.19: Resolution in the determination of the kinematical variable t, using 4-vectors (black), like in Eq. (6.11), and using only the angular position of the photon (in red) assuming DVCS kinematics, as in Eq. (6.12). These resolutions are calculated with the Monte Carlo simulation of the calorimeter. Using only the position of the detected photon in the calorimeter increases the resolution in the determination of the kinematics of the reaction by a factor 3.

Kinematic setting	Q_{+1} (C)	Q_{-1} (C)	$Q_{+1,-1}$ (C)	Q_{asy} (10^{-3})	$\int \mathcal{L}_{+1,-1}\, dt$ (fb^{-1})
1	0.3732	0.3733	0.7464	-0.10	2717
2	0.5287	0.5292	1.0580	-0.58	3851
3	0.6913	0.6937	1.3850	-1.70	5041

Table 6.6: Total charge accumulated during each kinematic setting and the corresponding integrated luminosities. Only charge during well-defined helicity gates is considered. Luminosity is computed for a 13.5 cm-long target (cf. section 6.2.4).

15.0 cm, but due to the cut on the target length (section 6.2.4), the effective length for luminosity purposes is 13.5 cm. The density ρ of LH_2 depends of the target temperature and pressure. The target was operated at 19 K and pressure of 25 psi, which gives a density of $\rho = 0.07229\,g/cm^3$

The helicity of the event appears in the data stream as –1, 0, and +1. A "0" means it is undefined. This happens during the approximately 500 μs it takes for the Pockel Cell (PC) to flip. The PC is an electro-optical element that determines the helicity of the laser which in turn determines the electron helicity. It takes some time for the $\sim$ 3 kV to settle (it flips from +3 kV to -3kV). There is a lost of 500 μs out of 30 ms (1.6% deadtime). Helicity undefined events are removed for analysis and so the corresponding correction needs to be done. Tab. 6.6 shows for each kinematic setting the total charge and integrated luminosity of events where the helicity is defined (+1 or –1). This is done by taking the BCM scaler readings which only count during well defined helicity gates [73].

6.8.2 Beam polarization

The beam polarization was measured during the whole experiment concurrently with regular data taking. Beam polarization results can be obtained readily from the electron detector of the Compton polarimeter. This electron detector consists of 4 planes of 48 silicon micro-strips, placed 4.6 mm above the beam axis during the DVCS experiment. Fig. 6.21 (left) shows the electron counting rate versus strip number in one of the detector planes for a typical Compton run of 3 h duration. The detector is located behind the third dipole of the Compton chicane and the strip number gives the position of the scattered electron along the dispersive axis with a resolution of 200 μm. Hence the horizontal axis of the plot is proportional to the energy lost by the electron (and given to the photon). The Compton energy spectrum shows up as a relatively flat rate on the first strips. The background spectrum has a $1/E$ shape, like bremsstrahlung. The differential asymmetry as a function of the electron energy (strip number) is shown in the right plot of Fig. 6.21.

The systematic error in the polarization measurement due to the uncertainty of the laser polarization is 0.7%. The maximum deviation of scattered electrons for a beam energy of 5.75 GeV is 21.5 mm at the electron detector plane, which makes a calibration error of 200 μm/21.5 mm=0.93%; this corresponds to a 1.9% uncertainty in the polarization measurement. The total systematic error is then 2.0%. An improvement of the 1.9% electron detector calibration error can be achieved by analyzing the correlated events in the photon detector. However, the analysis of this detector is more complex and the polarization results obtained with the electron detector alone are sufficiently accurate at this point in the analysis.

Fig. 6.21 shows the Compton polarimeter results during the full experiment [74], where only the electron detector was used in the analysis. Beam polarization was $75.3 \pm 0.1_{\rm stat} \pm 1.5_{\rm syst}$% on average during the experiment. The low polarization values at the beginning of the experiment (the first 3 points in Fig. 6.21) correspond to an incorrect setting of the Wien filter. The Wien filter is a spin rotator consisting of crossed electric and magnetic field, used to maximize the longitudinal beam polarization at the target position.

6.8.3 Acquisition deadtime correction

The acquisition deadtime (DT) arises due to the inability of the DAQ system to record events occurring during a DAQ "dead time", when it is recording another event. The total time that the DAQ is *busy* recording events is measured by counting pulses from a 62.5 MHz clock (in a gated scaler). By comparing its total count at the end of a run to a *free* running clock (counting continuously), we can determine precisely the dead time of the acquisition system for each run.

However, beam is not available continuously during the duration of the run. The beam is shut down quickly (*beam trip*) each time a superconducting cavity arcs, in order to protect the cavities from arc damage. At 5.75 GeV beam energy, the cavities are pushed well beyond the initial accelerating gradient specifications and the beam trip rate is sometimes large. A beam trip can last from a few seconds to a few minutes. During this

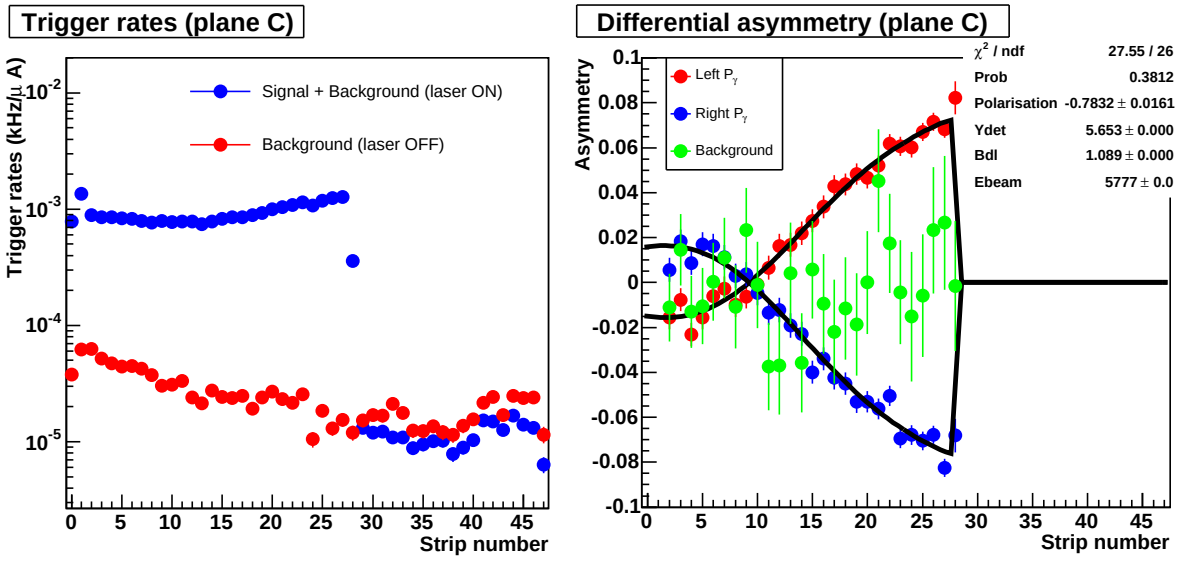

Figure 6.20: Signal and background rates (normalized to the electron beam current) in one of the planes of the electron detector for each strip (left), and the asymmetry measured for each of the laser polarization states and the background (right).

time, the DAQ system is ready to record events, but beam is not available. The counting of the *free* scaler during a beam trip needs to be subtracted from the total in order to properly take into account the time the DAQ was actually busy, normalized to the total time when it was not (but that events could be recorded, i.e. beam was available).

Beam trips were automatically subtracted by considering the time between two recorded events, measured by the *free* running scaler. Typical acquisition rates were between 25–60 Hz. A beam trip was considered whenever the time between two consecutive events was larger than 1 s.

Tab. 6.7 shows for three typical runs (about 45 min of data taking), each corresponding to a different kinematic setting, the value of the DT correction. These corrections were calculated following the procedure described above for each individual run [73]. As shown in Tab. 6.7, DT depends strongly on the kinematic setting, as the acquisition rate varies from approximately 25 to 60 Hz.

6.9 Extraction of observables

I will describe in this section the procedure followed to take into account the acceptances of detectors in extracting physical quantities.

To derive differential cross sections from the measured data, the solid angle (or acceptance) Ω of the detection apparatus must be known accurately. The number of counts in

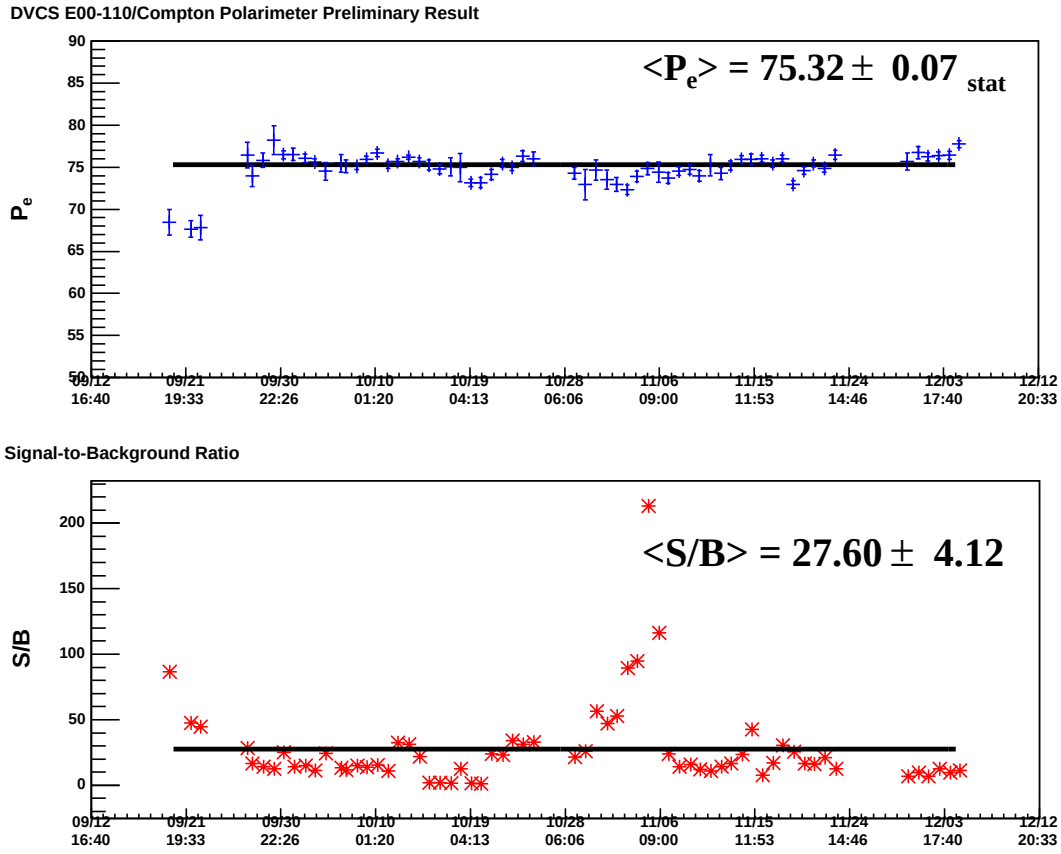

Figure 6.21: Compton polarimeter results [74], using only the electron detector. Beam polarization is shown in the upper plot. Lower plot shows the signal to background ratio. The first three points in the beginning of the experiment correspond to an incorrect Wien angle setting.

Kinematic setting	Trigger rate (Hz)	DT correction (%)	Number of beam trips
1	62	40.4	11
2	39	27.7	22
3	23	14.3	20

Table 6.7: Typical DT corrections to be applied to data as a function of the kinematic setting. The acquisition rate was the highest in kinematic 1 and so the DT correction also. These values are for three specific runs (about 45 min of data taking), but the DT correction was calculated in a run-by-run basis and data corrected correspondingly [73]. The number of beam trips is also shown as reference. It does not depend on the kinematic setting, but its number and duration can vary from one run to another.

a phase space bin N_i can be written as:

$$N_i = \mathcal{L}\int_i \frac{d\sigma}{d\Omega}d\Omega = \mathcal{L}\frac{\int_i \frac{d\sigma}{d\Omega}d\Omega}{\int_i d\Omega}\int_i d\Omega = \mathcal{L}\left\langle \frac{d\sigma}{d\Omega}\right\rangle_i \Delta\Omega_i\,, \tag{6.14}$$

which shows that dividing N_i by the luminosity $\mathcal{L}$ and the solid angle $\Delta\Omega_i$ of bin i, we can extract the *average* cross section over the bin. In order to determine solid angles that incorporate the various resolution effects together with the actual detection geometry, one needs a Monte Carlo (MC) simulation. Chapter 5 describes the simulation used for the DVCS experiment.

In our case, interesting quantities, some linear combinations of GPDs, $\mathcal{F}(GPDs)$, appear in the cross section multiplied by some kinematical factors $\Gamma(Q^2, x_B, t, \varphi)$ that also vary within the bin width. We can integrate all these factors in the Monte Carlo calculation of the acceptance, by computing a *weighted* solid angle:

$$N_i = \mathcal{L}\int_i \Gamma(Q^2, x_B, t, \varphi)\mathcal{F}(GPDs)\; d\Omega = \mathcal{L}\langle\mathcal{F}(GPDs)\rangle \underbrace{\int_i \Gamma(Q^2, x_B, t, \varphi)\; d\Omega}_{\text{MC integration}}\,. \tag{6.15}$$

With this idea in mind, I describe in the following the general procedure used to compute the experiment acceptance [75]. It takes into account two important effects:

- the variation of the kinematic factors within the bin width, as just mentioned,
- the effects of bin migration, caused by the resolution of the detectors.

6.9.1 General procedure

Let

$$\mathbf{x}_v = \{k, x_B, Q^2, t, \varphi_e, \varphi, v_z\}_v \tag{6.16}$$

represent the kinematic variables at the vertex (in the simulation). The incident electron energy k is included in order to treat the radiative tail. The angle φ_e is the angle between the leptonic and horizontal planes. Let

$$\mathbf{x}_e = \{k, x_B, Q^2, t, \varphi_e, \varphi, v_z\}_e \tag{6.17}$$

represent the event variables, as reconstructed by the detector. Here k_e is constant and equal to the measured electron beam energy $k_e = 5.7572\,\text{GeV}$ (cf. section 2.2.2.4). In the Monte-Carlo simulation, we define the mapping

$$K(\mathbf{x}_e|\mathbf{x}_v) \tag{6.18}$$

as the conditional probability distribution to observe an event at the kinematic point $\mathbf{x}_e$ starting from vertex point $\mathbf{x}_v$. The experimental acceptances, intrinsic detector efficiencies

and resolutions are included in $K(\mathbf{x}_e|\mathbf{x}_v)$. This conditional probability, which we compute using the MC simulation, takes into account the potential bin migration due to detectors resolution. The binning vector

$$\mathbf{i}_e = \{i_{x_B}, i_{Q^2}, i_t, i_\varphi\}_e \tag{6.19}$$

labels a set of bins in the corresponding event kinematics after integration over φ_e (this variable contains no physics). The binning vector

$$\mathbf{j}_v = \{j_{x_B}, j_{Q^2}, j_t, j_\varphi\}_v \tag{6.20}$$

labels a similar set of bins in the vertex variables.

The DVCS cross section can be written as a combination of several harmonic contributions as described in section 1.5. For the case of a cross section difference with opposite beam helicities, only two dominant harmonics remain:

$$\sigma^{\rightarrow}(\mathbf{x}_v) - \sigma^{\leftarrow}(\mathbf{x}_v) = \Gamma^1(\mathbf{x}_v) X^1_{\mathbf{j}_v}(GPDs) + \Gamma^2(\mathbf{x}_v) X^2_{\mathbf{j}_v}(GPDs) \tag{6.21}$$

$$\sigma^{\rightarrow}(\mathbf{x}_v) - \sigma^{\leftarrow}(\mathbf{x}_v) = \sum_{\Lambda=1}^{2} \Gamma^\Lambda(\mathbf{x}_v) X^\Lambda_{\mathbf{j}_v}\,, \tag{6.22}$$

where $\Gamma^1(\mathbf{x}_v)$ and $\Gamma^2(\mathbf{x}_v)$ represent some kinematical factors and $X^1_{\mathbf{j}_v}(GPDs)$ and $X^2_{\mathbf{j}_v}(GPDs)$ are linear combinations of GPDs that we want to measure.

The number of counts per bin at the vertex is

$$N(\mathbf{j}_v) = \mathcal{L} \int_{\mathbf{x}_v \in \mathrm{Bin}(\mathbf{j}_v)} \sum_{\Lambda=1}^{2} \Gamma^\Lambda(\mathbf{x}_v) X^\Lambda_{\mathbf{j}_v} d\mathbf{x}_v = \mathcal{L} \sum_{\Lambda=1}^{2} X^\Lambda_{\mathbf{j}_v} \int_{\mathbf{x}_v \in \mathrm{Bin}(\mathbf{j}_v)} \Gamma^\Lambda(\mathbf{x}_v) d\mathbf{x}_v\,, \tag{6.23}$$

where $\mathcal{L}$ is the integrated luminosity. In the experimental bin $\mathbf{i}_e$, the yield is

$$N(\mathbf{i}_e) = \int_{\mathbf{x}_e \in \mathrm{Bin}(\mathbf{i}_e)} d\mathbf{x}_e \sum_{\mathbf{j}_v} N(\mathbf{i}_v) K(\mathbf{x}_e|\mathbf{x}_v) \tag{6.24}$$

$$= \mathcal{L} \sum_{\mathbf{j}_v} \sum_{\Lambda=1}^{2} X^\Lambda_{\mathbf{j}_v} \int_{\mathbf{x}_e \in \mathrm{Bin}(\mathbf{i}_e)} d\mathbf{x}_e \int_{\mathbf{x}_v \in \mathrm{Bin}(\mathbf{j}_v)} d\mathbf{x}_v \Gamma^\Lambda(\mathbf{x}_v) K(\mathbf{x}_e|\mathbf{x}_v) \tag{6.25}$$

We define a bin mapping function:

$$K^\Lambda_{\mathbf{i}_e,\mathbf{j}_v} = \int_{\mathbf{x}_e \in \mathrm{Bin}(\mathbf{i}_e)} \int_{\mathbf{x}_v \in \mathrm{Bin}(\mathbf{j}_v)} d\mathbf{x}_e\, d\mathbf{x}_v\; K(\mathbf{x}_e|\mathbf{x}_v) \Gamma^\Lambda(\mathbf{x}_v)\,. \tag{6.26}$$

This function is basically the solid angle weighted by the kinematic factors $\Gamma^\Lambda(\mathbf{x}_v)$, where the effects of bin migration are taken into account through the function $K(\mathbf{x}_e|\mathbf{x}_v)$. Generally, the number of counts per bin can thus be written as:

$$N^{\mathrm{MC}}(\mathbf{i}_e) = \mathcal{L} \sum_{\mathbf{j}_v, \Lambda} K^\Lambda_{\mathbf{i}_e,\mathbf{j}_v} X^\Lambda_{\mathbf{j}_v}\,. \tag{6.27}$$

Note the summation over all $\mathbf{j}_v$. All bins at the vertex might contribute to a given experimental bin $\mathbf{i}_e$, with a certain probability or weight given by the function $K^{\Lambda}_{\mathbf{i}_e,\mathbf{j}_v}$, computed in the simulation. We can now construct a χ^2, which can be minimized to extract the $\mathbf{X}_{\mathbf{j}_v}$:

$$\chi^2 = \sum_{\mathbf{i}_e} \frac{[N^{\rm Exp}(\mathbf{i}_e) - N^{\rm MC}(\mathbf{i}_e)]^2}{[\sigma^{\rm Exp}(\mathbf{i}_e)]^2}\,, \tag{6.28}$$

where $\sigma^{\rm Exp}(\mathbf{i}_e)$ are the experimental error bars in each bin.

The coefficients $\overline{\mathbf{X}}_{\mathbf{j}_v}$ are defined as the values of $\mathbf{X}_{\mathbf{j}_v}$ that minimize χ^2:

$$0 \;=\; -\frac{1}{2}\frac{\partial\chi^2}{\partial X^{\Lambda}_{\mathbf{j}_v}}\bigg|_{\overline{\mathbf{X}}_{\mathbf{j}_v}} \tag{6.29}$$

$$0 \;=\; \sum_{\mathbf{i}_e} \mathcal{L} K^{\Lambda}_{\mathbf{i}_e,\mathbf{j}_v} \frac{\mathcal{L}\sum\limits_{\mathbf{j}'_v,\,\Lambda'} K^{\Lambda'}_{\mathbf{i}_e,\mathbf{j}'_v}\overline{X}^{\Lambda'}_{\mathbf{j}'_v} - N^{\rm Exp}(\mathbf{i}_e)}{[\sigma^{\rm Exp}(\mathbf{i}_e)]^2} \tag{6.30}$$

$$0 \;=\; \sum_{\mathbf{j}'_v,\,\Lambda'} \alpha^{\Lambda,\,\Lambda'}_{\mathbf{j}_v,\mathbf{j}'_v}\,\overline{X}^{\Lambda'}_{\mathbf{j}'_v} - \beta^{\Lambda}_{\mathbf{j}_v} \qquad \forall\,\mathbf{j}_v,\,\Lambda\,. \tag{6.31}$$

The linear system is defined by:

$$\alpha^{\Lambda,\,\Lambda'}_{\mathbf{j}_v,\mathbf{j}'_v} \;=\; \sum_{\mathbf{i}_e} \mathcal{L}\frac{K^{\Lambda}_{\mathbf{i}_e,\mathbf{j}_v}\,K^{\Lambda'}_{\mathbf{i}_e,\mathbf{j}'_v}}{[\sigma^{\rm Exp}(\mathbf{i}_e)]^2}\,, \tag{6.32}$$

$$\beta^{\Lambda}_{\mathbf{j}_v} \;=\; \sum_{\mathbf{i}_e} \frac{N^{\rm Exp}(\mathbf{i}_e)\,K^{\Lambda}_{\mathbf{i}_e,\mathbf{j}_v}}{[\sigma^{\rm Exp}(\mathbf{i}_e)]^2}\,. \tag{6.33}$$

The fit parameters are:

$$\overline{X}^{\Lambda}_{\mathbf{j}_v} = \sum_{\mathbf{j}'_v,\,\Lambda'} [\alpha^{-1}]^{\Lambda,\,\Lambda'}_{\mathbf{j}_v,\mathbf{j}'_v}\,\beta^{\Lambda'}_{\mathbf{j}'_v}\,. \tag{6.34}$$

The covariance matrix of the fitted parameters is:

$$V^{\Lambda,\,\Lambda'}_{\mathbf{j}_v,\mathbf{j}'_v} = [\alpha^{-1}]^{\Lambda,\,\Lambda'}_{\mathbf{j}_v,\mathbf{j}'_v}\,. \tag{6.35}$$

Note that the result, the *unknowns* of the linear system (6.33), are each linear combinations of GPDs averaged over each of the bins *at the vertex*. On the other hand, the data in the experimental bins $\mathbf{i}_e$, are the quantities used for the minimization of χ^2 in equation (6.28). There should be more *data points* than *unknowns* for the minimization procedure to work, i.e. for the linear system (6.33) to have a non-singular solution. In other words, the number of bins at the vertex should be smaller than the number of experimental bins. It is the variable φ which allows us to solve the system. Indeed, the unknowns quantities $\overline{X}^{\Lambda}_{\mathbf{j}_v}$ do not depend on the variable φ, so it makes no sense to bin on

this variable at the vertex. On the other hand, the number of counts (either $N^{\rm Exp}(\mathbf{i}_e)$ or $N^{\rm MC}(\mathbf{i}_e)$) do depend on φ through the $\varphi-$dependence of the kinematical factors $\Gamma^\Lambda(\mathbf{x}_v)$. We will therefore bin on the variable φ for experimental data.

6.9.2 Special case: the single spin cross-section difference

As mentioned in section 1.5.2, in the kinematic regime of this experiment the BH dominates over DVCS and through a cross section difference with opposite beam helicities we can access the imaginary part of the DVCS amplitude. In this particular case, only three terms $\Gamma^\Lambda(\mathbf{x}_v)$ remain, all helicity independent terms vanish. Furthermore, we can neglect the contribution of $|\mathcal{T}^{DVCS}|^2$ compared to the interference term, and so the number of Γ^Λ terms is two. The first, a twist 2 term, has a φ-dependence

$$\Gamma^1(\varphi) \sim \frac{\sin\varphi}{\mathcal{P}_1(\varphi)\mathcal{P}_2(\varphi)}\,, \tag{6.36}$$

where $\mathcal{P}_1$ and $\mathcal{P}_2$ are the BH propagators, which also depend on φ. The other contribution is a twist 3 term, with a φ dependence:

$$\Gamma^2(\varphi) \sim \frac{\sin 2\varphi}{\mathcal{P}_1(\varphi)\mathcal{P}_2(\varphi)}\,. \tag{6.37}$$

The number of *unknowns* in the system (6.33) is 2 times the number of bins *at the vertex*.

In this case

$$N^{\rm Exp}(\mathbf{i}_e) = \frac{1}{\mathcal{P}}[N^+(\mathbf{i}_e) - N^-(\mathbf{i}_e)]\,, \tag{6.38}$$

where $N^+(\mathbf{i}_e)$ and $N^-(\mathbf{i}_e)$ is the number of counts in an experimental bin for events of helicity $+1$ and -1 respectively, and $\mathcal{P}$ is the beam polarization. Note that in this observable, accidental events, which are helicity independent, are automatically subtracted.

Only the luminosity corresponding to positive (negative) helicity gates contributes to $N^+(\mathbf{i}_e)$ ($N^-(\mathbf{i}_e)$). As the beam charge asymmetry can be neglected (cf. Tab. 6.6), this means that the effective integrated luminosity contributing to the observable of Eq. (6.38) is

$$\mathcal{L} = \frac{\int \mathcal{L}_{+1,-1}\,dt}{2}\,. \tag{6.39}$$

6.10 Results

For each of the 3 different settings in Q^2, 5 bins in t have been made. Each experimental bin in Q^2 and t is divided into 25 bins in φ. Bin ranges and the average value of t in each bin are shown in Tab. 6.8. Fig. 6.24–6.26 show the results of the difference of counts for opposite helicity states (equation (6.38)) as a function of φ, for each of the experimental bins in Q^2 and t. Error bars are statistical only.

Fig. 6.25 and 6.26 show the effect of π^0 electroproduction, computed as described in section 6.6. As it can be seen, the effect is very small in our observable. Its contribution has

$t_{\min}$ (GeV^2)	$t_{\max}$ (GeV^2)	$\langle t \rangle$ (GeV^2)
-0.400	-0.349	-0.37
-0.349	-0.303	-0.33
-0.303	-0.257	-0.28
-0.257	-0.209	-0.23
-0.209	-0.121	-0.17

Table 6.8: Bin ranges in t and average t value over the bin, which is almost independent of the Q^2 setting.

been neglected at this point. For the kinematic setting 1 (Fig. 6.24), the π^0 contribution could not be accurately estimated. Indeed, the average π^0 energy is lower in this setting and the calorimeter threshold (around 1 GeV) reduces the number of detected π^0 events. Some extrapolation from the two other kinematic settings will probably be necessary and work is in progress. However, the effect is likely to be small, as in the two other cases.

Fig. 6.24–6.26 show raw counts and exhibit the experimental acceptance effects. The most important effect is the very irregular acceptance in φ for large $-t$. Eq. (6.12) shows that the value of t is directly related to the angle between the real and the virtual photons. As mentioned several times before, the virtual photon has a very small acceptance and is always pointing towards the center of the calorimeter. Then, the distance of the real photon impact point to the center of the calorimeter is directly related to the value of t, as shown in Fig. 6.22. For small values of $-t$ the acceptance of the calorimeter is flat. However, for large values of $-t$, the rectangular shape of the calorimeter implies a larger acceptance close to the corners, corresponding to the 4 values of the angle φ that define the corners, as shown in Fig. 6.23. The same acceptance effects appear at the same values of φ for the quantity $N^{\rm Exp}(\mathbf{i}_e)$ plotted in Fig. 6.24–6.26. However, the value of $N^{\rm MC}(\mathbf{i}_e)$ of Eq. (6.28) takes into account the acceptance of the experimental apparatus through the matrices $K^{\Lambda}_{\mathbf{i}_e,\mathbf{j}_v}$ of Eq. (6.27).

The red curves in Fig. 6.24–6.26 show the result of the fit obtained by minimizing χ^2 of Eq. (6.28). There are two different contributions to the fit: a $\sin\varphi$ modulated contribution corresponding to a twist 2 term (*handbag*), plotted in green, and a $\sin 2\varphi$ modulated contribution of twist 3 (in blue). The value of the linear combination of GPDs obtained is shown in the legend for each of these two terms, together with its statistical error. For the twist-2 term, this combination of GPDs is given by Eq. (1.63). Finally the χ^2 of the fit, normalized to the number of degrees of freedom $n = 25 - 2 = 23$, is also shown. The twist-2 term is obtained with high precision (10% or better). The twist-3 term is less accurately determined by the fits. It is compatible with zero at low $-t$ and has errors up to 50% at high $-t$.

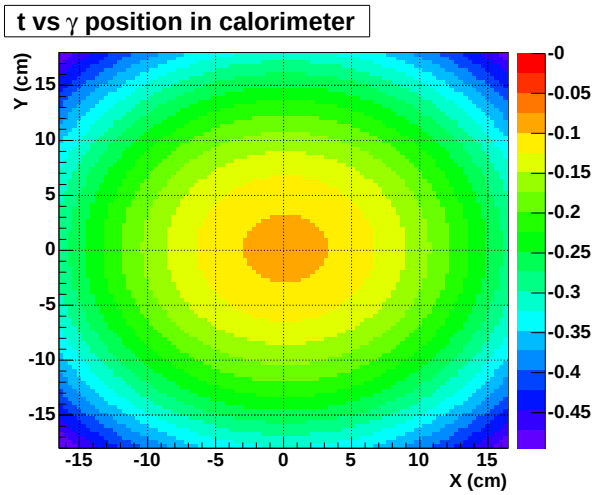

Figure 6.22: Value of the kinematic variable t as a function of the position of the real photon in the calorimeter, assuming the virtual photon points towards the center of the calorimeter. This figure is a graphical representation of Eq. (6.12).

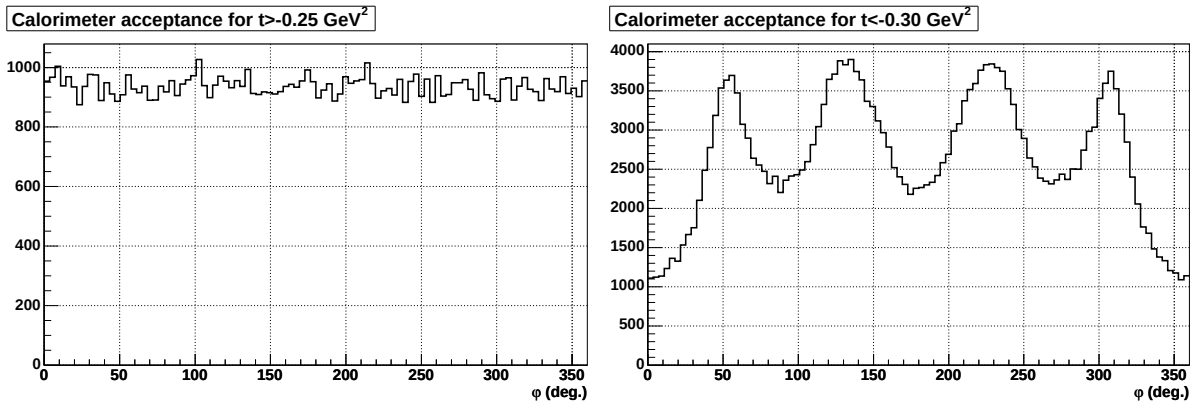

Figure 6.23: Acceptance in φ for small $-t$ (left) and large $-t$ (right), as shown in the Monte Carlo simulation, where events are generated following a flat distribution in t.

6.11 Discussion

6.11.1 Handbag dominance

The first interesting result which we can see in Fig. 6.24–6.26 is the relative small contribution of the twist-3 term (in blue) compared to the twist-2 term. Only at high $-t$, the twist 3 term begins to have a significant size. This is a first indication of the handbag mechanism dominance.

Note that the results of the fit, the linear combination of GPDs, for the twist-3 term are not smaller than those corresponding to the twist-2 term. Indeed, the twist 3 contribution

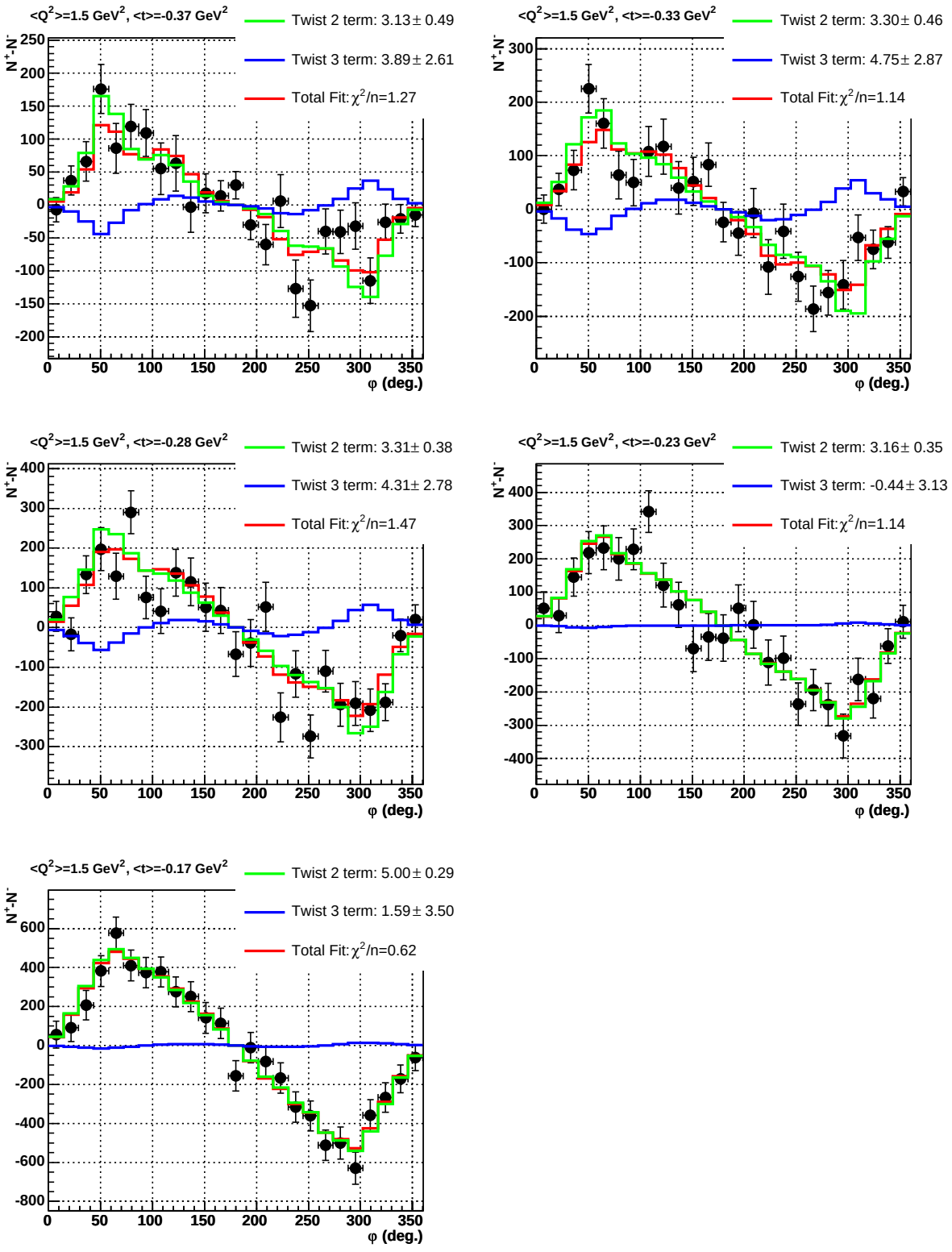

Figure 6.24: Results for kinematic setting 1 ($\langle Q^2 \rangle = 1.5\,\mathrm{GeV}^2$). For each of the 5 bins in t, the difference of the raw number of counts for opposite helicity events are plotted as a function of φ. The results of the fit is shown in red, together with each individual term: twist-2 in green and twist-3 in blue.

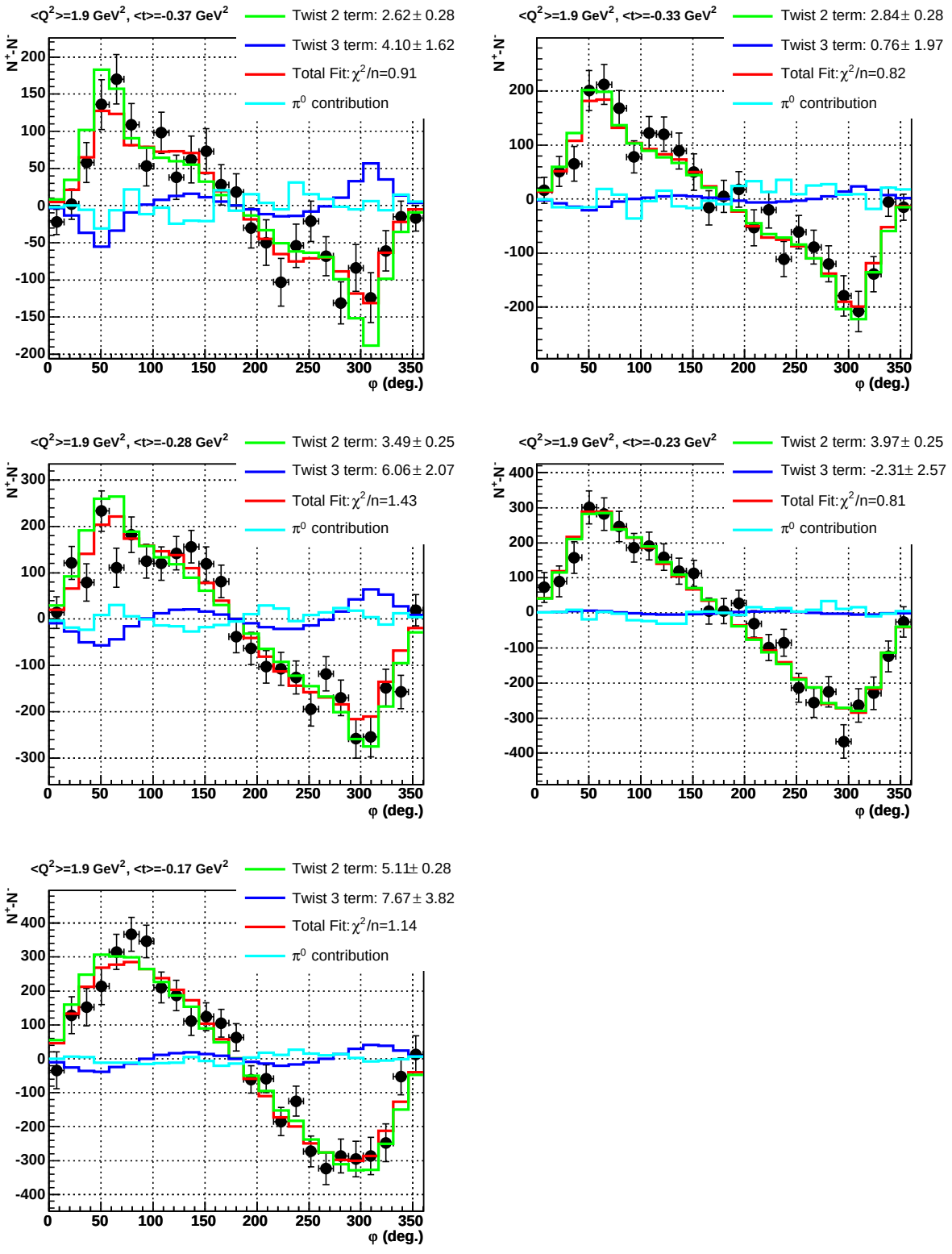

Figure 6.25: Results for kinematic setting 2 ($\langle Q^2 \rangle = 1.9\,\mathrm{GeV}^2$). For each of the 5 bins in t, the difference of the raw number of counts for opposite helicity events are plotted as a function of φ. The results of the fit is shown in red, together with each individual term: twist-2 in green and twist-3 in blue.

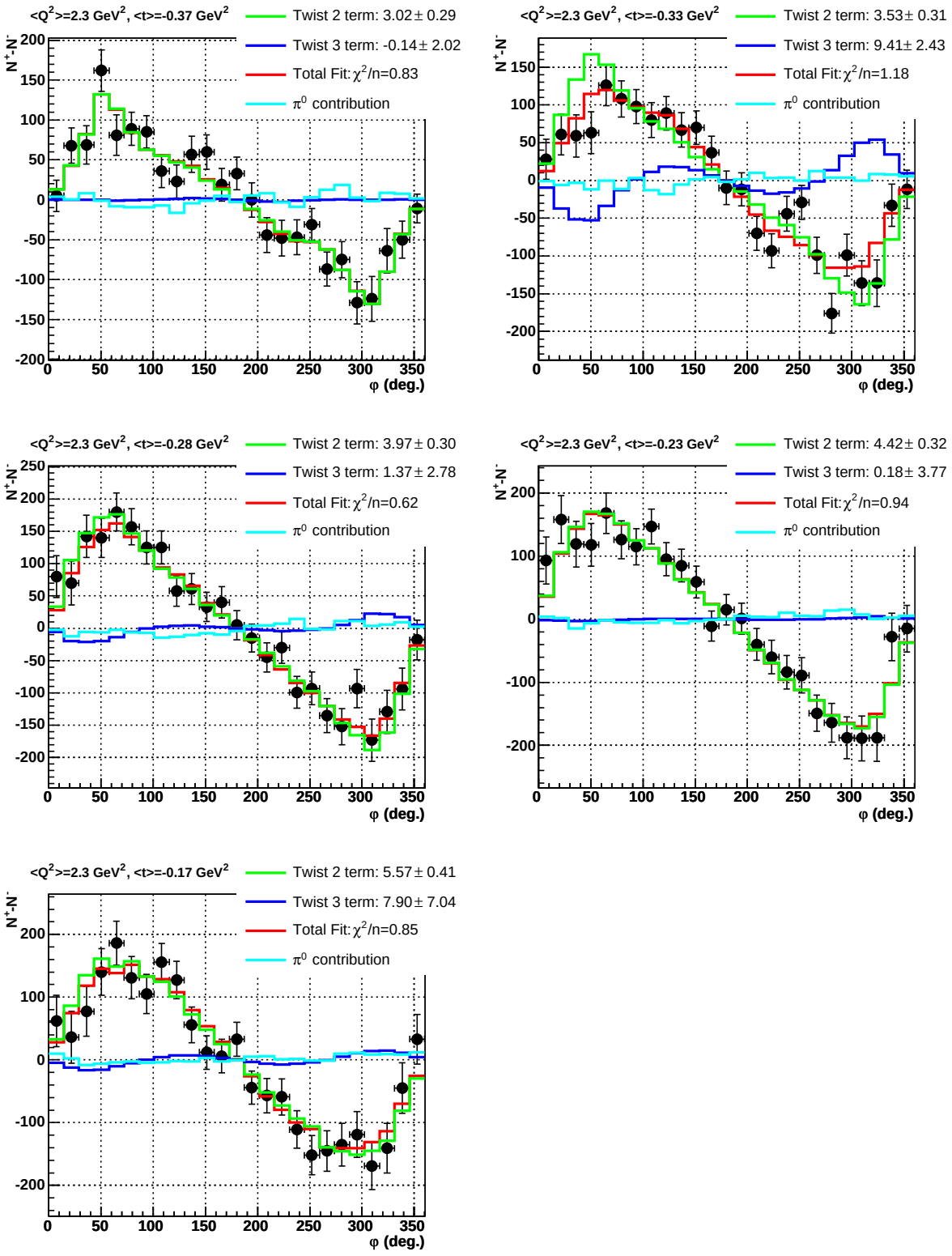

Figure 6.26: Results for kinematic setting 3 ($\langle Q^2 \rangle = 2.3\,\mathrm{GeV}^2$). For each of the 5 bins in t, the difference of the raw number of counts for opposite helicity events are plotted as a function of φ. The results of the fit is shown in red, together with each individual term: twist-2 in green and twist-3 in blue.

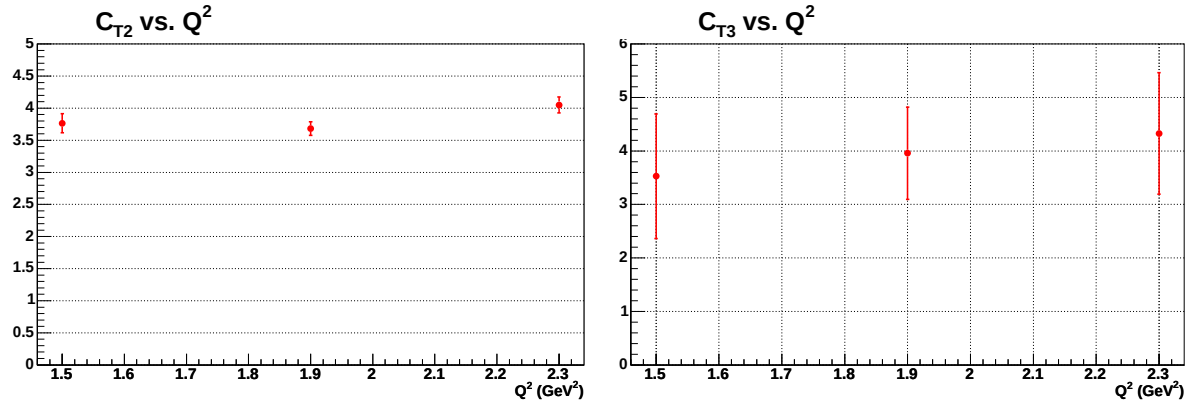

Figure 6.27: Q^2-dependence of each of the twist-2 and twist-3 terms for all bins in t. The small variation as a function of Q^2 for each of the $t-$bins shows the validity of the twist-3 approximation and the dominance of the handbag mechanism in the DVCS process.

is suppressed by the corresponding kinematical factor $\Gamma^{\Lambda}(\mathbf{x}_v)$ of Eq. (6.22). The twist-3 term appears multiplied by an additional power of the $1/Q-$power suppressed kinematical factor K, which goes to zero as $t \to t_{\rm min}$.

A stronger test of the handbag dominance can be obtained from the Q^2 dependence of the twist-2 and twist-3 terms obtained. As said before, all kinematic dependence (up to the twist-3 approximation) is removed from these terms and included in the kinematical functions $\Gamma^{\Lambda}(\mathbf{x}_v)$, computed by Monte Carlo. If the twist-3 approximation is correct and we can neglect higher twist contributions, then the twist-2 and twist-3 terms obtained here should have no Q^2 dependence, as there is no Q^2 dependence in GPDs[1].

In order to quantify the dominance of the handbag over the whole kinematic regime of the experiment, all data for each kinematic setting was integrated over a single bin in t: $-0.4 < t < -0.12\,\mathrm{GeV}^2$. Fig. 6.27 shows the variation of the twist-2 and twist-3 terms over the full Q^2 range of the experiment. The twist-2 term, which is measured with high precision (of the order of 3%) does not more than 2σ in the Q^2 range from $1.5\,\mathrm{GeV}^2$ to $2.3\,\mathrm{GeV}^2$. The variation of the twist-3 term, less accurately measured, is compatible with zero. The twist-3 term is measured with 20%–30% uncertainty.

6.11.2 $t-$dependence

Once verified that the handbag mechanism seems the leading underlying mechanism in the DVCS process in this kinematic region, we can interpret results in terms of (twist-2) GPDs. Fig. 6.28 shows the variation of the twist-2 term as a function of t. This term is the linear combination of GPDs given by Eq. (1.63):

$$\mathrm{C_{T2}} \equiv \Im\mathrm{m}C^{\mathcal{I}} = F_1\Im\mathrm{m}\mathcal{H} + \frac{x_B}{2-x_B}(F_1+F_2)\Im\mathrm{m}\tilde{\mathcal{H}} - \frac{t}{4M^2}F_2\Im\mathrm{m}\mathcal{E}\,. \tag{6.40}$$

[1]There is a known logarithmic Q^2 evolution of GPDs, but it can be neglected in the Q^2 range of this experiment ($1.5 - 2.3\,\mathrm{GeV}^2$).

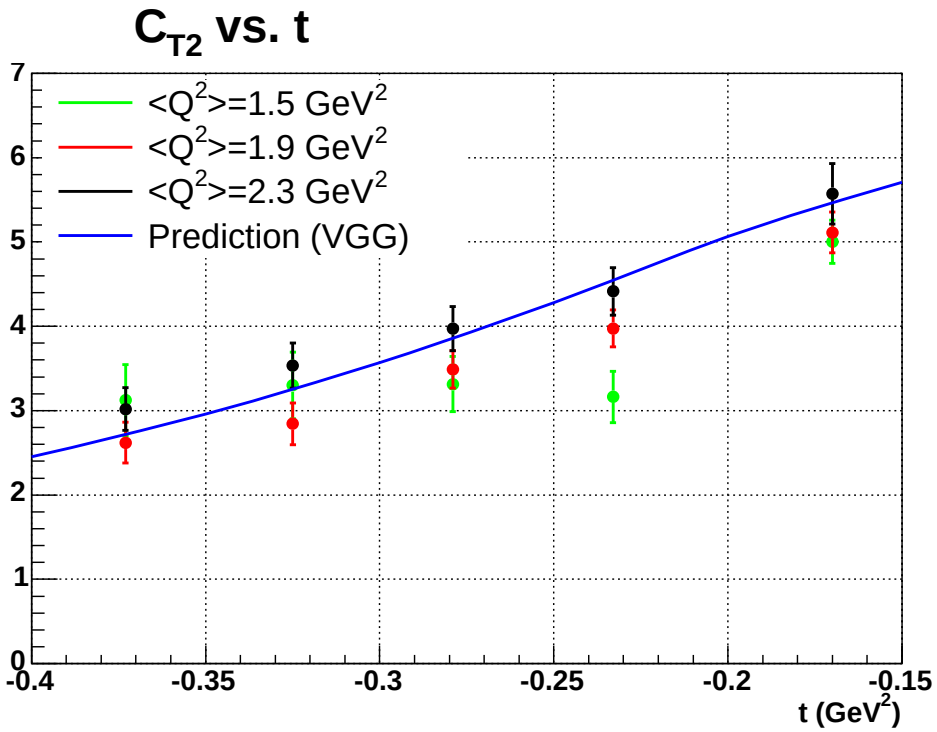

Figure 6.28: Under the dominance of the handbag diagram, the twist-2 term can be interpreted as the linear combination of GPDs of Eq. (1.63). The $t-$dependence of these coefficients contain both the one coming from form factors and the one contained in GPDs. Error bars are statistical only and are of the order of 15%.

We observe again the very slight dependence on Q^2. The dependence on the variable t includes the dependence already in the form factors $F_1(t)$ and $F_2(t)$ appearing in Eq. (6.40). The additional dependence is due to the $t-$dependence of GPDs H, $\tilde{H}$ and $\tilde{E}$. In our kinematic domain the contribution of the GPD E is very suppressed by the kinematical term $t/(4M^2)$ and the fact that $F_2 \ll F_1$ for the proton. The contribution of the GPD $\tilde{H}$ is slightly suppressed by $x_B/(2-x_B) = 0.22$.

Fig. 6.28 shows the comparison of the measured values with the prediction of the model of GPDs by Vanderhaeghen, Guichon and Guidal (VGG) [20, 21, 22] described in section 1.6. The values $b_{val} = b_{sea} = 1$ and $\alpha' = 0.8$ were used, and the contribution from the D-term was neglected. The absolute value and $t-$dependence of the data is well reproduced by the model, where an important contribution is, as mentioned before, the $t-$dependence of form factors, which is known.

6.11.3 Stability of results on the missing mass squared cut

The twist-2 term results for kinematic 3 are plotted in Fig. 6.29 for different values of the M_X^2 cut for each of the five bins in t. We observe that the result is stable around the missing mass squared cut $M_X^2 = (M_p + m_{\pi^0})^2$. For high values of $-t$ the results depends

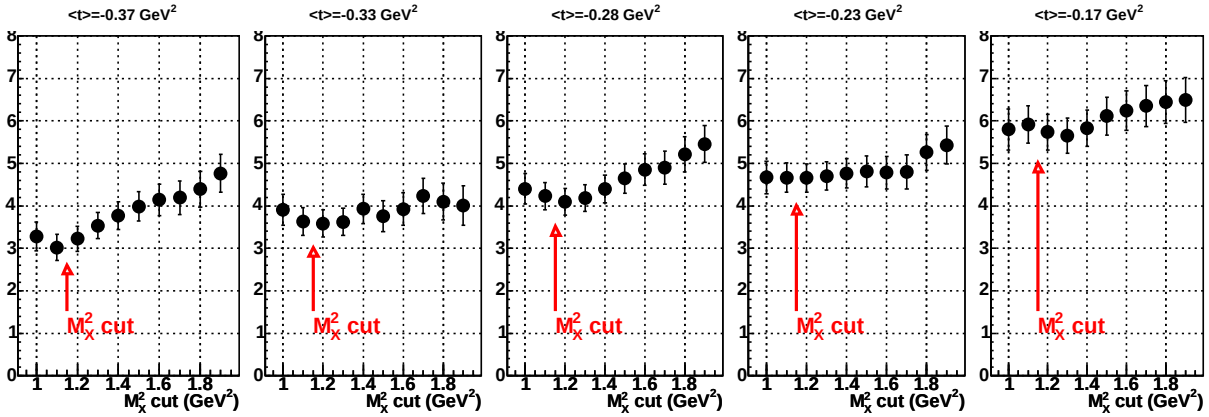

Figure 6.29: For kinematic 3 and each of the bins in t, the twist-2 term is plotted as a function of the M_X^2- cut (cf. section 6.5).

slightly on the value of this cut. The acceptance at high $-t$ depends strongly on φ as explained in 6.10 (cf. Fig. 6.23), and is more difficult to reproduce in the Monte Carlo. A rough estimate of the systematic error introduced by this cut is 5%. However, this error can be reduced with additional work on the Monte Carlo simulation of the calorimeter.

6.12 Cut summary and systematic error budget

Tab. 6.9 shows a summary of all the cuts and normalizations applied to the data, with an estimate of the systematic error introduced. The largest systematic error comes from the missing mass cut, of the order of 5% for certain bins in t. This error can probably be reduced with additional work on the Monte Carlo simulation in order to better compute the acceptance of the experiment. Beam polarization is the next most important systematic error. By analyzing the photon detector of the Compton calorimeter it can probably be reduced by 0.5%.

6.13 Outlook

Results presented here are very preliminary. Some corrections remain to be done. First, the contamination coming from π^0 electroproduction must be evaluated for kinematic setting 1. Also, while real radiative corrections, both internal and external, have been made, the contribution from virtual radiative corrections must be estimated.

Up to now, only the cross section difference for opposite electron helicities has been studied. The quality of the data is sufficiently high that it is promising to look into more complicated observables, such as the total DVCS cross-section, in order to access the real part of the DVCS amplitude and other combinations of GPDs.

Cut/Efficiency	Correction	Systematic error
Čerenkov inefficiency	+1.2%	0.1%
Geometrical acceptance cuts (HRS+calo)	–	0.5%
HRS multi-track	Tab. 6.2	0.1%
Target length	–(13.5 cm/15.0 cm)	1%
Clustering coincidence window	$<10^{-4}$	–
Calorimeter and trigger inefficiency	+1%	1%
Missing mass cut	–	5%
1-cluster cut	Tab. 6.5	0.1%
Charge	Tab. 6.6	0.2%
DT correction	Run-by-run	0.2%
Beam polarization	1/75.3%	2.0%
π^0 contamination	*under evaluation*	?
Virtual radiative corrections	*under evaluation*	?
	Total	5.6%+?

Table 6.9: Summary of corrections and systematic error budget.

Conclusion

Generalized Parton Distributions provide a very promising tool for systematically exploring hadron structure. In contrast to form factors and quark and gluon distributions, GPDs access quark position and momentum correlations in the nucleon, which are at present largely unknown. Furthermore, moments of GPDs provide new nucleon structure information and are also easily transported to lattice QCD calculations for direct comparison [76, 77]. In particular, the second moment of a particular combination of GPDs gives access to the total angular momentum carried by quarks in the nucleon [10, 11].

Deeply Virtual Compton Scattering is the cleanest reaction accessing the GPDs. Compared to other hard scattering processes, DVCS provides the simplest final state, and thus the simplest interpretation in terms of the nucleon GPDs. The advent of high luminosity accelerator facilities has made the study of GPDs accessible to experiment. The E00-110 experiment in the Hall A of Jefferson Lab is the first high statistics, dedicated DVCS experiment, and the subject of this thesis.

The E00-110 experiment presented several technical challenges. Two new detectors were designed and constructed to run at a luminosity of $10^{37}\,\mathrm{cm}^{-2}\,\mathrm{s}^{-1}$ at angles down to 15° from the beamline and at a distance of only 1.1 m from the target. The unprecedented background environment in such an open geometry required the development of novel electronics and data acquisition system.

The electromagnetic calorimeter performed very well during the whole experiment. The intense exposure to radiation produced an attenuation of the crystals transparency. However, the resolution obtained at the end of the experiment, during the last elastic calibration, was as good as the resolution obtained at the beginning of the experiment. Due to the fact that radiation damage was concentrated in the front face of crystals, the LED monitoring system was more sensitive to it than the electromagnetic showers, which develop deeper inside blocks. Calibration using the constrained elastic reaction was therefore the most reliable procedure for the electromagnetic calorimeter. A resolution of 2.4% at 4.2 GeV was obtained at the elastic calibration setting. In normal running and background conditions a resolution of $5\%/\sqrt{E}$ reproduced the missing mass width measured. Another calibration method consists of using the π^0 decay and the invariant mass of two cluster events in the calorimeter. This calibration technique has not been applied. Instead, we used the elastic calibrations and an extrapolation of coefficients based on the radiation dose received by each block. The reconstructed π^0 invariant mass width was used to check that the calibration was satisfactory during the experiment, i.e. the π^0 invariant mass width was almost constant.

The proton detector was the luminosity limiting factor of the experiment. Its PMTs were damaged significantly by low energy background. PMT anode current was continuously monitored during the experiment. PMTs from blocks closest to the beamline operated at about 45 μA of anode current, and some of them died a few days before the end of the experiment.

ARS sampling electronics were essential to achieve the time and energy resolutions obtained. The large amount of data that had to be transfered for each event was the limiting factor in DAQ deadtime. The calorimeter trigger module, which made an online selection of interesting channels to read, was an indispensable part of the acquisition, together with the multiplexer module that allowed the selection of proton detector channels. Each PMT signal was sampled at 1 GHz over 128 ns. However, careful studies of the waveform analysis algorithm showed that it was more efficient to use only a subset of the signal data for analysis: 80 samples were used for calorimeter analysis, and only 30 for proton detector analysis. Obviously, transferring only some of the ARS samples of each channel instead of all 128 would have reduced deadtime.

The new detectors and electronics required the development of original methods for their analysis. The waveform analysis algorithm to treat pile-up was efficient but time-consuming. The inefficiency of the algorithm used to reconstruct events in noisy blocks was computed accurately by measuring accidental events and testing the algorithm under simulation. Efficiency was higher than 90% in most of the proton detector for energy losses higher than 30 MeV.

As argued in chapter 6, using only the HRS and the calorimeter, together with a tight cut on the missing mass $e\ p \rightarrow e\ \gamma\ X$, provides a clean selection of DVCS events. Indeed, the π^0 electroproduction contribution can be subtracted from our data using the events where the two photons from the π^0 decay are detected in the calorimeter. Furthermore, the contamination coming from associated DVCS (i.e. the production of an additional pion) is expected small with a missing mass cut at the pion production threshold. Some additional tests are still needed in order to better estimate systematic errors and background contamination.

The main goal of the E00-110 experiment was to test whether the kinematic regime accessible at Jefferson Lab allows one to interpret the DVCS amplitude in terms of Generalized Parton Distributions. This is a fundamental step before one can draw any conclusions about the structure of the nucleon from DVCS measurements. Results presented here show a good agreement with the twist-3 approximation of the DVCS amplitude, where the handbag diagram is the dominant contribution.

Preliminary results from the difference of cross sections for opposite beam helicities allowed the extraction of a linear combination of Generalized Parton Distributions as a function of the transfer t to the proton. This is the first direct measurement of GPDs. The accuracy of this measurement will provide strong constraints to models and parametrizations. The comparison with a GPD model prediction from Vanderhaeghen, Guichon and Guidal [20, 21, 22] shows a very good agreement. In addition to the cross section difference presented here, the extraction of the unpolarized cross section is also planned. Taken together with the imaginary part of the DVCS amplitude (measured through the single

spin cross-section difference), it will provide a first measurement of the real part of the DVCS amplitude, and hence another set of GPD observables.

This is the beginning of a vast experimental program. Larger kinematic domains and a variety of different observables are needed to map out GPDs over their full parameter space. There are three major types of exclusive processes where GPDs can be measured or accessed. The object of this thesis, the leptoproduction of photons is, as already mentioned, the "golden" process and a number of experiments are already in progress and planned. An experiment covering a larger kinematic domain in Q^2 and x_B took place in 2005 in the Hall B of Jefferson Lab [41]. Also, by using a polarized target different kinds of GPD observables are accessible using the DVCS reaction. A dedicated experiment is proposed to measure DVCS with a polarized target and the spectrometer CLAS [78]. Another very interesting measurement is DVCS on the neutron. With this goal, an experiment using a deuterium target ran in Hall A in 2004 [40], and is currently under analysis [79]. DVCS on the neutron is mostly sensitive to the least constrained GPD, E. However, in order to understand how precisely one can determine neutron properties in hard reactions, one must understand completely the structure of contributions in measurements using deuterium targets. So far, the analysis has been performed only within the framework of the parton model [80, 81]. The consideration should be extended at least to the same level of precision as in the DVCS on the nucleon target, i.e. to twist-3 accuracy. HERMES and H1 will soon use a recoil detector, which will allow the exclusive measurement of the DVCS channel. Dedicated DVCS programs at HERA are planned [34, 43] in the next few years. A complementary kinematic domain to that of HERMES and Jefferson Lab could be explored by the COMPASS collaboration at CERN [44]: small x_B ($0.03 < x_B < 0.27$) and high Q^2 ($1.5 < Q^2 < 6.5\,\mathrm{GeV}^2$). This collaboration, which could start a DVCS program by 2010, would also add a recoil detector to their current setup in order to make an exclusive DVCS measurement.

At sufficiently large Q^2, the hard exclusive leptoproduction of a meson from a nucleon target is another major process involving GPDs. The production of pseudoscalar mesons is sensitive to the polarized GPDs $\tilde{H}$ and $\tilde{E}$, whereas the vector meson production is sensitive to the unpolarized GPDs H and E. Electroproduction of mesons is unique in its ability to potentially disentangle the flavor components of the GPDs. By changing the type of produced meson one can access different flavor combinations of GPDs.

Neutral pion electroproduction ($\gamma^* \; p \to p \; \pi^0$) cross-section was measured with the E00-110 data [69]. However, the factorization and the interpretation of these data in terms of GPDs is only valid for longitudinal photons. A factorization into a hard and soft part does not hold for transverse photons, and there is no dominance of the handbag mechanism expected even at large Q^2. Longitudinal cross sections for ρ^0 electroproduction have been measured for values of Q^2 between 1.5 and $3.0\,\mathrm{GeV}^2$ [82] and calculations based on GPD models reproduce the data. Electroproduction of ω mesons was measured up to $Q^2 \sim 5\,\mathrm{GeV}^2$ [83]. However, in contrast to the ρ^0 electroproduction, the measurement indicates that helicity is not conserved in the case of the ω meson and so the separation of the longitudinal and transverse cross sections could not be done. Here the interpretation in terms of GPDs must be postponed until data are available at higher momentum transfers.

The upgrade of the beam energy up to 12 GeV at CEBAF [84], planned around 2013, will open a new window for further investigation of these and other hard exclusive reactions.

As already mentioned before, thanks to the interference with the Bethe-Heitler process, DVCS provides a way to access GPDs directly via the imaginary part of its amplitude. However, this is only the case along the lines $x = \pm\xi$. A process unique in its ability to lift this kinematical restriction of DVCS and measure the full surface of the GPDs is Double DVCS (or DDVCS) [85]: $e\ p \to e'\ p'\ l\ \bar{l}$. In this reaction, very similar to DVCS, the final photon is off-shell, and couples to a pair of leptons in the final state. The virtuality of the final photon adds a new degree of freedom that allows the exploration of GPDs as a function of their three arguments independently. This process is highly suppressed compared to that of DVCS (about 200 times smaller), which makes its experimental measurement very challenging and unlikely until future facilities with higher luminosity are available. From the theoretical point of view, electroproduction of electron pairs requires that we add the exchange contributions due to the identical nature of the electrons in the final state. An immediate problem that still needs to be addressed by theory is the calculation of the Bethe-Heitler amplitudes for the case whre the final state leptons are identical to those in the initial state $l = e$. This will bring a vast variety of polarization and azimuthal observables that will further help to unravel the complicated structure of GPDs. Also, the theory of twist-3 effects in DDVCS is not yet developed.

In summary, given the active theoretical and experimental development around the subject of GPDs and DVCS in particular, we can anticipate a very intense activity in this field over the next few years. On an intermediate time scale, progress will depend upon the proposed beam energy upgrade to 12 GeV and the DVCS program at COMPASS. In the long term, the project of a high luminosity Electron-Ion-Collider EIC [86] can help continue the study of GPD physics with detail and precision.

Bibliography

[1] A. V. Belitsky, D. Müller, A. Kirchner, Nucl. Phys. **B629**, 323 (2002).

[2] A. V. Belitsky, X. Ji, F. Yuan, Phys. Rev. **D69**, 074014 (2004).

[3] F. Halzen and A. D. Martin, *Quarks & leptons* (John Wiley & Sons Inc., New York, 1984).

[4] R. Hofstadter and R. W. Mcallister, Phys. Rev. **98**, 217 (1955).

[5] A. V. Belitsky, A. V. Radyushkin, Phys. Rept. **418**, 1 (2005).

[6] J. Ellis, *Weak and Electromagnetic Interactions at High Energy* (Eds. R. Balian and C. H. Llewellyn Smith, North-Holland, Amsterdam, 1977).

[7] J. C. Collins, Adv. Ser. Direct. High Energy Phys. **5**, 1 (1988).

[8] J. C. Collins, A. Freund, Phys. Rev. **D59**, 074009 (1999).

[9] X. Ji, J. Osborne, Phys. Rev. **D58**, 094018 (1998).

[10] X. Ji, Phys. Rev. **D55**, 7114 (1997).

[11] X. Ji, Phys. Rev. Lett. **78**, 610 (1997).

[12] M. Diehl, Phys. Rept. **388**, 41 (2003).

[13] M. Burkardt, Phys. Rev. **D62**, 071503 (2000).

[14] M. Burkardt, Int. J. Mod. Phys. **A18**, 173 (2003).

[15] M. Diehl, Eur. Phys. J. **C25**, 223 (2002).

[16] J. P. Ralston and B. Pire, Phys. Rev. **D66**, 111501 (2002).

[17] A. V. Belitsky and D. Müller, Nucl. Phys. **A711**, 118 (2002).

[18] A. Freund, Phys. Lett. **B472**, 412 (2000).

[19] A. V. Belitsky, D. Müller, Nucl. Phys. **B589**, 611 (2000).

[20] M. Vanderhaeghen, P. Guichon and M. Guidal, Phys. Rev. **D60**, 094017 (1999).

[21] K. Goeke, M. V. Polyakov and M. Vanderhaeghen, Prog. Part. Nucl. Phys. **47**, 401 (2001).

[22] M. Guidal, M. V. Polyakov, A. V. Radyushkin, M. Vanderhaeghen, Phys. Rev. **D72**, 054013 (2005).

[23] A. V. Radyushkin, Phys. Lett. **B449**, 81 (1999).

[24] K. Goeke, M. V. Polyakov, M. Vanderhaeghen, Prog. Part. Nucl. Phys. **47**, 401 (2001).

[25] M. Polyakov, C. Weiss, Phys. Rev. **D60**, 114017 (1999).

[26] D. Müller, D. Robaschik, B. Geyer, F. M. Dittes, J. Fortsch, Fortsch. Phys. **42**, 101 (1994).

[27] A. V. Radyushkin, Phys. Lett. **B380**, 417 (1996).

[28] A. V. Radyushkin, Phys. Lett. **B385**, 333 (1996).

[29] A. V. Radyushkin, Phys. Rev. **D56**, 5524 (1997).

[30] P. A. M. Guichon, M. Vanderhaeghen, Prog. Part. Nucl. Phys. **41**, 125 (1998).

[31] C. Adloff et al., Phys. Lett. **B517**, 47 (2001).

[32] S. Chekanov et al., Phys. Lett. **B573**, 46 (2003).

[33] A. Freund, M. McDermott, M. Strikman, Phys. Rev. **D67**, 036001 (2002).

[34] A. Airapetian et al., Phys. Rev. Lett. **87**, 182001 (2001).

[35] S. Stepanyan et al., Phys. Rev. Lett. **87**, 182002 (2001).

[36] N. Kivel, M. V. Polyakov, M. Vanderhaeghen, Phys. Rev. **D63**, 114014 (2001).

[37] A. V. Belitsky, A. Kirchner, D. Mueller, A. Schafer, Phys. Lett. **B510**, 117 (2001).

[38] M. Diehl, T. Gousset, B. Pire and J. P. Ralston, Phys. Lett. **B411**, 193 (1997).

[39] P. Y. Bertin, C. Hyde-Wright, R. Ransome, F.Sabatié et al., Jefferson Lab proposal **E00-110** (2000).

[40] P. Y. Bertin, C. Hyde-Wright, F.Sabatié, E. Voutier et al., Jefferson Lab proposal **E03-106** (2003).

[41] V. Burkert, L. Elouadrhiri, M. Garçon, S. Stepanyan et al., Jefferson Lab proposal **E01-113** (2001).

[42] V. A. Korotkov, W. D. Nowak, Eur. Phys. J. **C23**, 455 (2002).

[43] VPS proposal, [DESY PRC 01/00] and [H1-5/00-582] .

[44] The COMPASS collaboration, Expression of Interest **SPSC-EOI-005**, (2005).

[45] C. W. Leemann, D. R. Douglas and G. A. Krafft, Nucl. Part. Sci. **51**, 413 (2001).

[46] A. Alconrn, et al., Nucl. Inst. and Meth. **A522**, 294 (2004).

[47] M. Iodice, et al., Nucl. Inst. and Meth. **A411**, 223 (1998).

[48] K. G. Fissum, et al., Nucl. Inst. and Meth. **A474**, 108 (2001).

[49] M. Baylac et al., Phys. Lett. **B539**, 8 (2002).

[50] J. Berthot and P. Vernin, Nucl. Phys. News **9**, 12 (1990).

[51] F. Feinstein, Proc. 2002 Conference on advances in Photon Detection France (2002).

[52] P. Y. Bertin, Internal collaboration report (2003).

[53] M. Mazouz, P.-Y. Bertin and E. Voutier, JLab Technical Note **JLAB-05-042**, (2005).

[54] V. Breton, et al., Nucl. Inst. and Meth. **A362**, 478 (1995).

[55] M. Mazouz and E. Voutier, JLab Technical Note **JLAB-05-033**, (2005).

[56] R. Brun et al., CERN Program Library **W5015**, (1990).

[57] G. Laveissiere et al., Phys. Rev. Lett. **93**, 122001 (2004).

[58] M. Rvachev, JLab Technical Note **JLAB-01-055**, (2001).

[59] J. Roche et al., Phys. Rev. Lett. **85**, 708 (2000).

[60] M. Vanderhaeghen, J.M. Friedrich, D. Lhuillier, D. Marchand, L. Van Hoorebeke, J. Van de Wiele, Phys. Rev. **C62**, 025501 (2000).

[61] J. Schwinger, Phys. Rev. **76**, 790 (1949).

[62] Y. S. Tsai, Phys. Rev. **122**, 1898 (1961).

[63] L. W. Mo, Y. S. Tsai, Rev. Mod. Phys. **41**, 205 (1969).

[64] L. C. Maximon, Rev. Mod. Phys. **41**, 193 (1969).

[65] P. Janssens et al., *to be summitted to* Nucl. Inst. and Meth .

[66] Y. S. Tsai, Rev. Mod. Phys. **815**, 46 (1974).

[67] X. Jiang, PhD thesis, University of Massachusetts Amherst .

[68] R. Brun, F. Rademakers, Nucl. Inst. and Meth. **A389**, 81 (1997).

[69] A. Camsonne, PhD thesis, Université Blaise Pascal (2005).

[70] P. A. M. Guichon, L. Mossé and M. Vanderhaeghen, Phys. Rev. (2003).

[71] L. L. Frankfurt et al., Phys. Rev. Lett. **84**, 2589 (2000).

[72] P. Y. Bertin, Internal collaboration report (2005).

[73] A. Camsonne, C. Ferdi, Internal collaboration report (2005).

[74] S. Nanda, Internal communication (2004).

[75] P. Y. Bertin, C. E. Hyde-Wright, Internal collaboration report (2005).

[76] M. Gockeler et al., Phys. Rev. Lett. **92**, 042002 (2004).

[77] P. Hagler et al., Phys. Rev. **D68**, 034505 (2003).

[78] A. Biselli, L. Elouadrhiri, K. Joo, S. Niccolai et al., Jefferson Lab proposal **E05-114** (2005).

[79] M. Mazouz, PhD thesis (2006).

[80] A. Kirchner, D. Müller, Eur. Phys. J. **C32**, 347 (2003).

[81] F. Cano, B. Pire, Eur. Phys. J. **A19**, 423 (2004).

[82] C. Hadjidakis et al., Phys. Lett. **B605**, 256 (2005).

[83] L. Morand et al., Eur. Phys. J. **A24**, 445 (2005).

[84] The Science Driving the 12 GeV Upgrade of CEBAF, Jefferson Lab internal report (2001).

[85] M. Guidal, M. Vanderhaeghen, Phys. Rev. Lett. **90**, 012001 (2003).

[86] R. Holt et al., Brookhaven Report **BNL-68933**, (2002).

Resumé

Les Distributions de Partons Généralisées (GPDs), introduites à la fin des années 90, décrivent de façon universelle la structure des hadrons en fonction des degrés de liberté de la Chromodynamique Quantique: les quarks et les gluons. Les GPDs apparaissent dans une grande variété de réactions exclusives et l'avènement des accélérateurs de haute luminosité a rendu possible leur étude expérimentale. La Diffusion Compton Profondément Virtuelle (DVCS) est le processus clef faisant intervenir les GPDs. La première expérience dédiée à la mesure du DVCS a eu lieu dans le Hall A au Jefferson Lab en 2004. Un calorimètre électromagnétique, un anneau de scintillateurs ainsi que l'électronique associée ont été construits. Ce document décrit la préparation de cette expérience, les prises de données et leur analyse. Les résultats de la mesure de la différence de sections efficaces absolues avec des hélicites du faisceau opposées constituent la première mesure d'une combinaison linéaire des GPDs.

MOTS CLEFS

Sonde électromagnétique. Structure du nucléon. Réactions exclusives. Distributions de Partons Généralisées (GPDs). Diffusion Compton Profondément Virtuelle (DVCS). Jefferson Lab (CEBAF).

Abstract

Generalized Parton Distributions (GPDs), introduced in the late 90s, provide a universal description of hadrons in terms of the underlying degrees of freedom of Quantum Chromodynamics: quarks and gluons. GPDs appear in a wide variety of hard exclusive reactions and the advent of high luminosity accelerator facilities has made the study of GPDs accessible to experiment. Deeply Virtual Compton Scattering (DVCS) is the golden process involving GPDs. The first dedicated DVCS experiment ran in the Hall A of Jefferson Lab in Fall 2004. An electromagnetic calorimeter and a plastic scintillator detector were constructed for this experiment, together with specific electronics and acquisition system. The experiment preparation, data taking and analysis are described in this document. Results on the absolute cross section difference for opposite beam helicities provide the first measurement of a linear combination of GPDs as a function of the momentum transfer to the nucleon.

KEYWORDS

Electromagnetic probe. Nucleon structure. Exclusive reactions. Generalized Parton Distributions (GPDs). Deeply Virtual Compton Scattering (DVCS). Jefferson Lab (CEBAF).